# PHOTOPHYSICS OF ORGANIC PROBES AND THEIR APPICATIONS IN BIOIMAGING & PHOTODYNAMIC THERAPY

by

BOSUNG KIM
B.S. Kookmin University, 2008

A dissertation submitted in partial fulfillment of the requirements
for the degree of Doctor of Philosophy
in the Department of Chemistry
in the College of Sciences
at the University of Central Florida
Orlando, Florida

Spring Term
2015

Major Professor: Kevin D. Belfield

# ABSTRACT

Over the past several decades the phenomenon of luminescence (divided into fluorescence and phosphorescence) has received great attention in the field of biological science. This quest has motivated scientists for a variety of applications, including fluorescence imaging. Fluorescence microscopy techniques that provide unique advantages, such as high spatial resolution and superior sensitivity, have been regarded as attractive tools in biophotonics. With the progress of ultrafast laser sources, two-photon absorption (2PA), in which a molecule absorbs two photons simultaneously, has opened possibilities of using it for various applications. Two-photon fluorescence microscopy (2PFM), which affords deeper tissue penetration and excellent three-dimensional (3D) images, is now being widely employed for bioimaging.

This dissertation focuses on the design, synthesis, and photophysical characterization of new fluorophores, as well as desirable applications. Chapter 1 gives an account of a brief introduction of luminescence and 2PA, as well as their utilities in biological applications. In chapter 2, a series of new BODIPY derivatives are presented along with their comprehensive linear and nonlinear characteristics. They exhibited excellent photophysical properties including large extinction coefficients, high fluorescence quantum yields, good photostability, and reasonable two-photon absorption cross sections. Two promising compounds were further evaluated as NIR fluorescent probes in one-photon and two-photon fluorescence imaging. Chapter 3 provides the design, synthesis, and photophysical characterization of two BODIPY dyes. In order to assess the potential of using the dye as a fluorescent probe, Lysotracker Red, a commercial lysosomal marker, was investigated for comparison purposes. The results indicate that figure of merit of both compounds were three orders of magnitude higher than that of

Lysotracker Red. With an eye towards applications, one of the compounds was encapsulated in silica-based nanoparticles for *in vitro* and *ex vivo* one-photon and two-photon fluorescence imaging, in which the surface of the nanoparticle was modified with RGD peptides for specific targeting. The nanoprobe exhibited good biocompatibility and highly selective RGD-mediated uptake in $\alpha_V\beta_3$ integrin-overexpressing cancers, while maintaining efficient fluorescence quantum yield and high photostability. In chapter 4, the synthesis and photophysical properties of a novel photosensitizer with heavy atoms (halogen) were presented. The dye exhibited low fluorescence quantum yield, resulting in high singlet oxygen generation quantum yield. *In vitro* photodynamic studies demonstrated that photosensitization of the agent can induce cellular damage, subsequently leading to cell death by a necrotic cell death mechanism, supporting the therapeutic potential of using the agent for photodynamic therapy.

To my family

# ACKNOWLEDGMENTS

I would like to express my sincerest thanks to my advisor Dr. Kevin D. Belfield for his encouragement, support, and guidance throughout my Ph.D. journey. Without his constant motivation and expert instruction, this dissertation wouldn't have been possible. Being part of Dr. Belfield's research group has provided many great opportunities to collaborate with other respected scholars. Especially, I am deeply grateful to Dr. Yi Xiao at Dalian University of Technology in China for providing precious BODIPY compounds. Also, I would like to acknowledge Dr. Mikhailo V. Bondar for his advice and guidance in the photophysical characterization of many compounds. Thanks also to my committee members, Dr. Andres D. Campiglia; Dr. Shengli Zou; Dr. Gul Shad Ali; and Dr. Andrew Frazer for their time and support.

I would also like to thank my colleagues, the current and former members of Belfield research group for their support, comments, and friendship. Special thanks to Dr. Hyo-Yang Ahn for her instruction and patience. She served as a mentor to me during my Ph.D. studies. I am also very grateful to Dr. Binglin Sui, Dr. Yuanwei Zhang, Dr. Sheng Yao, and Dr. Taihong Liu for trusting me with their compounds. I would like to thank Dr. Xiling Yue for her help and suggestions with cell-related experiments. Also, thanks to other group members: Simon Tang, Dr. Adam Woodward, Dr. Mengyuan Wang, Dr. Andrew Frazer, Dr. Alma Morales, Dr. Bill Moreshead, Dr. Ciceron O. Yanez, and I wish you all the best.

Finally, I would like to give my deepest appreciation to my parents and my brother's family. Without their support and love, this dissertation wouldn't have been accomplished.

# TABLE OF CONTENTS

LIST OF FIGURES ..... xii

LIST OF TABLES ..... xvii

LIST OF SCHEMES ..... xviii

LIST OF ACRONYMS AND ABBREVIATIONS ..... xix

CHAPTER 1. INTRODUCTION ..... 1

1.1 Background and Importance ..... 1

1.2 Dissertation Statement ..... 5

1.3 Dissertation Outline ..... 5

CHAPTER 2. LONG-WAVELENGTH, PHOTOSTABLE, TWO-PHOTON EXCITABLE AND SUBCELLULAR ORGANELLE-TARGETABLE FLUORESCENT PROBES FOR BIOLOGICAL IMAGING ..... 7

2.1 Abstract ..... 7

2.2 Introduction ..... 8

2.3 Results and Discussion ..... 11

2.3.1 Design and Synthesis of Long-Wavelength BODIPY Derivatives: SPC, DC-SPC, DPC, DC-DPC ..... 11

2.3.2 Fundamental Optical Properties and Photostability ..... 12

2.3.3 DFT Calculations ..... 17

2.3.4 Single-Molecule Experiment ..... 19

2.3.5 Mitochondrial Targetable Fluorescent Probe and its Application for Biological Imaging ..... 20

2.3.6 Lysosomal Targetable Fluorescent Probe and its Application for Biological Imagining ..... 22

2.3.7 In Vitro Photodecomposition Experiments ..... 27

2.3.8 Cytotoxicity Study ..... 28

2.4 Conclusion ..... 29

2.5 Experimental Section ..... 30

2.5.1 Materials ..... 30

2.5.2 General Methods ..... 30

2.5.3 Effects on Cell Growth/Viability ..... 31

2.5.4 Culture of MCF-7 Cells and Fluorescent Imaging ..... 32

2.5.5 Single-Molecule Experiments ..... 33

2.5.6 Photostability ..... 34

2.5.7 2PA Cross-Section Measurements ..... 35

2.5.8 General Procedure for the Synthesis of BODIPY Derivatives ..... 35

CHAPTER 3. NEAR-INFRARED FLUORESCENT 4,4-DIFLUORO-4-BORA-3A,4A-DIAZA-S-INDACENE PROBES FOR ONE-PHOTON AND TWO-PHOTON FLUORESCENCE BIOIMAGING ..... 40

3.1 Abstract ..... 40

3.2 Introduction ..... 40

3.3 Results and Discussion ..... 43

3.3.1 Linear and Nonlinear Photophysical Properties ..... 43

3.3.2 Cytotoxicity and in Vitro One-photon and Two-photon Fluorescence Lysosomal Imaging ..... 48

3.3.3 Characterization of RGD-Modified SDC-Doped SiNPs ..... 51

3.3.4 RGD Receptor-Targeted in Vitro and ex Vivo 1PFM and 2PFM Imaging with SiNPs ..... 52

3.4 Conclusion ..... 54

3.5 Experimental Section ..... 55

3.5.1 Synthesis ..... 55

3.5.2 Linear Optical Properties ..... 58

3.5.3 Nonlinear Optical Properties ..... 59

3.5.4 Photostability ..... 60

3.5.5 Preparation and Characterization of Dye-encapsulating SiNPs ..... 61

3.5.6 Cytotoxicity Assay ..... 62

3.5.7 Uptake of DDC by Cancer Cells ..... 63

3.5.8 Uptake of SiNPs by Cancer Cells ..... 63

3.5.9 Ex Vivo Studies ..... 64

3.5.10 One-photon Fluorescence Microscopy (1PFM) and Two-photon Fluorescence Microscopy (2PFM) Lysosomal Imaging ..... 64

3.5.11 RGD Receptor-Targeted in Vitro and ex Vivo 1PFM and 2PFM Imaging with SiNPs ..... 65

CHAPTER 4. *IN VITRO* PHOTODYNAMIC STUDIES OF NOVEL BODIPY DYE ..... 66

4.1 Abstract ..... 66

4.2 Introduction ..... 66

4.3 Results and Discussion ..... 67

4.4 Conclusion ..... 73

4.5 Experimental Section ..... 74

4.5.1 Synthesis ..... 74

4.5.2 Photophysical Properties ..... 76

4.5.3 Cytotoxicity Assay ..... 77

4.5.4 In Vitro Photosensitization Assay ..... 78

4.5.5 Live Cell Imaging ..... 78

APPENDIX A: PUBLICATIONS TO DATE FROM DISSERTATION WORK ..... 79

APPENDIX B: SUPPORTING INFORMATION OF CHAPTER 2 ..... 81

APPENDIX C: SUPPORTING INFORMATION OF CHAPTER 3 ..... 99

APPENDIX D: SUPPORTING INFORMATION OF CHAPTER 4 ..... 107

LIST OF REFERENCES ..... 112

# LIST OF FIGURES

**Figure 1:** Jablonski diagram. ..... 2

**Figure 2:** (a) Jablonski diagram for one-photon and two-photon excitation. (b) Localization of excitation by one-photon excitation (380 nm, left beam) versus two-photon excitation (760 nm, right beam). ..... 3

**Figure 3:** Deep vascular imaging in wounds by two-photon fluorescence microscopy. ..... 4

**Figure 4:** (a) Normalized absorption spectra, (b) normalized fluorescence spectra, and (c) two-photon absorption spectra of **SPC**, **DPC**, **DC-SPC**, and **DC-DPC** in chloroform. ..... 13

**Figure 5:** Fluorescence intensity decay of **SPC**, **DPC**, **DC-SPC**, **DC-DPC**, and Cy5 in chloroform with irradiation by a 500 W iodine-tungsten lamp. $I_0$ is the fluorescence intensity immediately after the irradiation. $I$ is the fluorescence intensity of the above compounds after a fixed time of irradiation. ..... 17

**Figure 6:** (A) DFT optimized structure of **DC-DPC** in the ball-and-stick representation. (B) The HOMO and LUMO electron distribution of **DC-DPC**. ..... 18

**Figure 7:** Single-molecule imaging of a PMMA film containing Cy5 (A) and **DPC** (B), respectively. The excitation wavelength is 656 nm, and laser intensity at the sample is approximate 0.25 kW/cm$^2$. (C) The spatially integrated fluorescence intensity time traces of the representative individual molecule, red for Cy5 and orange for **DPC**. The reported intensity is background-subtracted. Because of photobleaching, the emission terminates at 2 and 4.5 s for Cy5 and **DPC**, respectively. ..... 20

**Figure 8:** MCF-7 cells are costained with (A) 25 nM Rh-123 ($\lambda_{ex}$ = 488 nm, $\lambda_{em}$ = 500−560 nm, pseudo-color green) and (B) 37.5 nM **DC-SPC-PPh3** ($\lambda_{ex}$ = 559 nm, $\lambda_{em}$ = 600−660 nm, pseudo-

color red) (1 h at 37 °C, 5% $CO_2$) in PBS. (C) Overlay of (A), (B), and brightfield. (D) Intensity profile of region of interest (ROI) cross MCF-7 cell. ..... 21

**Figure 9:** MCF-7 cells are stained with 37.5 nM **DC-SPC-PPh3** (1 h at 37 °C, 5% $CO_2$) in PBS. (A) and (B) are 1PFM ($\lambda_{ex}$ = 559 nm, $\lambda_{em}$ = 600−660 nm, pseudo-color red) and 2PFM ($\lambda_{ex}$ = 900 nm, $\lambda_{em}$ = 600−660 nm, pseudo-color red) images of MCF-7 cells stained by **DC-SPC-PPh3**. . 22

**Figure 10:** MCF-7 cells are co-stained with (A) 25 nM NR ($\lambda_{ex}$ = 559 nm, $\lambda_{em}$ = 575−640 nm, pseudo-color red) and (B) 37.5 nM **DC-DPC-PPh3** ($\lambda_{ex}$ = 635 nm, $\lambda_{em}$ = 655−755 nm, pseudo-color green) (2 h at 37 ℃ 5% $CO_2$) in PBS. (C) Overlay of (A), (B), and brightfield. (D) Intensity profiles of region of interest (ROI) cross MCF-7 cell. ..... 23

**Figure 11:** HCT 116 cells stained with 1 $\mu$M **DC-DPC-PPh3** (4 h at 37 °C, 5% $CO_2$) in medium. (A) 1PFM ($\lambda_{ex}$ = 633 nm, $\lambda_{em}$ = 700−800 nm, pseudo-color green) and (B) 2PFM ($\lambda_{ex}$ = 1000 nm, $\lambda_{em}$ = 700−800 nm, pseudo-color green)..... 23

**Figure 12:** MCF-7 cells co-stained with (A) Rh-123 (25 nM) ($\lambda_{ex}$ = 488 nm, $\lambda_{em}$ = 500−560 nm, pseudo-color red) and (B) **DC-DPC-PPh3** (37.5 nM) ($\lambda_{ex}$ = 635 nm, $\lambda_{em}$ = 655−775 nm, pseudo-color green) (2 h at 37 ℃ 5% $CO_2$) in PBS. (C) Overlay of (A), (B), and brightfield. (D) Intensity profiles of region of interest (ROI) cross MCF-7 cell. ..... 24

**Figure 13:** Changes of intensity plot of **DC-DPC-PPh3** (3 $\mu$M) at 745 nm vs different pH value. Inset: changes in fluorescence spectra of **DC-DPC-PPh3** in aqueous solution containing 30% acetonitrile as cosolvent vs different pH. ($\lambda_{ex}$: 690 nm slit: 3 nm, 3 nm.). ..... 26

**Figure 14:** Fluorescence images of MCF-7 costained with NR (channel 1, pseudo-color red) and **DC-DPC-PPh3** (channel 2, pseudo-color green) stimulated with chloroquine. (a−d) Images from

channel 1 after chloroquine-stimulation for 0 min, 5 min, 10 min and 20 min; (e) overlay of (d) and brightfield; (f−i) Images from channel 2 after chloroquine-stimulation for 0 min, 5 min, 10 min and 20 min; (j) overlay of (i) and brightfield; (k−n) Merged images of channel 1 and channel 2; (o).Normalized fluorescence intensity change of ROIs from two channels respectively..... 26

**Figure 15:** Photofading of dyes (a, **DC-SPC-PPh3**, Rh123, and TMRM) and (b, **DC-DPC-PPh3** and Cy5) in living cells with irradiation by semiconductor laser in a confocal fluorescence microscope. (a) Excitation wavelength is 488 nm for Rh-123, 559 nm for TMRM and **DC-SPC-PPh3**, and the intensity at the sample is approximately 0.5 mW. (b) Excitation wavelength is 635 nm for **DC-DPC-PPh3** and Cy5 and the intensity at the sample is approximately 0.5 mW. ..... 27

**Figure 16:** Viability of MCF-7 cells with **DC-SPC-PPh3** (red) and **DC-DPC-PPh3** (black) after treatment in different concentrations for 24 h..... 28

**Figure 17:** Normalized one-photon absorption (a, c) and fluorescence emission (b, d) spectra of **DDC** (top), **SDC** (bottom) in toluene (black), dichloromethane (red), dimethyl sulfoxide (green), acetonitrile (blue), and **SDC-SNP** (bottom) in water (pink)..... 45

**Figure 18:** Linear and nonlinear optical spectra of (a) **DDC** in DMSO and (b) **SDC** in DMSO (1 GM (Göppert Mayer) = $10^{-50}$·$cm^4$·s·$photon^{-1}$). Linear absorption (black), emission (red), excitation anisotropy (blue) spectra, and 2PA cross sections (green circles). ..... 46

**Figure 19:** Time-dependent absorption spectra of (a) **DDC** in DMSO, and (b) LT Red in DMSO, (c) **SDC** in DMSO, and (d) **SDC-SNP** in water with corresponding wavelength irradiation. ..... 48

**Figure 20:** Colocalization images of HCT 116 cells coincubated with **DDC** (10 $\mu$M, 4 h) and LT Red (100 nM, 2 h). Row B shows magnification of area enclosed by the blue box in Row A. (a) differential interference contrast (DIC) image, (b) one-photon fluorescence image of **DDC**, (c)

one-photon fluorescence image of LT Red, (d) overlaid image of b and c, (e) overlaid image of a, b, and c (Pearson's correlation coefficient 0.88). 50 $\mu$m scale bar ..... 50

**Figure 21:** Images of HCT 116 cells incubated with **DDC** (10 $\mu$M, 4 h). (a) DIC image, (b) one-photon fluorescence image, and (c) two-photon fluorescence image. ..... 51

**Figure 22:** One-photon fluorescence (a-c) and DIC overlay (d-f) images in U87MG cells. Control group (a, d), **RGD-SDC-SNP** incubated group (b, e), and RGD-blocked group (c, f). 10 $\mu$m scale bar ..... 53

**Figure 23:** 2PFM images of tumor tissue co-stained with **RGD-SDC-SNP** (red) and Hoechst (green) in the view of X-Y plane (a, b) and 3D reconstruction (c, d). ..... 54

**Figure 24:** Z-scan experiment setup, (1) 100% reflection mirrors, (2) focusing lens, (3) pinhole, (4) neutral density filter, and (5) beam splitter. ..... 60

**Figure 25:** (A) Normalized absorption (black), emission (red), and excitation (green) spectra of **BDP 3** in ACN. (B) Near-infrared singlet oxygen luminescence spectra of **BDP 3** (red) and Acridine (black) in ACN. ..... 70

**Figure 26:** (A) Dark cytotoxicity toward LLC cells after incubation with increasing concentrations of **BDP 3**. (B) Cell viability of LLC cells in the absence (blue) or presence (red) of 10 $\mu$M of **BDP 3** under a different period of irradiation time in the spectral range 502-542 nm. ..... 71

**Figure 27:** Differential interference contrast, DIC, (A, D) and confocal fluorescence (B, E) images of LLC cells stained with propidium iodide after irradiation in the absence (A−C) or presence (D−F) of **BDP 3**. Scale bars show 50 $\mu$m. ..... 72

**Figure 28:** DIC images of LLC cells after irradiation in the absence (A, B) or presence (C, D) of **BDP 3**. Scale bars show 100 $\mu$m..... 73

# LIST OF TABLES

**Table 1**: Photophysical Properties of **SPC**, **DPC**, **DC-SPC**, **DC-DPC**, **DC-SPC-PPh3**, and **DC-DPC-PPh3**. ..... 15

**Table 2:** DFT Calculation Results[a]. ..... 19

**Table 3:** Linear Photophysical Properties for **DDC**, **SDC**, **RGD-SDC-SNP**, and LT Red..... 44

**Table 4:** Photochemical Decomposition Quantum Yields and Figure of Merits of **DDC**, **SDC**, **RGD-SDC-SNP**, and LT Red. ..... 47

**Table 5:** Photophysical Properties for **BDP 3** and Acridine ..... 69

# LIST OF SCHEMES

**Scheme 1:** Synthetic procedures for **SPC**, **DPC**, **DC-SPC**, **DC-DPC**, **DC-SPC-PPh3**, and **DC-DPC-PPh3**[a] ..... 10

**Scheme 2:** Synthesis of **SDC** and **DDC**. ..... 56

**Scheme 3:** Synthetic route for **BDP 3**. ..... 68

# LIST OF ACRONYMS AND ABBREVIATIONS

| | |
|---|---|
| Abs | Absorption |
| ACN | Acetonitrile |
| RGD | Arginine-Glycine-Aspartic acid |
| $CDCl_3$ | Deuterated chloroform |
| DCM | Dichloromethane |
| DM | Dichroic mirror |
| DIC | Differential interference contrast |
| DMSO | Dimethylsulfoxide |
| DLS | Dynamic light scattering |
| Em | Emission |
| Ex or Exc | Excitation |
| fs | Femtosecond ($10^{-15}$ s) |
| $F_M$ | Figure of merit |
| $\tau$ | Fluorescence lifetime |
| $\Phi_f$ or $\Phi_{FL}$ | Fluorescence quantum yield |
| FWHM | Full width at half maximum |
| GM | Göppert-Mayer unit for the two-photon absorption cross section ($10^{-50}$ $cm^4$ s photon$^{-1}$ molecule$^{-1}$) |
| ISC | Intersystem crossing |
| ICT | Intramolecular charge transfer |
| kW | Kilowatt ($10^3$ W) |

| | |
|---|---|
| $\lambda_{Abs}$ | Maximum wavelength of absorption |
| $\lambda_{Em}$ | Maximum wavelength of emission |
| MHz | Megahertz ($10^{6}$ Hz) |
| μL | Microliter ($10^{-6}$ L) |
| μm | Micrometer ($10^{-6}$ m) |
| μM | Micromolarity ($10^{-6}$ M) |
| mJ | Millijoule ($10^{-3}$ J) |
| mL | Milliliter ($10^{-3}$ L) |
| mM | Millimolarity ($10^{-3}$ M) |
| ε | Molar absorption coefficient |
| M | Molarity |
| nm | Nanometer ($10^{-9}$ m) |
| nM | Nanomolarity ($10^{-9}$ M) |
| ns | Nanosecond ($10^{-9}$ s) |
| NMR | Nuclear magnetic resonance |
| NIR | Near-infrared |
| 1PA | One-photon absorption |
| 1PFM | One-photon fluorescence microscopy |
| OD | Optical density |
| η | Photodecomposition quantum yield |
| PDT | Photodynamic therapy |
| PET | Photoinduced electron transfer |

| | |
|---|---|
| PMT | Photomultiplier tube |
| pTHF | Polytetrahydrofuran |
| ROS | Reactive oxygen species |
| ROI | Region of interest |
| SiNPs | Silica nanoparticles |
| $^1O_2$ | Singlet oxygen |
| SOG | Singlet oxygen generation |
| $\Phi_\Delta$ | Singlet oxygen generation quantum yield |
| $\Delta\lambda$ | Stokes shift |
| THF | Tetrahydrofuran |
| TOL | Toluene |
| TPP | Triphenylphosphonium |
| 2PA | Two-photon absorption |
| $\delta_{2PA}$ | Two-photon absorption cross section |
| 2PFM | Two-photon fluorescence microscopy |
| UV | Ultraviolet |
| W | Watt |

# CHAPTER 1. INTRODUCTION

## 1.1 Background and Importance

Over the past several decades the phenomenon of luminescence (categorized by fluorescence and phosphorescence) has received great attention in the field of biological science. According to quantum theory, when matter consisting of molecules or atoms absorbs the energy of a photon, an electron in matter is excited from the ground state to a higher energy state, producing electronically-excited species. The electron in the excited state can rapidly return to the ground state by the emission of light (luminescence).

The electronic energy states of a molecule, and transitions possible between them are illustrated by the Jablonski diagram in Figure 1. Following light absorption, a molecule can be excited from the singlet ground state ($S_0$) to some higher singlet excited state ($S_1$, $S_2$, or $S_n$) and generally relaxes to the lowest vibrational level of $S_1$ through non-radiative internal conversion. Consequently, it returns to $S_0$ via one of several ways, e.g., fluorescence or non-radiative internal conversion. Typically, transitions between states with the same spin multiplicity (e.g., $S_1 \rightarrow S_0$) are allowed, whereas transitions between two states of different spin multiplicity (e.g., $S_1 \rightarrow T_1$) are forbidden with a few exceptions. The transitions to triplet excited states may occur through the process of intersystem crossing (ISC) by spin-orbit coupling. Subsequently, the molecule in the $T_1$ state can undergo secondary radiative relaxation called phosphorescence.

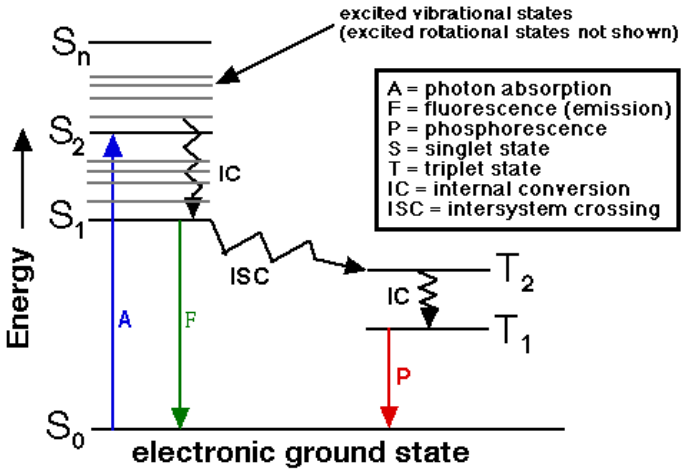


**Figure 1:** Jablonski diagram.

Source: http://www.shsu.edu/chm_tgc/chemilumdir/JABLONSKI.html

In 1931, Maria Göppert-Mayer proposed the concept of two-photon absorption (2PA) in her doctoral dissertation, in which a molecule absorbs two photons simultaneously (Figure 2(a)), and was later awarded the Nobel Prize in Physics for this work.[1] This concept had not been demonstrated until the advent of the laser in the beginning of the 1960s because no real 2PA had been observed with conventional light sources. Since 1961, when the first observation of 2PA was reported,[2] scientists and engineers have been inspired to study a new research area of multiphoton spectroscopy.

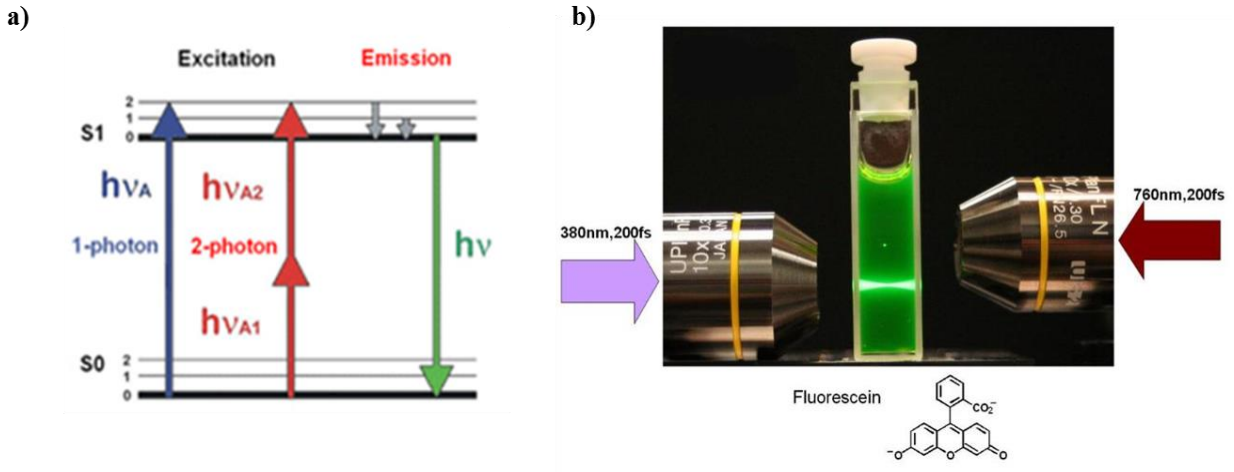


**Figure 2:** (a) Jablonski diagram for one-photon and two-photon excitation. (b) Localization of excitation by one-photon excitation (380 nm, left beam) versus two-photon excitation (760 nm, right beam).

Source: http://www.setabiomedicals.com/two_photon_appl.php
http://chemistry.cos.ucf.edu/belfield/photophysics

The primary difference between one-photon absorption (1PA) and 2PA is that 2PA is a nonlinear process in which it exhibits a quadratic dependence on the incident light intensity, while 1PA has a linear relationship to the incident excitation. Also, given that the 2PA wavelength can be twice the wavelength of 1PA, 2PA may occur in the far-red to near-infrared (NIR) region. This range is known as the biological tissue transparency window (700−1000 nm). In bioimaging applications, therefore, these characteristics afford a highly localized focal spot, where there is reasonable probability of two photons being absorbed at the same time, deeper light penetration as well as less photobleaching and reduced photodamage (Figure 2(b)).[3] The benefit of using 2PA can be evidenced by three-dimensional (3D) imaging of wound healing tissue captured by two-photon fluorescence microscopy (2PFM) in Figure 3.

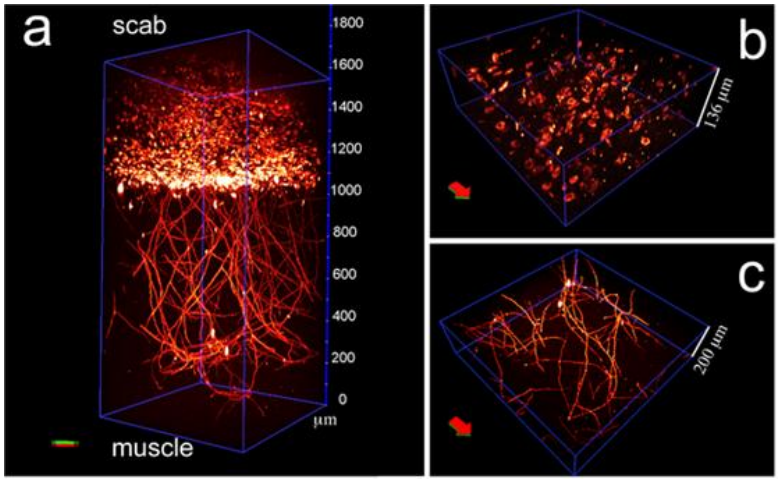


**Figure 3:** Deep vascular imaging in wounds by two-photon fluorescence microscopy.

Source: http://dx.doi:10.1371/journal.pone.0067559

As cancer has become a great concern around the world, there have been substantial research efforts in cancer diagnosis and therapy. One of the most significant problems associated with conventional therapies, such as chemotherapy and radiotherapy, is that these therapies may destroy healthy cells because of the lack of tumor specificity. As a result, photodynamic therapy (PDT) has emerged as an alternative for the treatment of many cancers.[4] As mentioned above, certain molecules in the $S_1$ state may undergo a spin conversion to the $T_n$ state through the process of intersystem crossing (ISC). By introducing heavy atoms (e.g., halogens), the molecules can exhibit an internal heavy-atom effect, which enhances spin-orbit coupling and consequently the efficiency of ISC.[5] By combining these molecules with light and oxygen, the light-activated photosensitizers transfer energy to surrounding oxygen molecules ($^3O_2$), resulting in the formation of reactive oxygen species (ROS), such as singlet oxygen ($^1O_2$). The generated ROS can induce cellular damage, leading to cell death by apoptotic and/or necrotic process.[4, 6, 7]

## 1.2 Dissertation Statement

The main purpose of this dissertation is to address the information on the structure of two-photon absorbing fluorophores and their linear/nonlinear photophysical properties for biological applications. The phenomenon of two-photon absorption, since its first observation with the development of ultrafast laser sources, brought about the motivation for developing new two-photon absorbing materials, due to many advantages of using 2PA. Unlike 1PA, 2PA occurs at a more highly localized spot, where there is reasonable probability of two-photons being absorbed simultaneously. In addition, 2PA is proportional to the square of the incident intensity. With these nonlinear characteristics, two-photon fluorescence microscopy can provide excellent 3D images and deeper penetration depth, along with reduced photodamage. Herein, several organic molecules were designed and their photophysical properties were characterized, depending on materials and applications. Finally, *in vitro* and/or *ex vivo* experiments were conducted to demonstrate biophotonic potential.

## 1.3 Dissertation Outline

This dissertation is presented as follows: Chapter 1 provides the introduction of luminescence and 2PA, followed by their uses in biological applications. In chapter 2, a series of new BODIPY derivatives are introduced along with their comprehensive linear and nonlinear characteristics. Two promising compounds were further evaluated as NIR fluorescent probes using one-photon fluorescence microscopy (1PFM) and 2PFM. Chapter 3 renders an account of the design, synthesis, and photophysical characterization of two BODIPY dyes. In order to assess the potential as a subcellular-targetable probe, Lysotracker Red, a commercial lysosomal marker,

was investigated for comparison purposes. In the view of applications, one of the compounds was encapsulated in silica-based nanoparticles (SiNPs) for *in vitro* and *ex vivo* 1PFM and 2PFM bioimaging. In chapter 4, the synthesis and photophysical properties of a novel BODIPY-based photosensitizer with halogen atoms were presented. *In vitro* photodynamic activities were evaluated to further demonstrate the therapeutic potential of using the agent for PDT.

# CHAPTER 2. LONG-WAVELENGTH, PHOTOSTABLE, TWO-PHOTON EXCITABLE AND SUBCELLULAR ORGANELLE-TARGETABLE FLUORESCENT PROBES FOR BIOLOGICAL IMAGING

Reproduced with permission from: Xinfu Zhang, Yi Xiao, Jing Qi, Junle Qu, Bosung Kim, Xiling Yue, and Kevin D. Belfield *The Journal of Organic Chemistry* **2013**, 78 (18), 9153-9160.


## 2.1 Abstract

Near-infrared (NIR) fluorescent probes are increasingly popular in biological imaging and sensing, as long-wavelength (650−900 nm) excitation and emission have the advantages of minimum photodamage, deep tissue penetration, and minimum interference from autofluorescence in living systems. Here, a series of long-wavelength BODIPY dyes **SPC**, **DC-SPC**, **DPC**, and **DC-DPC** are synthesized conveniently and efficiently. They exhibit excellent photophysical properties in far-red to NIR region, including large extinction coefficient, high fluorescence quantum yield, good photostability, and reasonable two-photon absorption cross section. Comparison of single-molecular imaging confirms that **DPC** is a much more efficient and more photostable NIR fluorophore than commonly used Cy5. Also importantly, two kinds of convenient functionalization sites have been reserved; the aryl iodide for organometallic couplings and the terminal alkyne groups for click reactions. Further derivatives **DC-SPC-PPh3** and **DC-DPC-PPh3** exhibit specificity to localize in mitochondria and in lysosomes respectively. Since their long-wavelength emission at ~650 nm and ~740 nm respectively can efficiently avoid the spectral crosstalk with other probes emitting in the visible light region, **DC-SPC-PPh3**

and **DC-DPC-PPh3** will act as the standard colocalizing agents to estimate the other probes' local distribution. The introduction of triphenylphosphonium (TPP) moieties mediates their hydrophilic-lipophilic balance and makes **DC-SPC-PPh3** and **DC-DPC-PPh3** appropriate for cell labeling. Particularly, **DC-DPC-PPh3** with pH-independent fluorescence properties has demonstrated its constant lysosomal targetability and strong NIR emission in lysosomes in spite of the stimulant's alkalization effect, which is more desirable than most of previous pH-sensitive lysotrackers that lose their fluorescence or leave lysosomes when local pH rises. Superior photostability, low cytotoxicity, and two-photon excitable property demonstrate our probes' utilities for fluorescent imaging and sensing in cell biology.

## 2.2 Introduction

Near-infrared (NIR) fluorescent probes are increasingly popular in biological imaging and sensing, as long-wavelength (650−900 nm) excitation and emission have the advantages of minimum photodamage to biological samples, deep tissue penetration, and minimum interference from background autofluorescence by biomolecules in the living systems.[8, 9] However, as compared to the large amount and widespread use of the probes in the UV-visible region, the number of NIR probes is limited, and their practical applicability needs to be further improved.

The development of NIR fluorescent probes encounters bottlenecks produced by the lack of appropriate fluorophores. Up to now, the only common NIR fluorophores belong to cyanine dyes, such as Cy5 and Cy7.[10-12] Yet their photostability is unsatisfactory, and their fluorescence quantum yields are suboptimal.[13] Especially in real time imaging of living cells or tissues, photostability is an important feature that defines fluorescence dyes. This situation urges a few

research groups, including ours, to search for novel ones.[14-23] Recent examples include Si-rhodamines,[14, 15] AZA-Bodipys,[16-19] Changsha NIRs,[20] and squaraines,[23] etc. Even though photophysical properties of these new NIR fluorophores are enhanced to some extent, most of them have complex structures and involve tanglesome synthetic methodologies, which make their further derivatization to obtain probes very difficult to achieve.

Currently, there is also an urgent demand to develop organelle-targetable NIR probes that can be separable from the fluorescence windows of other probes emitting in the visible range. Subcellular organelle-specific probes provide an advantageous way to collect accurate local information from intracellular regions of interest. For this reason, a variety of organelle-specific probes are being explored.[24-26] Commercially available organelle-specific probes, such as the Mitotrackers that stain mitochondria specifically, and Lysotrackers that localize in lysosomes, have made the exploitation of other new specific probes easier, as they can act as colocalizing agents in cell imaging. Unfortunately, almost all of these commercial trackers have absorption and emission in the visible range (400−650 nm), which is also the spectrum range of most other fluorescent probes. Sometimes, spectral crosstalk is so serious that the colocalization becomes unreliable. Thus, new NIR organelle trackers will help in addressing this issue.

In this article, a series of new BODIPY (4,4-difluoro-4-bora-3a,4a-diaza-s-indacene) derivatives have been developed to overcome the problems during the development of NIR dyes (Scheme 1). These fluorophores emit intensive far-red to near-infrared fluorescence, they are photostable, and importantly they are easily prepared. Besides, two kinds of convenient functionalization sites have been reserved; the aryl iodide for organometallic couplings and the propargyl groups for click reactions. By attaching one or two triphenylphosphonium (TPP)

moieties to the above BODIPYs, we obtain positively charged probes, which specifically localize in mitochondria or lysosomes.

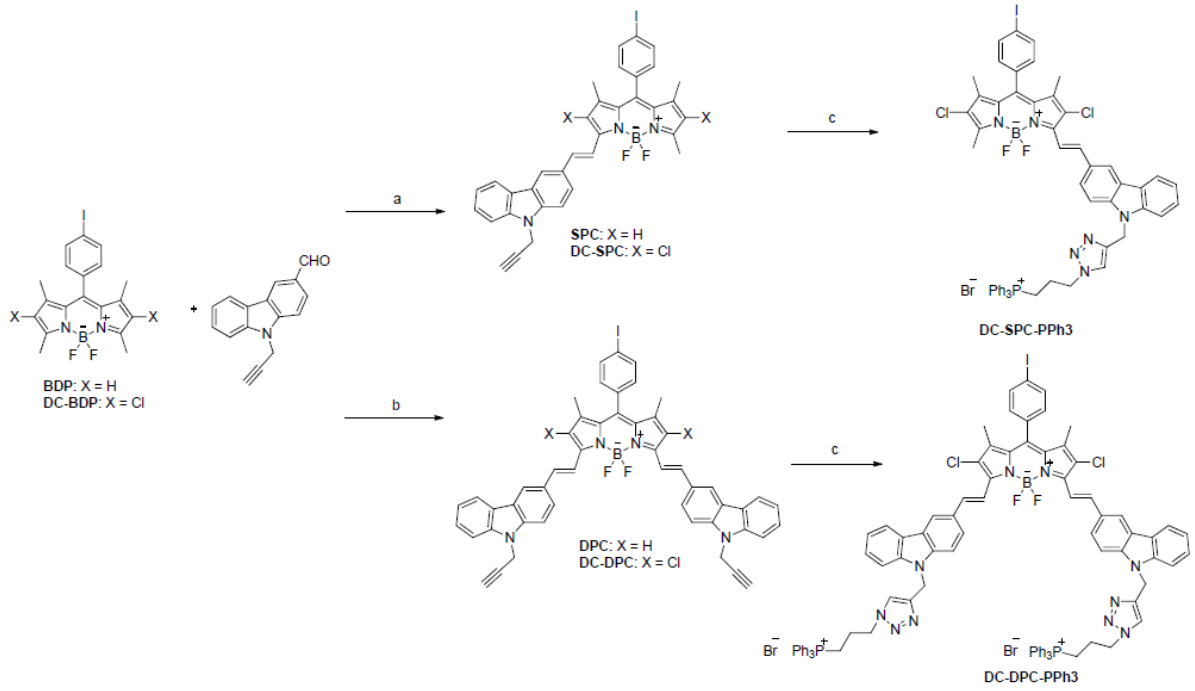


**Scheme 1:** Synthetic procedures for **SPC**, **DPC**, **DC-SPC**, **DC-DPC**, **DC-SPC-PPh3**, and **DC-DPC-PPh3**[a].

[a]Conditions: (a) Piperidine, acetic acid, toluene, reflux by using a Dean-Stark trap, 8 h. (b) Piperidine, acetic acid, anhydrous magnesium perchlorate, toluene, reflux by using a Dean-Stark trap, 8 h. (c) (3-Azidopropyl)-triphenylphosphonium bromide, DIPEA, $CuSO_4$, sodium ascorbate, alcohol, $H_2O$, toluene, room temperature, overnight.

## 2.3 Results and Discussion

### *2.3.1 Design and Synthesis of Long-Wavelength BODIPY Derivatives: SPC, DC-SPC, DPC, DC-DPC*

Long-wavelength and convenient derivative approaches are mainly considered during the designing of these BODIPY dyes. Two strategies, extending π-conjugations[27, 28] and forming moderate ICT (Intramolecular Charge Transfer)[29-32] structures, are general methods employed in designing long-wavelength dyes. The former usually results in long-wavelength derivatives that inherit the excellent optical properties from the BODIPY precursors, but in many cases it requires superb synthetic skills; for example, much research has fused aromatic or heterocyclic rings to the BODIPY core via relatively long synthetic routes.[33, 34] The ICT strategy is very effective in producing red shifts and is relatively easy to realize in synthesis. However, the reported BODIPY derivatives of strong ICT character lose some of the typical characteristics of the family. In highly polar media, a significant decrease in fluorescence intensity and broadening in fluorescence spectra are observed.[29, 35] According to our previous work, introduction of the carbazole group to BODIPY core will optimize spectral properties.[36, 37] It is a good choice that combines the above two strategies, because of its aromaticity and moderate ICT strength. On the other hand, the aryl iodide and the propargyl groups through carbazole are designed in BODIPY dyes. These dyes can be further functionalized through organometallic couplings or click reactions, which are important for NIR dyes to be applied.

As shown in Scheme 1, BODIPY dyes **SPC**, **DPC**, **DC-SPC**, and **DC-DPC** have been synthesized efficiently and in high yield by the classical Knoevenagel condensation of 3,5-dimethyl-BODIPY dyes with N-propargyl carbazole aldehyde. This strategy has been proven

efficient to extending π-conjugations by the research works of Rurack, Akkaya, and Ziessel, etc.[21, 22, 27-32] Knoevenagel reaction on the 3- and 5-methyl sites is in most cases high yielding and can be carried out in large scale. Moreover, chlorines on 2,6-positions may increase the electron density of the carbon atoms on 3,5-positions and then increase the condensation reactivity.[38] Thus, two parent BODIPY dyes are used, one of which, **DC-BDP**, is chlorosubstituent on the 2,6-positions. Knoevenagel condensation of **DC-BDP** proceeded more efficiently than that of **BDP**. In general, **DPC** and **DC-DPC**, the products of twice condensations, show satisfactory isolated yields of 75% and 80%, respectively. The monocondensations are also readily controllable by adjusting the mole ratio and stopping the reaction at a proper time to get **SPC** or **DC-SPC** with optimized yields of about 35%. Restricted by tanglesome synthetic methodologies, rarely new NIR fluorescent dyes have been further applied in medical analysis. Here, provision of larger quantities will not be a bottleneck for further applications of these BODIPY dyes. **DC-SPC** and **DC-DPC** are facilely functionalized via click chemistry into **DC-SPC-PPh3** and **DC-DPC-PPh3,** respectively, which possess the enhanced solubility in polar solvents and maintain similar photophysical properties. The introduction of triphenylphosphonium (TPP) moieties mediates their hydrophilic-lipophilic balance and makes **DC-SPC-PPh3** and **DC-DPC-PPh3** appropriate for cell labeling. All imaging experiments are carried out following the regular operation without worrying about its solubility in biological media.

### *2.3.2 Fundamental Optical Properties and Photostability*

These NIR dyes have been qualified for biological imaging by their outstanding optical characteristics. The normalized absorption and emission spectra in chloroform are recorded in

Figure 4, and the spectra data are listed in Table 1. These BODIPY dyes exhibit strong emission in the far-red to NIR region. After the introduction of chlorines and carbazole groups, the emission peak is pushed stepwise from about 500 to 614, 666, 703, and 749 nm. As compared to **SPC** and **DPC**, respectively, chlorides on 2,6-positions of **DC-SPC** and **DC-DPC** also cause red shift of about 40 nm for both absorption and emission. Importantly, these four long-wavelength fluorophores have inherited the BODIPY family's excellent photophysical properties, such as high molar extinction coefficient (70000−120000 $M^{-1}$ $cm^{-1}$), small FWHM (full width at half-maximum) of spectrum (37−48 nm), and high fluorescence quantum yield (e.g., 0.55−0.99 in chloroform; 0.40−0.96 in acetonitrile). Also, noticeably, in highly polar solvents such as DMSO, their emission spectra shift slightly relative to those in chloroform, and fluorescence quantum yields remain high, which indicates that they are also environmental factor-independent fluorophores as typical BODIPYs.[39] This is totally different from some previous long-wavelength BODIPY derivatives of apparent ICT character.

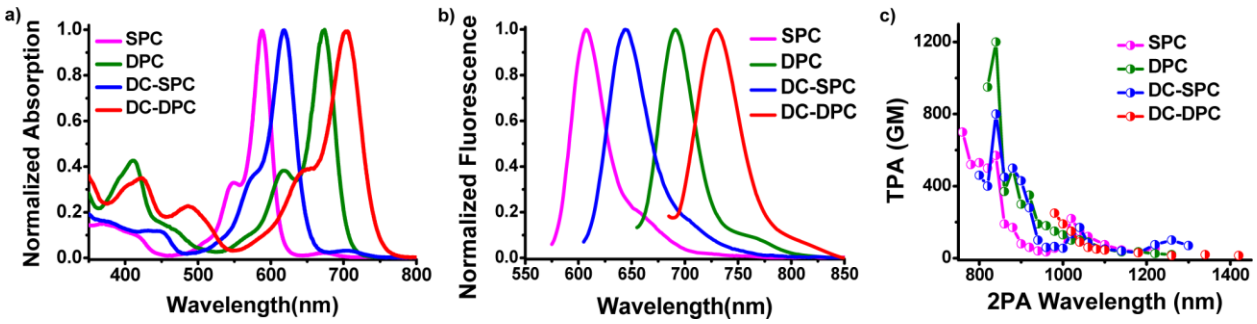


**Figure 4:** (a) Normalized absorption spectra, (b) normalized fluorescence spectra, and (c) two-photon absorption spectra of **SPC**, **DPC**, **DC-SPC**, and **DC-DPC** in chloroform.

The quantum yield is a result of competition between nonradiative deactivation processes and fluorescence emission.[16] To gain a better understanding this, fluorescence lifetimes ($\tau$) of these dyes were measured. Their lifetimes are approximately 4 ns (Table 1). Further, both radiative ($K_r$) and nonradiative ($K_{nr}$) decay rates (in relation to $\Phi_f$ and $\tau$) were calculated. The results show that the propensity of the radiative channel in the total decay is large enough, which means that these dyes emit intensely.

**Table 1**: Photophysical Properties of **SPC**, **DPC**, **DC-SPC**, **DC-DPC**, **DC-SPC-PPh3**, and **DC-DPC-PPh3**.

| dye | solvent | $\lambda_{Abs}$ (nm) | $\varepsilon$ ($M^{-1}$ $cm^{-1}$) | $\lambda_{Em}$ (nm) | $\Phi_f$ | $\tau$ (ns) | $K_r$ [d] ($10^8$ $s^{-1}$) | $K_{nr}$ [d] ($10^8$ $s^{-1}$) | $\delta$ [e] (GM) |
|---|---|---|---|---|---|---|---|---|---|
| **SPC** | chloroform | 588 | 124200 | 607 | 0.66[a] | 3.93 | 1.67 | 0.87 | 700 (760 nm) |
| | acetonitrile | 579 | 120800 | 605 | 0.77 | 4.03 | 1.91 | 0.57 | nd |
| | DMSO | 589 | 110600 | 614 | 0.72 | 3.64 | 1.98 | 0.77 | nd |
| **DC-SPC** | chloroform | 619 | 92800 | 644 | 0.62[a] | 4.24 | 1.46 | 0.89 | 800 (840 nm) |
| | acetonitrile | 606 | 92100 | 650 | 0.43 | 3.95 | 1.09 | 1.44 | nd |
| | DMSO | 616 | 77900 | 666 | 0.33 | 3.06 | 1.07 | 2.19 | nd |
| **DPC** | chloroform | 674 | 105900 | 691 | 0.99[b] | 4.00 | 2.48 | 0.02 | 1200 (840 nm) |
| | acetonitrile | 665 | 99600 | 688 | 0.96 | 4.14 | 2.32 | 0.10 | nd |
| | DMSO | 678 | 94900 | 703 | 0.97 | 3.61 | 2.69 | 0.08 | nd |
| **DC-DPC** | chloroform | 703 | 86100 | 730 | 0.55[b] | 3.97 | 1.39 | 1.13 | 250 (980 nm) |
| | acetonitrile | 694 | 68600 | 731 | 0.50 | 3.94 | 1.27 | 1.27 | nd |
| | DMSO | 705 | 68700 | 749 | 0.32 | 3.05 | 1.05 | 1.25 | nd |
| **DC-SPC-PPh3** | EtOH | 612 | 89800 | 650 | 0.40[a] | nd | nd | nd | nd |
| **DC-DPC-PPh3** | DCM | 704 | 98700 | 736 | 0.81[c] | nd | nd | nd | 450 (1000 nm) |
| | acetonitrile | 698 | nd | 745 | 0.69 | nd | nd | nd | nd |
| | DMSO | 712 | nd | 763 | 0.70 | nd | nd | nd | nd |

[a]Rhodamine B is used as standard. [b]Reported 3,5-bi (*p*-methoxy) phenyl-1,7-bi (*p*-bromo) phenyl aza-BODIPY ($\Phi_f$ 0.42, in toluene) is used as standard. [c]Cresyl violet is used as standard. [d]Radiative ($K_r$) and nonradiative ($K_{nr}$) decay rates. [e]Maximum two-photon absorption cross section, 1 GM = $10^{-50}$ $cm^4$ s $photon^{-1}$. nd, not determined.

The two-photon absorption (2PA) spectra have been measured through the femtosecond Z-scan technique, as shown Figure 4(c). These BODIPY dyes exhibit reasonable 2PA cross sections ($\delta$). Across the 760−1500 nm spectral window, **SPC**, **DC-SPC**, and **DPC** show maximum $\delta$ of 700, 800, and 1200 GM at 760, 840, and 840 nm, respectively. Although the NIR dye **DC-DPC** only gives a moderate $\delta$ of 250 GM at 980 nm, this might not be the real maximum, because Z-scan experiments were performed only in the 980−1400 nm range to rule out the interference from the long-wavelength one-photon absorption (1PA).

Our fluorophores, with combined two-photon excitation and long-wavelength emission, will be advantageous over commonly used two-photon fluorophores emitting in the visible range and common one-photon NIR emitters with poor two-photon activities. As is known, two-photon fluorescence microscopy (2PFM) has been gaining increased popularity in biological imaging because of its considerable imaging depth inside intact tissues (>500 $\mu$m), inherent three-dimensional resolution without out-of-focus fluorescence, and limiting photobleaching and photodamage to the focal volume.[40-43] However, the relatively short-wavelength emission of the most known two-photon fluorophores tends to be obscured in biological background fluorescence, which, to some extent, offsets the benefit of NIR two-photon excitation.

Photodecomposition experiments demonstrate that these BODIPY dyes have good photostability. Here, the photostability of these dyes is compared to that of a well-known NIR fluorophore Cy5 (Figure B-7, Appendix B) in chloroform. These BODIPY dyes show superior photostability over Cy5 (Figure 5). After irradiation by a 500 W iodine-tungsten lamp for 475 min, the fluorescence of these BODIPY dyes remains as high as 95%, while Cy5 is fully

bleached within 100 min. Enhanced photostability points to the advantage of these NIR fluorescence dyes for biological imaging applications.

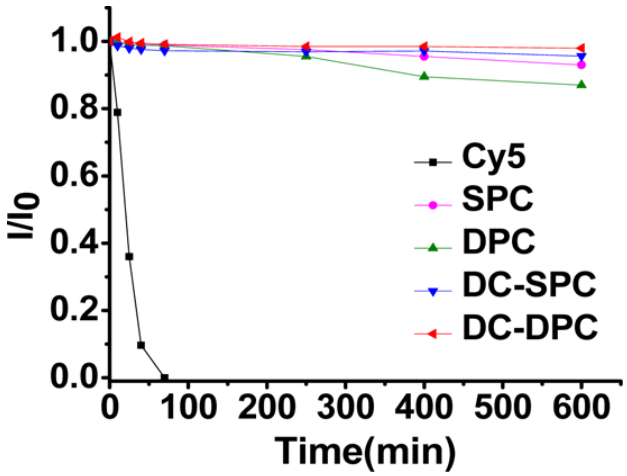


**Figure 5:** Fluorescence intensity decay of **SPC**, **DPC**, **DC-SPC**, **DC-DPC**, and Cy5 in chloroform with irradiation by a 500 W iodine-tungsten lamp. $I_0$ is the fluorescence intensity immediately after the irradiation. $I$ is the fluorescence intensity of the above compounds after a fixed time of irradiation.

### *2.3.3 DFT Calculations*

DFT calculations were carried out for further understanding of structure-property relationships,[44, 45] with part of the data listed in Table 2. The small dihedral angles (less than 10°) between the numbered atoms demonstrate high planarity between the BODIPY core and carbazole group (Figure 6(A) and Figure B-8, Appendix B). In addition, the HOMO and LUMO electron distribution of **DC-DPC** illustrates the transition dipole moment is larger than a typical $\pi-\pi^*$ transition (Figure 6(B) and Figure B-8, Appendix B). The above two results are in accordance with our design strategies: extending $\pi$-conjugations and forming moderate ICT. Moreover, HOMO and LUMO data show that the introduction of a carbazole group will raise the

HOMO energy level pronouncedly, and the introduction of chlorine will drop the LUMO energy level. It means smaller energy transitions and bathochromic shifts for **SPC**, **DC-SPC**, **DPC**, and **DC-DPC** as compared to **BDP**. Calculated absorption spectra show the general trend of red shift stepwise from 407 nm to 525, 565, 613, 654 nm, and these values are close to the experimental results. Another benefit from the quantum calculation is to estimate the lowest-lying singlet excited state, which is responsible for the emissive property of the fluorophore. According to the quantum mechanical selection rules, emissive properties (as well as the excitation) of a dye can be evaluated by the symmetry and the overlapping of the molecular orbitals (MOs), the change of the spin state, and the oscillator strength (*f*) of the electronic transitions, etc.[46-48] The DFT calculations demonstrate these NIR dyes bear a $S_1 \leftarrow S_0$ transition oscillator strength (*f*) of more than 1. This means the reverse transition, that is, $S_1 \rightarrow S_0$ transition, is also strongly allowed; thus, this dye is potentially fluorescent. These results are in good agreement with the experimental fluorescence quantum yield.

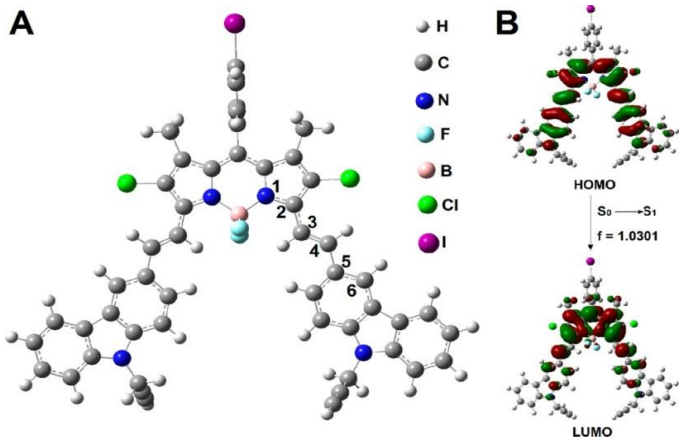


**Figure 6:** (A) DFT optimized structure of **DC-DPC** in the ball-and-stick representation. (B) The HOMO and LUMO electron distribution of **DC-DPC**.

**Table 2:** DFT Calculation Results[a].

| Dyes | $\varphi_{C1-C2-C3-C4}$[b] | $\varphi_{C3-C4-C5-C6}$[b] | energy (eV)[c] | $f$[d] | HOMO/LUMO (eV) |
|---|---|---|---|---|---|
| **BDP** | | | 3.05 (407 nm) | 0.4493 | -5.61/-2.61 |
| **SPC** | 6.99 | 0.84 | 2.36 (525 nm) | 1.2179 | -4.98/-2.58 |
| **DC-SPC** | 9.56 | 0.90 | 2.19 (565 nm) | 1.0939 | -5.22/-2.97 |
| **DPC** | 5.26 | 1.10 | 2.02 (613 nm) | 1.2271 | -4.68/-2.59 |
| **DC-DPC** | 2.82 | 1.84 | 1.89 (654 nm) | 1.0301 | -4.90/-2.91 |

[a]Calculations were carried out using the Gaussian 09 programs, employing the B3LYP functional. [b]$\varphi$ stands for dihedral angle between the numbered atoms. [c]Optical band gap and calculated absorption wavelength. [d]Oscillator strength of $S_1 \leftarrow S_0$ transition.

### *2.3.4 Single-Molecule Experiment*

Single-molecule imaging investigation also confirms **DPC** to be a very efficient and photostable NIR emitter. As the representative of these new BODIPYs, **DPC** is chosen for the comparison with Cy5, because they have similar absorption and emission wavelengths. Single-molecule imaging experiments are performed in PMMA (Figure 7). This is a standard test of a fluorophore to be used in imaging at single-molecule level, which requires bright fluorescence and robust photostability.[49-51] Typical time (Figure 7(C)) traces of single-molecule **DPC** and Cy5 illustrate that, in most cases, **DPC** single molecule exhibits longer surviving time (approximate 100 slides = 5000 ms) and higher emission rate (approximate 45000 photons per 50 ms). Hence, the total number of collected photons before bleaching of **DPC** will be much larger than that of Cy5 (about 4 times simply by integral area). Considering the long wavelength, as well as large

two-photon action cross section and good photostability in both bulk and single-molecule state, **DPC** exhibits obvious superiority over Cy5 as a NIR fluorophore.

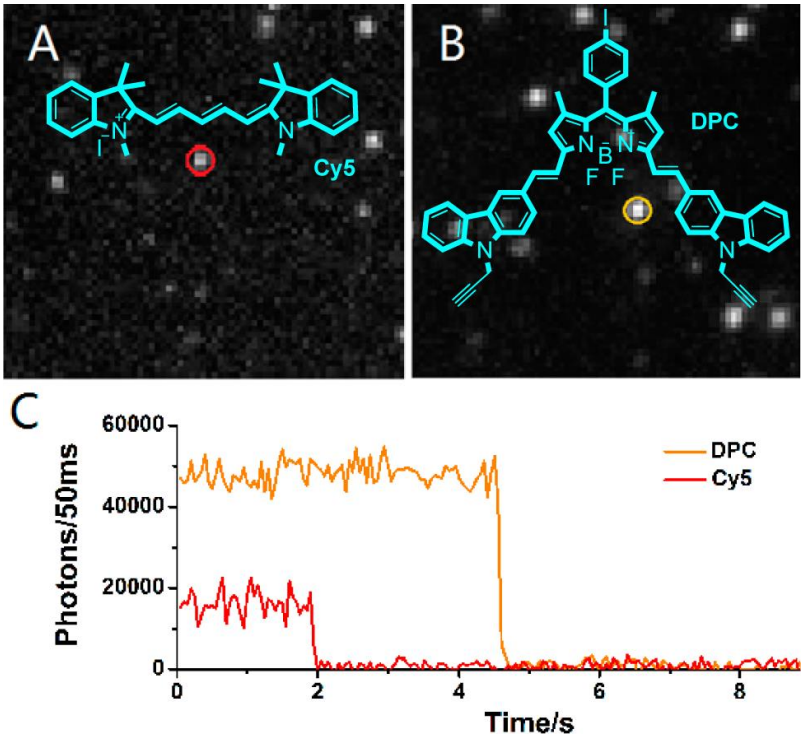


**Figure 7:** Single-molecule imaging of a PMMA film containing Cy5 (A) and **DPC** (B), respectively. The excitation wavelength is 656 nm, and laser intensity at the sample is approximate 0.25 kW/cm$^2$. (C) The spatially integrated fluorescence intensity time traces of the representative individual molecule, red for Cy5 and orange for **DPC**. The reported intensity is background-subtracted. Because of photobleaching, the emission terminates at 2 and 4.5 s for Cy5 and **DPC**, respectively.

### *2.3.5 Mitochondrial Targetable Fluorescent Probe and its Application for Biological Imaging*

**DC-SPC-PPh3** is then qualified as a useful mitochondrion tracker in both one-photon and two-photon fluorescence imaging experiments. Colocalization study of **DC-SPC-PPh3** with Rh-123 (Rhodamine 123, a commercial mitochondrial probe) has been conducted. As demonstrated in Figure 8, fluorescence intensity profiles of linear region of interest (ROI) across

MCF-7 cells stained with **DC-SPC-PPh3** and Rh-123 vary in close synchrony (Figure 8(D)). Pearson's coefficient and overlap coefficient are 0.863 and 0.887, respectively, evaluated using the conventional dye-overlay method (Figure B-9, Appendix B). Moreover, two-photon fluorescence images are collected to demonstrate the advantage of using **DC-SPC-PPh3** as a mitochondrial probe for 2PFM imaging. In Figure 9, the two-photon fluorescence image of MCF-7 cells is identical to the one-photon image. According to pioneering works of Chang and others,[52, 53] the mitochondrial targetability of **DC-SPC-PPh3** should be ascribed to the positively charged alkyltriphenylphosphonium (TPP) moiety.

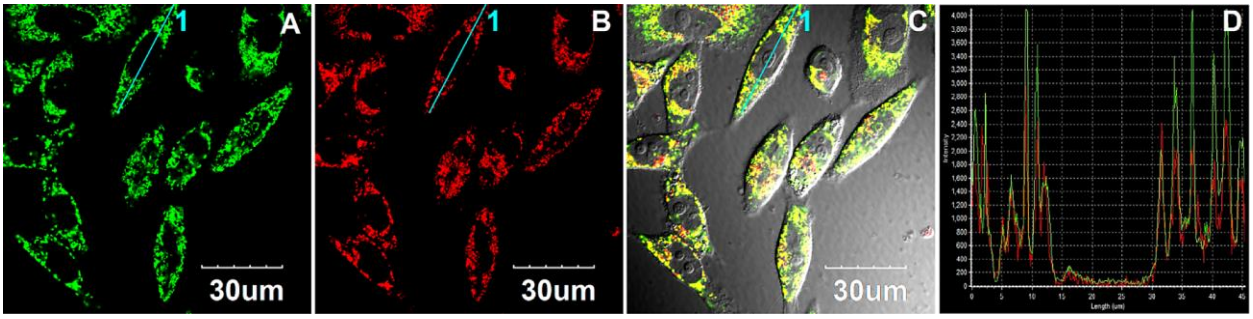


**Figure 8:** MCF-7 cells are costained with (A) 25 nM Rh-123 ($\lambda_{ex}$ = 488 nm, $\lambda_{em}$ = 500−560 nm, pseudo-color green) and (B) 37.5 nM **DC-SPC-PPh3** ($\lambda_{ex}$ = 559 nm, $\lambda_{em}$ = 600−660 nm, pseudo-color red) (1 h at 37 °C, 5% $CO_2$) in PBS. (C) Overlay of (A), (B), and brightfield. (D) Intensity profile of region of interest (ROI) cross MCF-7 cell.

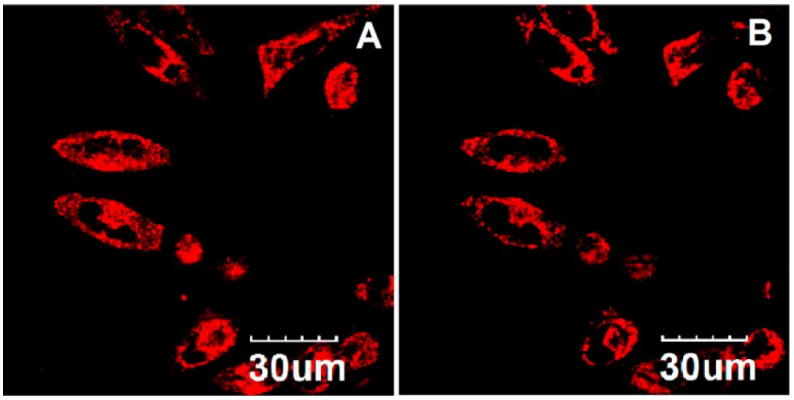


**Figure 9:** MCF-7 cells are stained with 37.5 nM **DC-SPC-PPh3** (1 h at 37 °C, 5% $CO_2$) in PBS. (A) and (B) are 1PFM ($\lambda_{ex}$ = 559 nm, $\lambda_{em}$ = 600−660 nm, pseudo-color red) and 2PFM ($\lambda_{ex}$ = 900 nm, $\lambda_{em}$ = 600−660 nm, pseudo-color red) images of MCF-7 cells stained by **DC-SPC-PPh3**.

### *2.3.6 Lysosomal Targetable Fluorescent Probe and its Application for Biological Imagining*

**DC-DPC-PPh3** displays good specificity to localize in lysosomes (Figure 10). Intensity profiles of ROI across MCF-7 cells stained with NR (Neutral Red, a commercial lysosomal probe) also vary in close synchrony (Figure 10(D)). Pearson's coefficient and overlap coefficient are 0.771 and 0.731 respectively in MCF-7 cells. Two-photon fluorescence images demonstrate the advantage of using **DC-DPC-PPh3** as a lysosomal probe for 2PFM imaging. In Figure 11, two-photon fluorescence image of HCT 116 cells is identical with one-photon image. To our knowledge, two-photon excitation over 1000 nm has not been commonly adopted. However, such a long-wavelength excitation might help increase the image depth further.

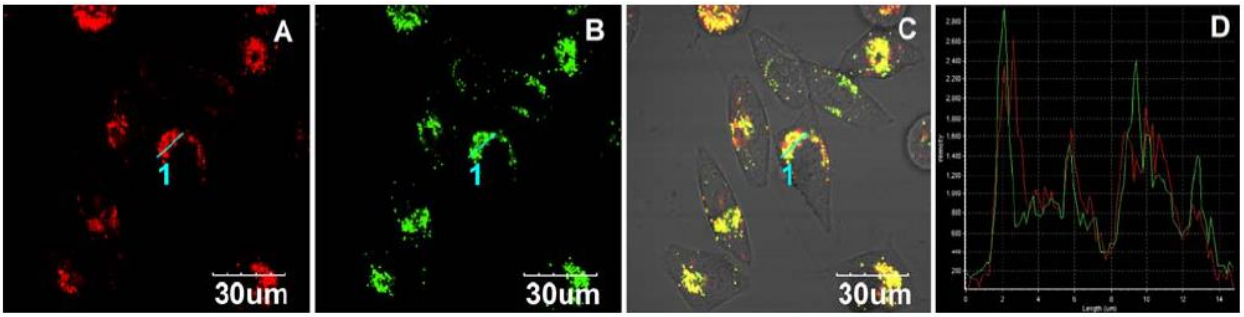


**Figure 10:** MCF-7 cells are co-stained with (A) 25 nM NR ($\lambda_{ex}$ = 559 nm, $\lambda_{em}$ = 575−640 nm, pseudo-color red) and (B) 37.5 nM **DC-DPC-PPh3** ($\lambda_{ex}$ = 635 nm, $\lambda_{em}$ = 655−755 nm, pseudo-color green) (2 h at 37 ℃ 5% $CO_2$) in PBS. (C) Overlay of (A), (B), and brightfield. (D) Intensity profiles of region of interest (ROI) cross MCF-7 cell.

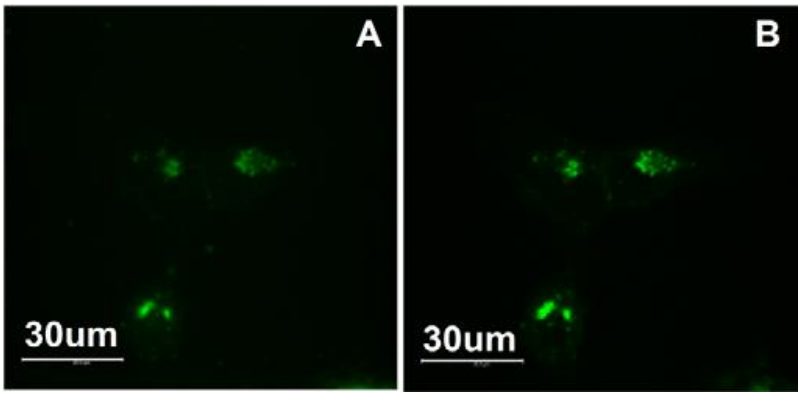


**Figure 11:** HCT 116 cells stained with 1 $\mu$M **DC-DPC-PPh3** (4 h at 37 °C, 5% $CO_2$) in medium. (A) 1PFM ($\lambda_{ex}$ = 633 nm, $\lambda_{em}$ = 700−800 nm, pseudo-color green) and (B) 2PFM ($\lambda_{ex}$ = 1000 nm, $\lambda_{em}$ = 700−800 nm, pseudo-color green).

As reported, the targetability of probes is controlled by competitive accumulation of probe by different cellular organelles.[54] However, in another colocalization imaging experiment, **DC-DPC-PPh3** and the mitotracker Rh-123 do not localize in the same intracellular regions (Figure 12), indicating that **DC-DPC-PPh3** is no longer mitochondria-targeting. This is an interesting discovery that deviates from the well-recognized knowledge on TPP moiety which usually enables probes selectively accumulate in mitochondria.[52, 53] Our explanation for **DC-**

**DPC-PPh3**'s preference to accumulate in lysosomes but not in mitochondria is that, when two TPP moieties exist in one molecule, the complex effect of the number of charge, different mol/ionic weight and different hydrophilicity-lipophilicity will result in different organelle selectivity.

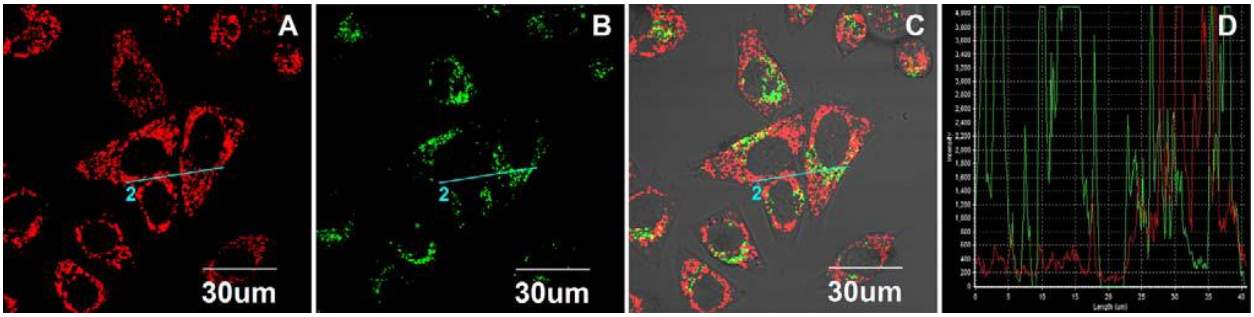


**Figure 12:** MCF-7 cells co-stained with (A) Rh-123 (25 nM) ($\lambda_{ex}$ = 488 nm, $\lambda_{em}$ = 500−560 nm, pseudo-color red) and (B) **DC-DPC-PPh3** (37.5 nM) ($\lambda_{ex}$ = 635 nm, $\lambda_{em}$ = 655−775 nm, pseudo-color green) (2 h at 37 ℃ 5% $CO_2$) in PBS. (C) Overlay of (A), (B), and brightfield. (D) Intensity profiles of region of interest (ROI) cross MCF-7 cell.

**DC-DPC-PPh3** also shows stable targeting-ability against lysosomal pH changes. The pH titration experiment reveals that fluorescence of **DC-DPC-PPh3** is insensitive to the change of pH (Figure 13). *In vitro* experiment for **DC-DPC-PPh3** shows stable fluorescence against drug-induced lysosomal pH changes in MCF-7. In this experiment, chloroquine that can cause the leakage of protons out of lysosomes is used to increase lysosomal pH.[55] Under co-staining condition, the addition of 20 $\mu$M chloroquine induces a clearly decrease of fluorescence intensities of NR within 20 min while fluorescence from **DC-DPC-PPh3** only shows a slight fluctuations possibly due to the migration of lysosomes (Figure 14) under chloroquine-

stimulation. Such stable fluorescence intensity independent on lysosomal pH change is quite important for correctly indicating the location and morphology of lysosomes.

To our knowledge, most lysosome-targeting probes, including commercial lysotrackers, bear alkaline groups (usually, amines) and thus their fluorescence is highly pH-sensitive owing to a protonation-induced switch-off of PET (photoinduced electron transfer) process:[56] they are strongly fluorescent only in acidic medium but weakly fluorescent or nonfluorescent at higher pH. There are also some lysosomal targeting probes whose targetability is dependent on acidic pH: the saltification of the basic side chains is the origin of their accumulation in acidic environment.[57-59] In other words, if the pH rises, the previous lysosomal probes will lose their fluorescence or will leave lysosomes to other intracellular areas. Indeed, these features are suitable for the 'healthy' lysosomes keeping acidic pH. However, ones should know, in a long time under physiologic conditions, pH values of the highly inhomogeneous lysosomes are always changing, and for lysosomes at different states the pH cannot be the same. More noticeably, under pathologic conditions, e.g., when lysosomes are stimulated by various external stimulants, it is highly recommended to adopt a pH-insensitive and stably targeting tracker to monitor the lysosomal migrations.

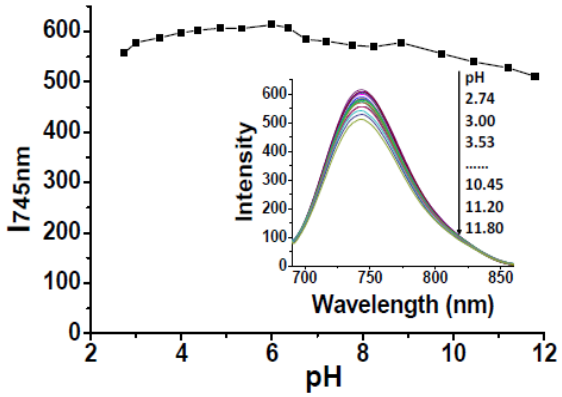


**Figure 13:** Changes of intensity plot of **DC-DPC-PPh3** (3 $\mu$M) at 745 nm vs different pH value. Inset: changes in fluorescence spectra of **DC-DPC-PPh3** in aqueous solution containing 30% acetonitrile as cosolvent vs different pH. ($\lambda_{ex}$: 690 nm slit: 3 nm, 3 nm.).

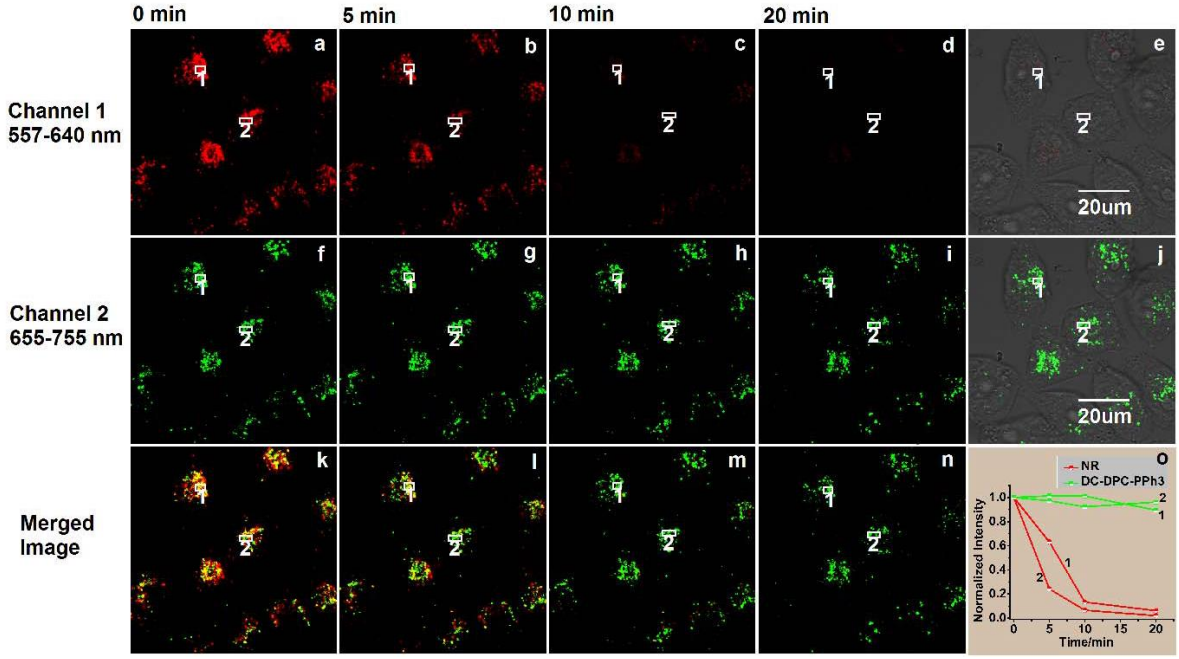


**Figure 14:** Fluorescence images of MCF-7 costained with NR (channel 1, pseudo-color red) and **DC-DPC-PPh3** (channel 2, pseudo-color green) stimulated with chloroquine. (a−d) Images from channel 1 after chloroquine-stimulation for 0 min, 5 min, 10 min and 20 min; (e) overlay of (d) and brightfield; (f−i) Images from channel 2 after chloroquine-stimulation for 0 min, 5 min, 10 min and 20 min; (j) overlay of (i) and brightfield; (k−n) Merged images of channel 1 and channel 2; (o).Normalized fluorescence intensity change of ROIs from two channels respectively.

### *2.3.7 In Vitro Photodecomposition Experiments*

*In vitro* photodecomposition experiments also reveal that **DP-SPC-PPh3** has much better photostability than widely used mitochondrial probes, such as Rh-123 and tetramethylrhodamine methyl ester (TMRM). After irradiation by semiconductor laser (488 nm for Rh-123, 559 nm for TMRM and **DC-SPC-PPh3**, 0.5 mW) on a confocal fluorescence microscope for 140 s, the fluorescence of **DC-SPC-PPh3** remained as high as 88%, while the other two showed obvious decreases, TMRM to 30% and Rh-123 to 9% (Figure 15(a)). In addition, it has been proven that **DP-DPC-PPh3** has better photostability than Cy5. After irradiation by semiconductor laser (635 nm, 0.5 mW) on a confocal fluorescence microscope for 300 s, the fluorescence of **DC-DPC-PPh3** appeared to remain as high as 90%, whereas Cy5 decreased to 30% (Figure 15(b)). Enhanced photostability demonstrates the advantage of **DC-SPC-PPh3** and **DC-DPC-PPh3** as first choice mitochondrial tracker and lysosomal tracker, respectively, in living cells.

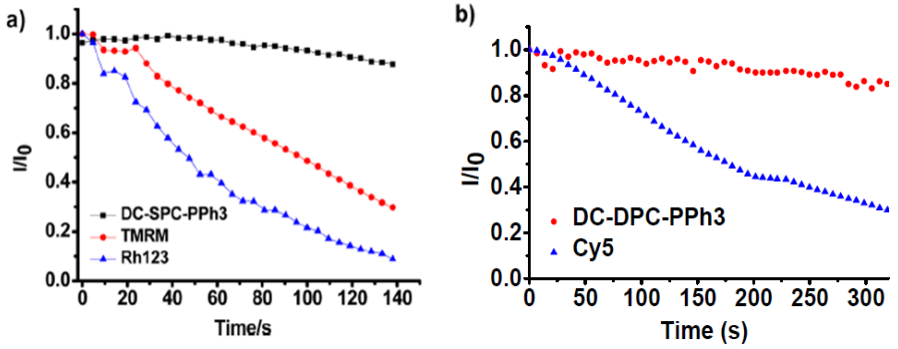


**Figure 15:** Photofading of dyes (a, **DC-SPC-PPh3**, Rh123, and TMRM) and (b, **DC-DPC-PPh3** and Cy5) in living cells with irradiation by semiconductor laser in a confocal fluorescence microscope. (a) Excitation wavelength is 488 nm for Rh-123, 559 nm for TMRM and **DC-SPC-PPh3**, and the intensity at the sample is approximately 0.5 mW. (b) Excitation wavelength is 635 nm for **DC-DPC-PPh3** and Cy5 and the intensity at the sample is approximately 0.5 mW.

### *2.3.8 Cytotoxicity Study*

The dark cytotoxicity of **DC-SPC-PPh3** and **DC-DPC-PPh3** is low (Figure 16). MTT assay has revealed that ~95% of MCF-7 cells survived after being incubated with **DC-SPC-PPh3** (10 $\mu$M) for 24 hours. This is a favorable characteristic of a practical mitochondrial probe applied in living cells. The result also shows that **DC-DPC-PPh3** has the advantage of low cytotoxicity. Even incubated with a much higher concentration (10 $\mu$M) than optimized level, 91% of MCF-7 cells survived after being incubated for 24 hours. As has been mentioned previously, most of the known lysosomal probes have alkalinity favorable for retention in acidic lysosomes. However, an alkalinizing effect to elevate pH values within lysosomes will interrupt lysosomal functions and lead to relatively high cytotoxicity. Our new lysotracker, **DC-DPC-PPh3**, doesn't have such effect, and thus shows low cytotoxicity.

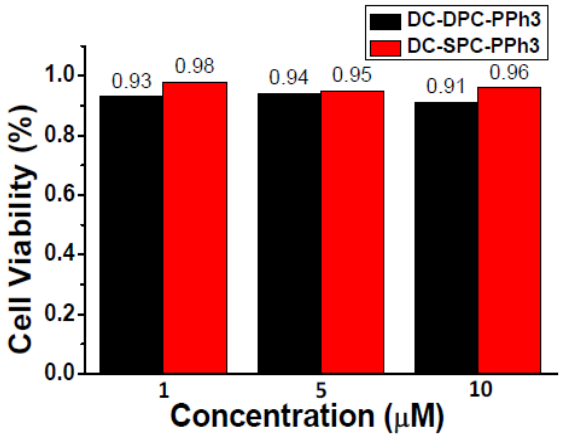


**Figure 16:** Viability of MCF-7 cells with **DC-SPC-PPh3** (red) and **DC-DPC-PPh3** (black) after treatment in different concentrations for 24 h.

## 2.4 Conclusion

In conclusion, in order to develop efficient and photostable long-wavelength fluorescent probes, we have synthesized a series of BODIPY derivatives such as **SPC**, **DPC**, **DC-SPC**, and **DC-DPC** in high yields through Knoevenagel condensation. These dyes emit at tunable wavelengths in the far-red to NIR region. For example, in chloroform their emission peak is 607, 644, 691, and 730 nm, respectively. Importantly, their fluorescence quantum yields are very high, regardless of the solvents' polarity. For example, in chloroform, these values are up to 0.66, 0.62, 0.99, and 0.55, respectively. They are much more efficient and much more photostable emitters than common NIR dyes, for example, Cy5, as proved by the comparison study of single-molecule fluorescence imaging. Another advantage lies in that they have reasonable two-photon absorption across sections. These precursors bearing terminal acetylene groups are readily modified into organelle-targetable probes, e.g., **DC-SPC-PPh3** and **DC-DPC-PPh3**, via Click chemistry. While **DC-SPC-PPh3** exhibits specificity to localize in mitochondria, **DC-DPC-PPh3** exhibits specificity to localize in lysosomes. Noticeably, regardless of pH rise within lysosomes under drug stimulation, **DC-DPC-PPh3** exhibits stable fluorescence, and it also displays low cytotoxicity. These features distinguished from the commonly used lysosomal probes that show alkalinity are quite important to qualify a lysosomes tracker, especially for the imaging of living cells for a long time or under external stimulations. Because its long-wavelength emission at ~650 and ~740 nm can efficiently avoid the spectral crosstalk with other probes emitting in the visible light region, **DC-SPC-PPh3** and **DC-DPC-PPh3** will act as standard colocalizing agents to estimate the other probes' local distribution in both 1PFM and

2PFM imaging. We expect that they will become valuable tools for fluorescent imaging and sensing in cell biology.

## 2.5 Experimental Section

### *2.5.1 Materials*

Carbazole aldehydes, 3-nitrine propyl triphenylphosphonium, and **DC-BDP** are synthesized according to standard procedures.[8-12] Toluene is dried over suitable reagents and distilled under argon immediately prior to use. The commercial dyes Cy5, NR, Rh-123, and TMRM are used as received with a purity >99% (checked by spectroscopic and chromatographic methods). Solvents for spectra studies are of spectroscopic grade and are used without purification.

### *2.5.2 General Methods*

The 400 ($^{1}$H) MHz NMR and 100 ($^{13}$C) MHz NMR spectra are registered at room temperature using perdeuterated solvents as internal standard. Melting points were obtained with a capillary melting point apparatus in open-ended capillaries and are uncorrected. Chromatographic purification is conducted with silica gel. All solvent mixtures are given as volume/volume ratios. The slit width is 3 nm for both excitation and emission during fluorescence spectra recording. Relative quantum efficiencies of fluorescence of compounds are obtained by comparing the areas under the corrected emission spectrum of the test sample in diluted solvents with that of Rhodamine B ($\Phi_F \approx 0.69$) in methanol, Cresyl violet ($\Phi_F \approx 0.54$) in methanol, and a reported aza-BODIPY derivative in toluene, which has a quantum efficiency of 0.42 according to the literature.[13] Nondegassed, spectroscopic grade toluene and a 10 mm quartz

cuvette are used. Dilute solutions (0.01 < A < 0.05) are used to minimize reabsorption effects. Quantum yields are determined using Equation 1:

$$\Phi_F^{(\text{sample})} = \Phi^{(\text{standard})} \times \left(\text{Abs}^{(\text{standard})} \times F^{(\text{sample})}\right) \Big/ \left(\text{Abs}^{(\text{sample})} \times F^{(\text{standard})}\right) \quad (1)$$

where $\Phi^{(\text{standard})}$ is the reported quantum yield of the standard, Abs is the absorbance at the excitation wavelength, and *F* is the integrated emission spectra.

Fluorescence lifetimes were determined for dilute solutions (ca. $10^{-6}$ M). Excitation anisotropy spectrum of **DC-DPC-PPh3** was recorded with a PTI Quantamaster spectrofluorimeter equipped with a photomultiplier tube (PMT) in high viscosity solvent (glycerol).

*2.5.3 Effects on Cell Growth/Viability*

MCF-7 (human breast carcinoma) cells are obtained from the Institute of Basic Medical Sciences (IBMS) of the Chinese Academy of Medical Sciences (CAMS). The cells are maintained under standard culture conditions (atmosphere of 5% $CO_2$ and 95% air at 37 °C) in RPMI-1640 medium, supplemented with 10% FBS (fetal calf serum). The cytotoxic effect of **DC-SPC-PPh3** and **DC-DPC-PPh3** against MCF-7 cells is assessed using the MTT assay. Briefly, MCF-7 cells in the exponential phase of growth are used in the experimentation. $1.5\times10^3$ cells/well are seeded onto 96-well plates and allowed to grow for 24 h prior to treatment with **DC-SPC-PPh3** or **DC-DPC-PPh3**. The incubation time of **DC-SPC-PPh3** or **DC-DPC-PPh3** is 1−2 h. At the end of this time, the **DC-SPC-PPh3** or **DC-DPC-PPh3** containing medium is replaced with PBS, MTT is then added to each well (final concentration 0.5 mg/mL) for 4 h at 37 °C, and formazan crystals formed through MTT metabolism by viable cells are dissolved in

DMSO. Optical densities are measured at 570 nm. $IC_{50}$ values (concentrations reducing the cell survival fraction by 50%) are obtained by nonlinear regression analysis, using Origin 8.5.

For MTS assay, HCT 116 cells (purchased from America Type Culture Collection, Manassas, VA) are cultured in RPMI-1640, supplemented with 10% FBS, and 1% penicillin, 1% streptomycin, at 37 °C, in a 95% humidified atmosphere containing 5% $CO_2$. N° 1 round 12 mm coverslips are treated with poly-D-lysine, to improve cell adhesion, and washed (3×) with PBS buffer solution. HCT 116 cells are prepared for cell viability studies in 96-well plates ($10\times10^3$ cells per well). The cells are incubated for an additional 22 h with **DC-DPC-PPh3** in different concentrations. The dye is dissolved in DMSO at a concentration of $3\times10^{-4}$ M and then, diluted with RPMI-1640 medium. Subsequently, 20 $\mu$L of MTS assay reagent is added into each well for 2 h at 37 °C and the relative viability is determined by measuring the MTS-formazan absorbance.

*2.5.4 Culture of MCF-7 Cells and Fluorescent Imaging*

MCF-7 cells are obtained from the Institute of Basic Medical Sciences (IBMS) of the Chinese Academy of Medical Sciences (CAMS). The cells are maintained under standard culture conditions (atmosphere of 5% $CO_2$ and 95% air at 37 °C) in RPMI-1640 medium, supplemented with 10% FBS (fetal calf serum). MCF-7 cells are grown in the exponential phase of growth on 35 mm glass-bottom culture dishes (Φ 20 mm) for 1−2 days to reach 70−90% confluence. These cells are used in colocalization experimentation. The cells are washed three times with RPMI-1640, and then are incubated with 2 mL medium containing **DC-SPC-PPh3** or **DC-DPC-PPh3** (37.5 nM) and Rh-123 or NR (25 nM) in an atmosphere of 5% $CO_2$ and 95% air at 37 °C. **DC-SPC-PPh3** or **DC-DPC-PPh3** are first prepared as a DMSO solution with a concentration of 1 mM and is diluted with RPMI-1640 for cell incubation. Cells are washed twice with 1 mL of

PBS at room temperature, and 1 mL of RPMI-1640 culture medium is added and then observed under a confocal microscope (Olympus FV1000).

For imaging of HCT 116 cells, the treated cover slips are placed in 24-well plates and 40000 cells per well are seeded and incubated for 48 h before incubation with the dye. From a stock solution (see above) of the dye, a 1 $\mu$M solution in culture media is freshly prepared and also a 100 nM solution of Lysotracker Red (Invitrogen). These solutions are used to incubate the cells. Cells are incubated for 4 h with the dye and 1 h with Lysotracker Red. After incubation, cells are washed with PBS three times, fixed with 3.7% formaldehyde in PBS at room temperature for 10 min, and incubated twice with $NaBH_4$ (1 mg/mL) in PBS at room temperature for 10 min. The cells are then washed with PBS twice and mounted on microscopy slides with Prolong Gold (Invitrogen) mounting media for imaging. One-photon fluorescence imaging is recorded on Leica TCS SP5 microscope system. The excitation wavelength for **DC-DPC-PPh3** is 633 nm, while emission is collected from 700 to 800 nm. For Lysotracker Red, 561 nm is used for exciting while collecting the emission between 570 and 670 nm. Two-photon fluorescence imaging is recorded on Leica TCS SP5 microscope system coupled to a tunable Coherent Chameleon Vision S laser (80 MHz, modelocked, 75 fs pulse width, tuned to 1000 nm). Two-photon induced fluorescence is collected with a water immersion 63× objective (HCX Pl APO CS 63.0×1.20 WATER UV).

### *2.5.5 Single-Molecule Experiments*

For the single-molecule experiments, thin-film samples are prepared by spin coating one drop of a dye-polymer-toluene cosolution ($10^{-10}$ M dye, poly[methyl methacrylate] (PMMA), 20 g $L^{-1}$) at 5000 rpm onto glass microscope coverslips. The resulting thickness of the polymer films

amounts to ~20 nm. The samples are excited with a solid-state laser (MRL-N-656.5, CNI) at 656.5 nm with an excitation intensity of 1.25 kW/cm$^2$. The output of the laser is directed into a home-built epifluorescence microscope and reflected via a dichroic beam splitter (FF660-Di, Semrock) toward an infinity-corrected oil-immersion objective (UPLSAPO, 100×, NA = 1.4, Olympus). In the plane of the sample, the excitation is defocused to an area of about 40×40 mm$^2$ by an additional lens with long focal distance ($f$ = 300 mm). The emission from the dyes is collected by the objective, passed through the dichroic beam splitter and two dielectric filters (HQ680LP, D680/30, Chroma), and is focused onto the chip of a back-illuminated electron-multiplying charge-coupled device (EMCCD, iXon DV897, Andor Technology). Typically, a fluorescence-microscopy image displays about 30 spatially isolated single molecules within the illuminated area. From this area, 5000 fluorescence-microscopy images are registered successively with an exposure time of 50 ms. The total acquisition time is 250 s. All experiments are carried out at room temperature.

### *2.5.6 Photostability*

**SPC**, **DC-SPC**, **DPC**, **DC-DPC**, and **Cy5** are dissolved in chloroform at a concentration of 10.0 $\mu$M, respectively. The solutions are irradiated under a 500 W iodine-tungsten lamp for 10 h at a distance of 250 mm away. An aqueous solution of sodium nitrite (50.0 g/L) is placed between the samples and the lamp as a light filter (to cut off the light shorter than 400 nm) and heat filter. The photostability is expressed in the terms of remaining fluorescence (%) calculated from the changes of fluorescence at the fluorescence maximum before and after irradiation by iodine-tungsten lamp.

### *2.5.7 2PA Cross-Section Measurements*

The investigations of the 2PA were performed with a femtosecond laser system (Coherent, Inc.). The output of a Ti:Sapphire laser (Mira 900-F, tuned to 800 nm, with a repetition rate = 76 MHz, average power ~1.1 W, and pulse duration ~200 fs), pumped by the second harmonic of cw $Nd^{3+}$:YAG laser (Verdi-10), was regeneratively amplified with a 1 kHz repetition rate (Legend Elite USP) providing ~100 fs pulses (FWHM) with energy ~3.6 mJ/pulse. This output at 800 nm was split into two separate beams with average power ~1.8 W each and pumped into two ultrafast optical parametric amplifiers (OPerA Solo (OPA), Coherent Inc.) with a tuning range 0.24−20 $\mu$m, ~100 fs (FWHM), and pulse energies up to ~100 $\mu$J. A single laser beam from the first OPA was used for direct 2PA cross-section measurements by the open-aperture Z-scan method.[60]

### *2.5.8 General Procedure for the Synthesis of BODIPY Derivatives*

**DC-BDP** (500 mg, 0.97 mmol) and carbazole aldehyde (0.97 mmol) were refluxed in a mixture of toluene (50 mL), acetic acid (1 mL), and piperidine (1 mL). Any water formed during the reaction was removed azeotropically by heating 8 h in a Dean-Stark apparatus. Crude product was then concentrated under vacuum, and purified by silica gel column chromatography.

2.5.8.1 SPC

**BDP** (1.11 mmol, 500 mg) and N-propargyl-4-carbazole aldehyde (1.11 mmol, 259 mg) were added to a 100 mL round bottomed flask containing 50 mL of toluene, and to this solution were added piperidine (1 mL) and acetic acid (1 mL). The mixture was heated under reflux by using a Dean-Stark trap, and the reaction was monitored by TLC 1:3 $CH_2Cl_2$:hexanes ($R_f$ 0.3).

When all of the starting material had been consumed, the mixture was cooled to room temperature, and solvent was evaporated. Water (300 mL) added to the residue and the product was extracted into the $CH_2Cl_2$ (3×200 mL). Organic phase was dried over $Mg_2SO_4$, evaporated, and residue was purified by silica gel column chromatography using 1:3 $CH_2Cl_2$:hexanes as the eluent, which yielded the desired product **SPC** as a purple powder (255 mg, 35%). mp 258−259 °C. $^1$H NMR (400 MHz, $CDCl_3$): δ 8.28 (s, 1H), 8.15 (d, *J* = 7.6 Hz, 1H), 7.85 (d, *J* = 8.0 Hz, 2H), 7.78 (d, *J* = 10.0 Hz 3H), 7.72 (d, *J* = 16.0 Hz, 1H), 7.45−7.52 (m, 4H), 7.31 (t, *J* = 8.0 Hz, 1H), 7.08 (d, *J* = 8.0 Hz, 2H), 6.67 (s, 1H), 6.01 (s, 1H), 5.05 (s, 2H), 2.63 (s, 3H), 2.29 (s, 1H), 1.49 (s, 3H), 1.44 (s, 3H). $^{13}$C NMR (100 MHz, $CDCl_3$): δ 155, 154, 141, 138, 135, 130, 128, 126, 124, 123, 121, 120, 109, 95, 73, 33, 30, 15. m/z (TOF MS ES): calcd $M^+$ for $C_{35}H_{27}BN_3F_2NaI$, 688.1209; found, 688.1222.

2.5.8.2 DC-SPC

**DC-BDP** (0.97 mmol, 500 mg) and N-propargyl-4-carbazole aldehyde (0.97 mmol, 225 mg) were added to a 100 mL round bottomed flask containing 50 mL of toluene, and to this solution were added piperidine (1 mL) and acetic acid (1 mL). The mixture was heated under reflux by using a Dean-Stark trap, and the reaction was monitored by TLC 1:3 $CH_2Cl_2$:hexanes ($R_f$ 0.4). When all of the starting material had been consumed, the mixture was cooled to room temperature, and solvent was evaporated. Water (300 mL) added to the residue and the product was extracted into the $CH_2Cl_2$ (3×200 mL). Organic phase was dried over $Mg_2SO_4$, evaporated, and residue was purified by silica gel column chromatography using 1:3 $CH_2Cl_2$:hexanes as the eluent, which yielded the desired product **DC-SPC** as a blue powder (220 mg, 35%). mp 263−264 °C. $^1$H NMR (400 MHz, $CDCl_3$): δ 8.31 (s, 1H), 8.27 (s, 1H), 8.16 (d, *J* = 8.0 Hz, 1H),

7.89 (d, *J* = 8.0 Hz, 2H), 7.85 (d, *J* = 8.0 Hz 1H), 7.75 (d, *J* = 16.0 Hz, 1H), 7.49−7.55 (m, 3H), 7.31 (t, *J* = 6.0 Hz, 1H), 7.06 (d, *J* = 8.0 Hz, 2H), 5.07 (s, 2H), 2.66 (s, 3H), 2.30 (s, 1H), 1.46 (s, 3H), 1.42 (s, 3H). $^{13}$C NMR (100 MHz, $CDCl_3$): δ 152.0, 148.6, 140.8, 140.3, 138.9, 138.7, 138.6, 136.6, 134.1, 130.5, 130.1, 129.8, 128.8, 126.4, 125.8, 123.9, 123.3, 120.8, 120.3, 115.2, 109.3, 109.1, 95.3, 72.7, 32.6, 12.6, 12.2. m/z (TOF MS ES): calcd $M^+$ for $C_{35}H_{25}BN_3F_2NaCl_2I$, 756.0429; found, 756.0435.

2.5.8.3 DPC

**BDP** (1.11 mmol, 500 mg) and N-propargyl-4-carbazole aldehyde (3.33 mmol, 777 mg) were added to a 100 mL round bottomed flask containing 50 mL of toluene, and to this solution were added piperidine (1.5 mL) and acetic acid (1.5 mL). The mixture was heated under reflux by using a Dean-Stark trap, and the reaction was monitored by TLC 1:2.5 $CH_2Cl_2$:hexanes ($R_f$ 0.3). When all of the starting material had been consumed, the mixture was cooled to room temperature, and solvent was evaporated. Water (300 mL) added to the residue and the product was extracted into the $CH_2Cl_2$ (3×200 mL). Organic phase was dried over $Mg_2SO_4$, evaporated, and the residue was purified by silica gel column chromatography using 1:2.5 $CH_2Cl_2$:hexanes as the eluent, which yielded the desired product **DPC** as a green powder (733 mg, 75%). mp 267−269 °C. $^1$H NMR (400 MHz, THF-$d_8$): δ 8.36 (s, 2H), 8.22 (d, *J* = 8.0 Hz, 2H), 7.93 (d, *J* = 8.0 Hz, 2H), 7.84 (d, *J* = 7.2 Hz 2H), 7.82 (s, 2H), 7.58−7.65 (m, 6H), 7.47 (t, *J* = 8.0 Hz, 2H), 7.26 (t, *J* = 8.0 Hz, 4H), 6.83 (s, 2H), 6.01 (s, 2H), 5.21 (s, 4H), 2.75 (s, 2H), 1.54 (s, 6H). $^{13}$C NMR (100 MHz, THF-$d_8$): δ 151.3, 138.8, 136.4, 129.1, 126.9, 124.1, 118.6, 118.0, 107.6, 107.3, 92.6, 76.1, 70.8, 29.9, 12.3. m/z (TOF MS ES): calcd $M^+$ for $C_{51}H_{36}BN_4F_2I$, 880.2046; found, 880.2010.

2.5.8.4 DC-DPC

**DC-BDP** (0.97 mmol, 500 mg) and N-propargyl-4-carbazole aldehyde (2.91 mmol, 678 mg) were added to a 100 mL round bottomed flask containing 50 mL of toluene, and to this solution were added piperidine (1.5 mL) and acetic acid (1.5 mL). The mixture was heated under reflux by using a Dean-Stark trap, and the reaction was monitored by TLC 1:2.5 $CH_2Cl_2$:hexanes ($R_f$ 0.35). When all of the starting material had been consumed, the mixture was cooled to room temperature, and solvent was evaporated. Water (300 mL) added to the residue and the product was extracted into the $CH_2Cl_2$ (3×200 mL). Organic phase was dried over $Mg_2SO_4$, evaporated, and residue was purified by silica gel column chromatography using 1:2.5 $CH_2Cl_2$:hexanes as the eluent, which yielded the desired product **DC-DPC** as a brown powder (728 mg, 80%). mp >300 °C. $^1$H NMR (400 MHz, $CDCl_3$): δ 8.32 (d, *J* = 16.0 Hz 1H), 8.18 (d, *J* = 8.0 Hz, 1H), 7.83−7.93 (m, 3H), 7.52−7.55 (m, 3H), 7.30 (t, *J* = 6.0 Hz 1H), 7.09 (d, *J* = 8.0 Hz 1H), 5.07 (s, 2H), 2.64 (s, 3H). $^{13}$C NMR: nd. m/z (TOF MS ES): calcd $[M+Na]^+$ for $C_{51}H_{34}BN_4F_2NaCl_2I$, 971.1164; found, 971.1168.

2.5.8.5 DC-SPC-PPh3

Under a nitrogen atmosphere, $CuSO_4 \cdot 5H_2O$ (2.8 mg, 0.012 mmol) in $H_2O$ (1 mL) and Na-ascorbate (4.2 mg, 0.022 mmol) in $H_2O$ (1 mL) followed by DIPEA (30 mL, 0.174 mmol) were added to a solution of (3-azidopropyl)triphenylphosphonium bromide (45 mg, 0.106 mmol) in EtOH (8 mL). A solution of **DC-SPC** (63 mg, 0.086 mmol) in toluene (20 mL) then was slowly added dropwise to the mixture in the absence of light. The reaction mixture was stirred in the dark for 12 h at room temperature. Still in the absence of light, the solvent was evaporated off

under vacuum, and the product was purified by silica gel column chromatography using 1:35 EtOH:$CH_2Cl_2$ as the eluent, which yielded the desired product **DC-SPC-PPh3** as a dark blue solid (84.7 mg, 85%). mp 235−236 °C. $^1$H NMR (400 MHz, $CDCl_3$): δ 8.62 (s, 1H), 8.25−8.13 (m, 3H), 7.89−7.50 (m, 20H), 7.26 (s, 2H), 5.73 (s, 2H), 4.47 (s, 2H), 3.56 (s, 2H), 2.57 (s, 3H), 2.04 (s, 2H), 1.42 (s, 3H), 1.36 (s, 3H). $^{13}$C NMR (100 MHz, $CDCl_3$): δ 151.6, 147.7, 143.4, 141.4, 140.9, 140.4, 138.8, 134.0, 133.9, 133.3, 130.8, 130.7, 127.9, 126.9, 124.8, 124.0, 123.5, 122.7, 121.8, 121.2, 120.4, 118.9, 118.0, 111.2, 97.1, 49.7, 49.3, 23.5, 18.9, 18.4, 12.8, 12.3. $^{31}$P NMR (100 MHz, DMSO) δ 24. m/z (TOF MS ES): calcd $[M\text{-}Br]^+$ for $C_{56}H_{46}BN_6F_2PCl_2I$, 1079.2005; found, 1079.2042.

# CHAPTER 3. NEAR-INFRARED FLUORESCENT 4,4-DIFLUORO-4-BORA-3A,4A-DIAZA-S-INDACENE PROBES FOR ONE-PHOTON AND TWO-PHOTON FLUORESCENCE BIOIMAGING

## 3.1 Abstract

A series of two-photon absorbing near-infrared (NIR) emitting 4,4-difluoro-4-bora-3a,4a-diaza-s-indacene (BODIPY) derivatives, **DDC** and **SDC**, were designed as fluorescent probes for one-photon fluorescence microscopy (1PFM) and two-photon fluorescence microscopy (2PFM) imaging. Linear and nonlinear photophysical properties, including UV-visible absorption, fluorescence, excitation anisotropy, photostability, and two-photon absorption (2PA) cross sections, of the dyes were investigated to assess the potential of using the new probes as bioimaging agents. Cell viability and colocalization studies of **DDC** with Lysotracker Red, a commercial lysosomal marker, in COS 7 and HCT 116 cells demonstrated not only low toxicity but also selective targeting of lysosomes. With an eye towards applications, **SDC** was encapsulated in silica-based nanoparticles for *in vitro* and *ex vivo* 1PFM and 2PFM bioimaging. The surface of the nanoparticles was modified with an RGD (arginine-glycine-aspartic acid) peptide, a well-known $\alpha_V\beta_3$ integrin-binding ligand. The nanoprobe exhibited good biocompatibility and highly selective RGD-mediated uptake in $\alpha_V\beta_3$ integrin-overexpressing cancers, while maintaining efficient fluorescence quantum yield and high photostability.

## 3.2 Introduction

Fluorescence microscopy techniques provide unique advantages, such as high spatial resolution and superior sensitivity, and have become essential tools for live cell imaging.[61, 62] Fluorescence techniques have enabled visualization of biological and biochemical mechanisms at

the subcellular level. With the current progress in ultrafast laser sources, two-photon fluorescence microscopy (2PFM), which affords deeper tissue penetration and excellent three-dimensional (3D) imaging capability, has been widely employed in bioimaging applications.[63, 64] One of the major challenges for 2PFM is a shortage of biocompatible probes with high two-photon absorptivity and high fluorescence quantum yields ($\Phi_{FL}$), in contrast to more commonly reported hydrophobic organic molecules that possess large two-photon absorption (2PA) cross-sections ($\delta_{2PA}$) that are synthetically more accessible.[65, 66]

Recently, nanomaterials encapsulating hydrophobic dyes have been reported as promising biocompatible nanocarriers for applications in bioimaging and biomedical fields.[67-69] Among a wide variety of nanoparticles, silica nanoparticles (SiNPs) doped with two-photon fluorescent (2PF) dyes have drawn particular attention in recent years. They provide stable aqueous dispersion and high photostability as well as appropriate size for *in vivo* imaging relative to organic dyes.[70-74] To achieve the potential of SiNPs in 2PFM, two-photon absorbing dyes are required to maintain high fluorescence while entrapped in the silica nanoparticles.

In combination with two-photon excitation, emission in the near-infrared (NIR) range (700−1000 nm), referred to as the optical window of biological samples, is also an important factor in biophotonics research.[75-77] Near IR fluorescent probes have the advantage of minimum light scattering and autofluorescence, all leading to high-contrast imaging.[23, 78] Currently, however, many commercially available fluorescent probes, such as Lysotrackers that selectively stain lysosomes, have fluorescence in the visible range, limiting their use in biological research.

As one of the promising NIR-emitting 2PA fluorophores, 4,4-difluoro-4-bora-3a,4a-diaza-s-indacene (BODIPY) derivatives have gained substantial attention. This is likely due to

their extraordinary photophysical properties, such as generally high fluorescence quantum yield, high photostability, and more importantly, strong absorbance and narrow emission bandwidth in the far-red to NIR region, providing improved fluorescence signal-to-background ratio for fluorescence microscopy.[39, 79-81] Herein, we introduce two 2PA NIR fluorescent BODIPY derivatives (**DDC** and **SDC**) along with their photophysical properties. Additionally, **DDC** was investigated for *in vitro* one-photon and two-photon fluorescence lysosomal imaging. Lysosomes are cellular organelles that play key roles in a wide variety of physiological activities, including cell antigen processing, bone remodeling, plasma membrane remodeling, and cell death.[82-84] Although lysosomal dysfunction is highly involved in diverse diseases, such as tumor invasion and neurodegenerative disorders,[85, 86] relatively few NIR fluorescent probes for lysosomal imaging have been reported.

To further investigate potential applications in tissues, SiNPs with narrow size distribution were prepared and employed to encapsulate a NIR fluorescent dye (**SDC**), a compound that has a maximum 2PA cross section of ~400 GM (1 GM (Göppert Mayer) = $10^{-50}$·$cm^4$·s·$photon^{-1}$). Stable aqueous dispersion and improved biocompatibility enabled successful deployment of **SDC**-doped SiNPs for bioimaging. In order to achieve selective tumor targeting, the surface of the SiNPs was modified with an RGD (arginine-glycine-aspartic acid) peptide to enable targeting of $\alpha_V\beta_3$ integrin.[87-90] It is well-known that $\alpha_V\beta_3$ integrin is responsible for cell growth and death.[91, 92] It is also noted that $\alpha_V\beta_3$ integrin is overexpressed in various types of tumor cells and tumor blood vessels,[93] and it regulates tumor growth, metastasis, and angiogenesis.[92, 94] In this study, we report not only the synthesis of RGD-modified **SDC**-encapsulated SiNPs, but the analysis of their photophysical characteristics. Moreover, selective

targeting with RGD-functionalized SiNPs was demonstrated by *in vitro* and *ex vivo* one-photon and two-photon fluorescence imaging. On the basis of 1PFM and 2PFM images, these nanoparticles were uptaken by cancer cells and tumor vasculatures that highly upregulate $\alpha_V\beta_3$ integrins, making these RGD-modified dye-containing SiNPs promising for tumor detection and angiogenesis imaging.

## 3.3 Results and Discussion

### *3.3.1 Linear and Nonlinear Photophysical Properties*

Linear and nonlinear photophysical properties (Table 3 and Table 4) of free **DDC** and **SDC** dyes, as well as RGD-modified **SDC**-encapsulated SiNPs (**RGD-SDC-SNP**) in water, were characterized to demonstrate their potential as efficient fluorescent probes. Lysotracker Red (LT Red), a commercial lysosomal marker, in DMSO was investigated for comparison purposes. **DDC** and **SDC** exhibited good solubility in investigated polar and nonpolar organic solvents. One-photon absorption (1PA) and fluorescence spectra of the free dyes (Figure 17) indicated modest dependence on solvent polarity. The relatively larger Stokes shift and lower fluorescence quantum yield in polar solvents were likely due to strong intermolecular interactions between solute and solvent.[95, 96] Furthermore, the absorption and emission spectra of **SDC**-doped SiNPs (**SDC-SNP**) in water were close to those of the free **SDC** dye in DMSO, suggesting a clear indication of successful loading of the dye in SiNPs (Figure 17).

**Table 3:** Linear Photophysical Properties for **DDC**, **SDC**, **RGD-SDC-SNP**, and LT Red.

| dye | solvent | $\lambda_{Abs}$ (nm) | $\lambda_{Em}$ (nm) | $\Delta\lambda$ (nm) | $\varepsilon^{max} \times 10^{-4}$ ($M^{-1}$ $cm^{-1}$) | $\Phi_{FL}$ |
|---|---|---|---|---|---|---|
| **DDC** | toluene | 679 ± 1 | 695 ± 1 | 16 ± 2 | 10 ± 1 | 0.90 ± 0.14 |
| | DCM | 674 ± 1 | 700 ± 1 | 26 ± 2 | 9.6 ± 1 | 0.78 ± 0.12 |
| | DMSO | 683 ± 1 | 711 ± 1 | 28 ± 2 | 9.5 ± 1 | 0.41 ± 0.06 |
| | ACN | 669 ± 1 | 697 ± 1 | 28 ± 2 | 9.3 ± 1 | 0.66 ± 0.10 |
| **SDC** | toluene | 592 ± 1 | 609 ± 1 | 17 ± 2 | 10 ± 1 | 0.79 ± 0.12 |
| | DCM | 587 ± 1 | 613 ± 1 | 26 ± 2 | 8.9 ± 1 | 0.82 ± 0.12 |
| | DMSO | 593 ± 1 | 630 ± 1 | 37 ± 2 | 9.2 ± 1 | 0.80 ± 0.12 |
| | ACN | 582 ± 1 | 616 ± 1 | 34 ± 2 | 8.9 ± 1 | 0.72 ± 0.11 |
| **RGD-SDC-SNP** | water | 594 ± 1 | 623 ± 1 | 29 ± 2 | 9.0 ± 1 | 0.56 ± 0.08 |
| **LT Red** | DMSO | 585 ± 1 | 604 ± 1 | 19 ± 2 | 7.8 ± 1 | 0.57 ± 0.09 |

Maxima of Absorption $\lambda_{Abs}$ and Fluorescence $\lambda_{Em}$, Stokes shift $\Delta\lambda$, Maximum molar absorptivity $\varepsilon^{max}$, and Fluorescence quantum yield $\Phi_{FL}$.

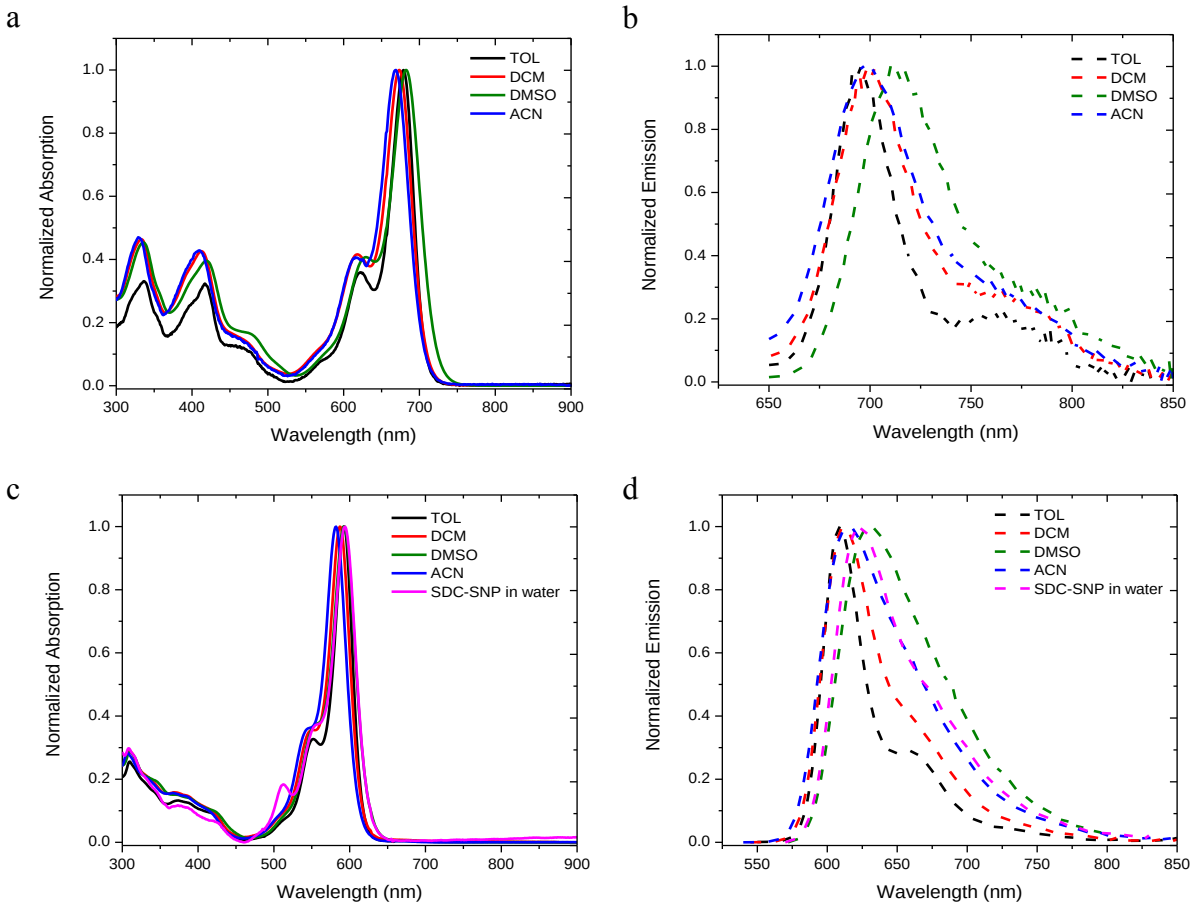


**Figure 17:** Normalized one-photon absorption (a, c) and fluorescence emission (b, d) spectra of **DDC** (top), **SDC** (bottom) in toluene (black), dichloromethane (red), dimethyl sulfoxide (green), acetonitrile (blue), and **SDC-SNP** (bottom) in water (pink).

The analysis of excitation anisotropy in viscous polytetrahydrofuran (pTHF) was performed since excitation anisotropy spectra provide information with respect to the spectral position of various electronic transitions.[23, 97] As shown in Figure 18, the values of anisotropy of free **DDC** and **SDC** dyes were not fully constant in the main long-wavelength absorption band which is associated with the low energy electronic transition $S_0 \rightarrow S_1$, although the values were nearly close to the theoretical limit ranging from -0.2 to 0.4.[98] This suggests that there are likely

more than one electronic transition in the main one-photon allowed absorption band. Decreases or shoulders in the short-wavelength region in the anisotropy spectra are indicative of higher electronic transitions $S_0 \rightarrow S_n$, generally two-photon allowed transitions.

Both compounds exhibited weak 2PA cross sections in the main long-wavelength absorption band, in good agreement with the anisotropy spectra, while the maximum 2PA cross sections were observed in the short-wavelength region. As described in Figure 18, higher 2PA cross sections of **DDC** correlated well with two minima in the excitation anisotropy spectrum, although the maximum 2PA value of **SDC** did not completely correspond to the shoulder in the anisotropy spectrum.

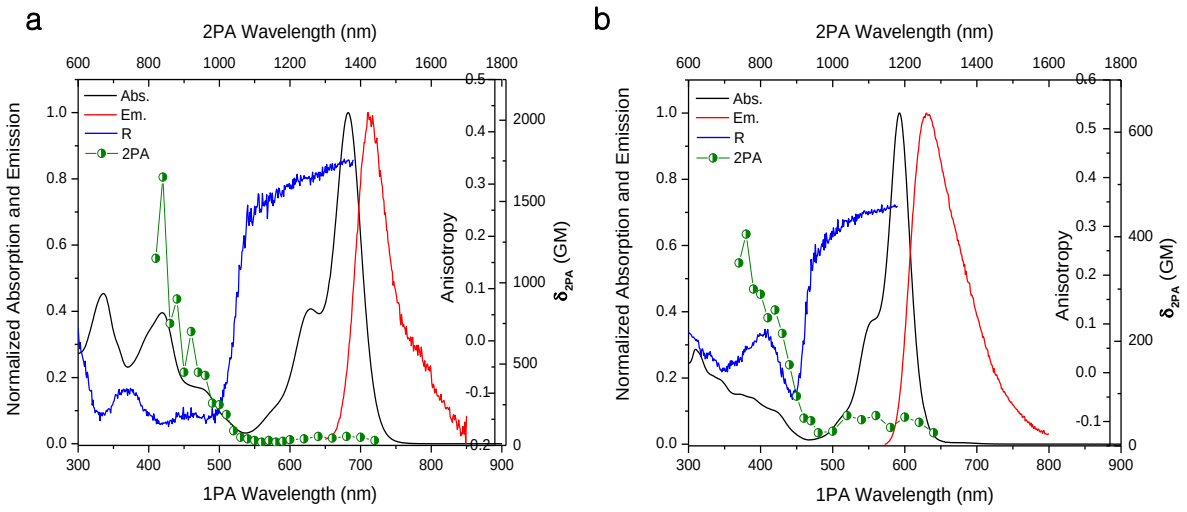


**Figure 18:** Linear and nonlinear optical spectra of (a) **DDC** in DMSO and (b) **SDC** in DMSO (1 GM (Göppert Mayer) = $10^{-50} \cdot cm^4 \cdot s \cdot photon^{-1}$). Linear absorption (black), emission (red), excitation anisotropy (blue) spectra, and 2PA cross sections (green circles).

To assess the potential applicability for fluorescence microscopy under prolonged irradiation, photochemical stability was investigated by an absorption method, and the corresponding photodecomposition quantum yield ($\eta$) was determined (Figure 19 and Table 4).[98-100] Details for photostability experiments are provided in the Experimental Section. In addition, as a means for evaluating the efficiency of a fluorescent marker, we previously defined a figure of merit ($F_M$), which is the product of the fluorescence quantum yield and the 2PA cross section normalized by photodecomposition quantum yield, i.e., $\Phi_{FL}\delta_{2PA}/\eta$.[99] The results listed in Table 4 indicate that $F_M$ values of both free **DDC** and **SDC** dyes in DMSO were three orders of magnitude higher than that of LT Red in DMSO, supporting strong potential of the dyes for fluorescence imaging.

**Table 4:** Photochemical Decomposition Quantum Yields and Figure of Merits of **DDC**, **SDC**, **RGD-SDC-SNP**, and LT Red.

| dye | solvent | $\Phi_{FL}$ | $\delta_{2PA}$ (GM) | $\eta \times 10^7$ | $\Phi_{FL}\delta_{2PA}$ (GM) | $F_M \times 10^{-6}$ (GM) |
|---|---|---|---|---|---|---|
| **DDC** | DMSO | 0.41 ± 0.06 | 1650 | 2.00 | 676.5 | 3382.5 |
| **SDC** | DMSO | 0.80 ± 0.12 | 405 | 1.36 | 324 | 2314.3 |
| **RGD-SDC-SNP** | water | 0.56 ± 0.08 | ND | 1.30 | ND | ND |
| **LT Red** | DMSO | 0.57 ± 0.09 | 33[a] | 54.4 | 18.81 | 3.46 |

Fluorescence quantum yield $\Phi_{FL}$, Maximum 2PA cross section $\delta_{2PA}$, Photodecomposition quantum yield $\eta$, Two-photon action cross section $\Phi_{FL}\delta_{2PA}$, and Figure of merit $F_M$. ND, not determined. [a]See reference 99.

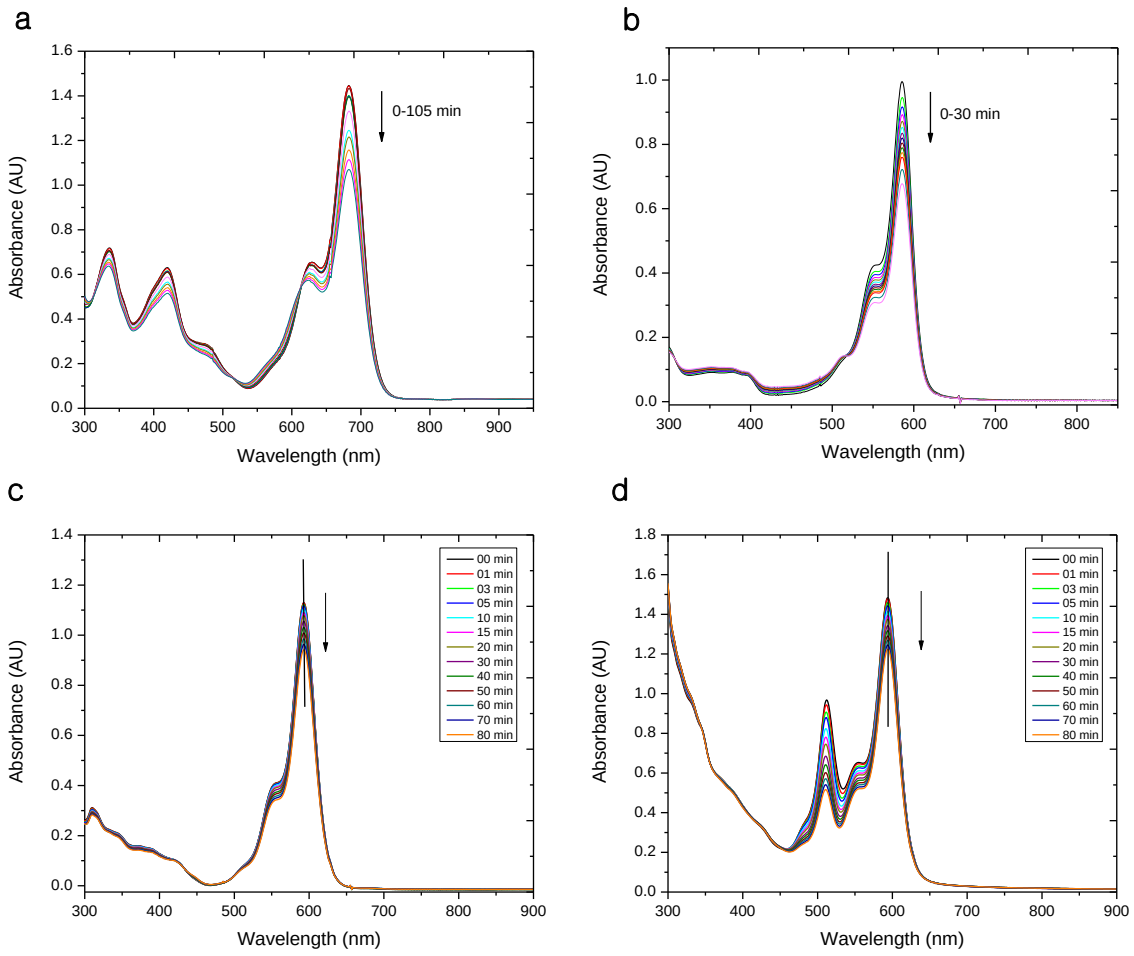


**Figure 19:** Time-dependent absorption spectra of (a) **DDC** in DMSO, and (b) LT Red in DMSO, (c) **SDC** in DMSO, and (d) **SDC-SNP** in water with corresponding wavelength irradiation.

### *3.3.2 Cytotoxicity and in Vitro One-photon and Two-photon Fluorescence Lysosomal Imaging*

In order to demonstrate the potential of **DDC** as a bioimaging probe, cytotoxicity assays were conducted in a fibroblast cell line, COS-7 and an epithelial colorectal carcinoma cell line, HCT 116 by MTS assay with dye concentration ranging from 1 to 50 $\mu$M. According to the data shown in Figure C-1 (Appendix C), **DDC** showed ~70% cell viability up to 25 $\mu$M in both cell

lines, confirming high cellular biocompatibility of the probe. Subsequently, cellular uptake of the dye into COS-7 and HCT 116 cells was determined by treating with different dye concentrations (5, 10, and 20 $\mu$M) and different incubation times (1, 2, and 4 h). Based on these results, 20 $\mu$M concentration for 2 h incubation was the condition utilized for one-photon fluorescence microscopy (1PFM) and 2PFM of COS 7 cells. A concentration of 10 $\mu$M was used for 4 h incubation with HCT 116 cells.

To further address selective subcellular localization properties of the probe in two different cell lines, a colocalization study was performed with LT Red. Both types of cells were incubated with **DDC** and LT Red, and subsequently, fluorescence images were obtained from two separated channels. The excitation wavelength for **DDC** was 633 nm while collecting the emission between 700 and 800 nm. For LT Red, 561 nm was used for excitation and emission was collected from 570 to 670 nm. The fluorescence from two different channels showed excellent spatial overlap (Figure 20, Figure C-2, and Figure C-4, Appendix C), and it was quantitatively determined by calculating Pearson's correlation coefficient with ImageJ software. The colocalization coefficients relative to LT Red were 0.96 and 0.88 in COS 7 and HCT 116 cells, respectively, supporting that **DDC** possesses highly selective lysosome-targeting ability.

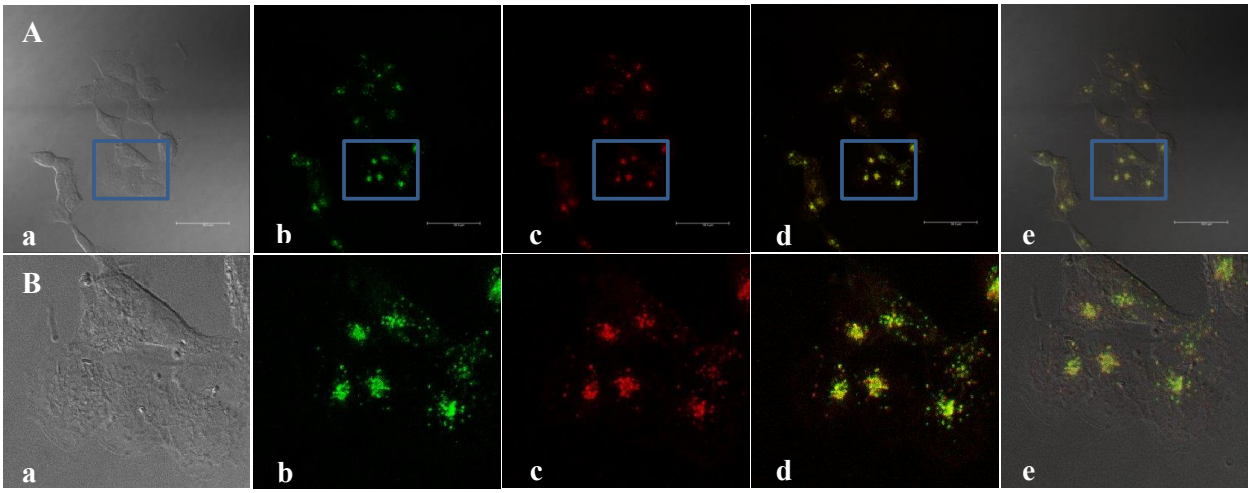


**Figure 20:** Colocalization images of HCT 116 cells coincubated with **DDC** (10 $\mu$M, 4 h) and LT Red (100 nM, 2 h). Row B shows magnification of area enclosed by the blue box in Row A. (a) differential interference contrast (DIC) image, (b) one-photon fluorescence image of **DDC**, (c) one-photon fluorescence image of LT Red, (d) overlaid image of b and c, (e) overlaid image of a, b, and c (Pearson's correlation coefficient 0.88). 50 $\mu$m scale bar

In order to explore the potential of **DDC**, 2PFM imaging was conducted for both COS 7 and HCT 116 cells (Figure 21 and Figure C-3, Appendix C). Excitation at 920 nm was employed due to the relatively strong 2PA cross section at this wavelength while the emission range was same as in 1PFM (700−800 nm). Consistent with high value of $F_M$, 2PFM images exhibited high resolution and contrast, as well as nearly identical localization with 1PFM images.

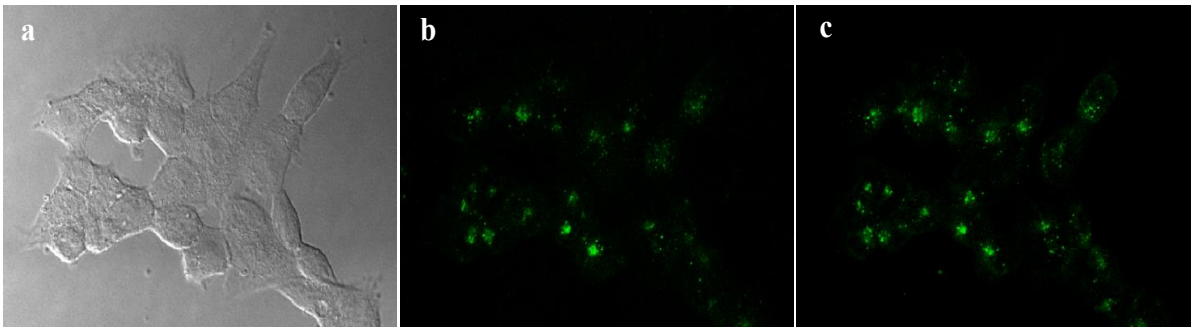


**Figure 21:** Images of HCT 116 cells incubated with **DDC** (10 $\mu$M, 4 h). (a) DIC image, (b) one-photon fluorescence image, and (c) two-photon fluorescence image.

### *3.3.3 Characterization of RGD-Modified SDC-Doped SiNPs*

The average size and size distribution of **SDC-SNP** and **RGD-SDC-SNP** were determined by dynamic light scattering (DLS). As presented in Figure C-5 (Appendix C), the average diameters of **SDC-SNP** and **RGD-SDC-SNP** were ca. 66 nm and 62 nm, respectively, which indicates that the RGD conjugation did not exert a significant effect on the size and distribution of the nanoparticles.

To examine surface charges of the dye-doped SiNPs, zeta potential measurements were conducted with **SDC-SNP** and **RGD-SDC-SNP**. Both nanoparticles exhibited moderate negative zeta potentials of -33 mV (**SDC-SNP**) and -26 mV (**RGD-SDC-SNP**), suggesting that the surface of nanoparticles dispersed in water was dominantly negatively charged. Furthermore, it is worth noting that the zeta potential slightly increased after surface modification of **SDC-SNP**s with the RGD peptide.

### *3.3.4 RGD Receptor-Targeted in Vitro and ex Vivo 1PFM and 2PFM Imaging with SiNPs*

To evaluate the selectivity of RGD-functionalized **SDC**-doped SiNPs, we used U87MG human glioma cells for cell imaging as these cells overexpress integrin receptors.[87-90] The cells directly incubated with **RGD-SDC-SNP** were used as a positive control, while the cells pre-incubated with free RGD and then incubated with the nanoparticle probe were employed as a negative (saturation) control. Cell images without **RGD-SDC-SNP** showed virtually no fluorescence (Figure 22(a) and (d)). Bright fluorescence was clearly observed in the nanoparticle-incubated cells (Figure 22(b) and (e)). In contrast, the cells with integrin receptors blocked by free RGD barely exhibited fluorescence (Figure 22(c) and (f)). These results demonstrated that the uptake of RGD-functionalized SiNPs by U87MG cells is mediated specifically by integrin receptors, and that receptor-mediated endocytosis can enhance the efficiency of the cellular uptake of the nanoprobe.

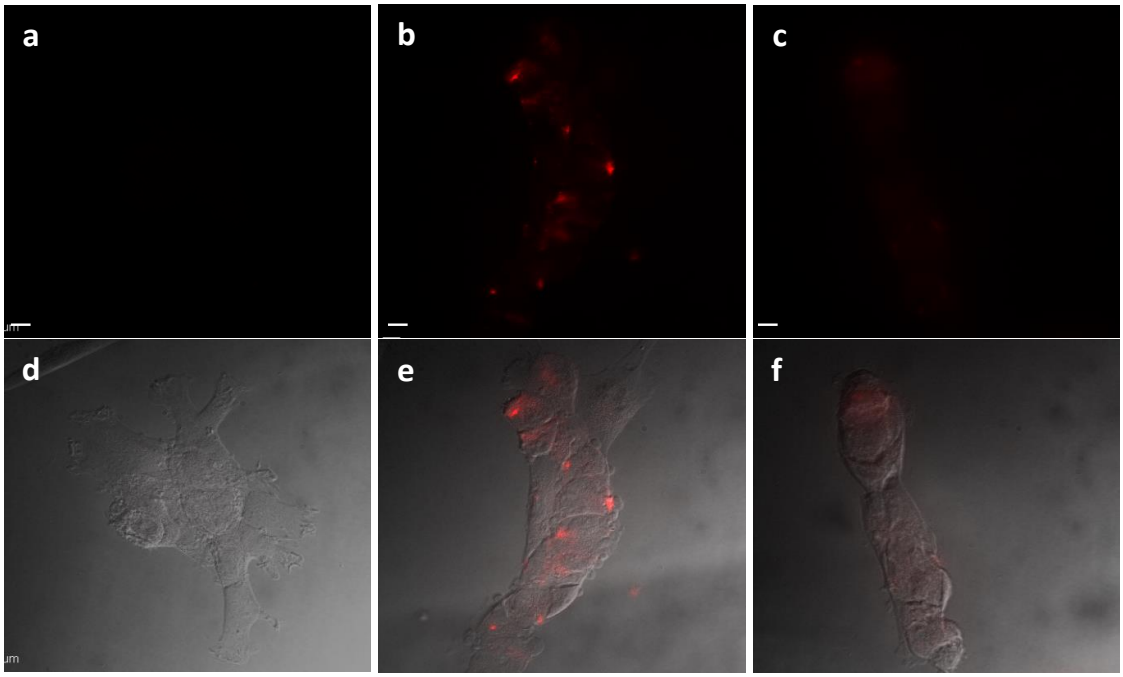


**Figure 22:** One-photon fluorescence (a-c) and DIC overlay (d-f) images in U87MG cells. Control group (a, d), **RGD-SDC-SNP** incubated group (b, e), and RGD-blocked group (c, f). 10 $\mu$m scale bar

To further assess the selectivity of **RGD-SDC-SNP** to integrin receptors in tissues, we stained histological sections of Lewis lung carcinoma (LLC) mouse tumors with the nanoprobe. The LLC tumor implants were used for this study as integrins are overexpressed in the vasculature of these tumors.[101] The two-photon fluorescence images demonstrated staining of LLC tumors with strong signal from vessel like structures (Figure 23), suggesting that the specific binding of RGD-functionalized SiNPs to integrins can be used to visualize tumor interior. Thus, the two-photon fluorescent nanoprobe is promising for in vivo imaging of tumors due to its large fluorescence quantum yield, near IR emission, and RGD-mediated specific tumor targeting.

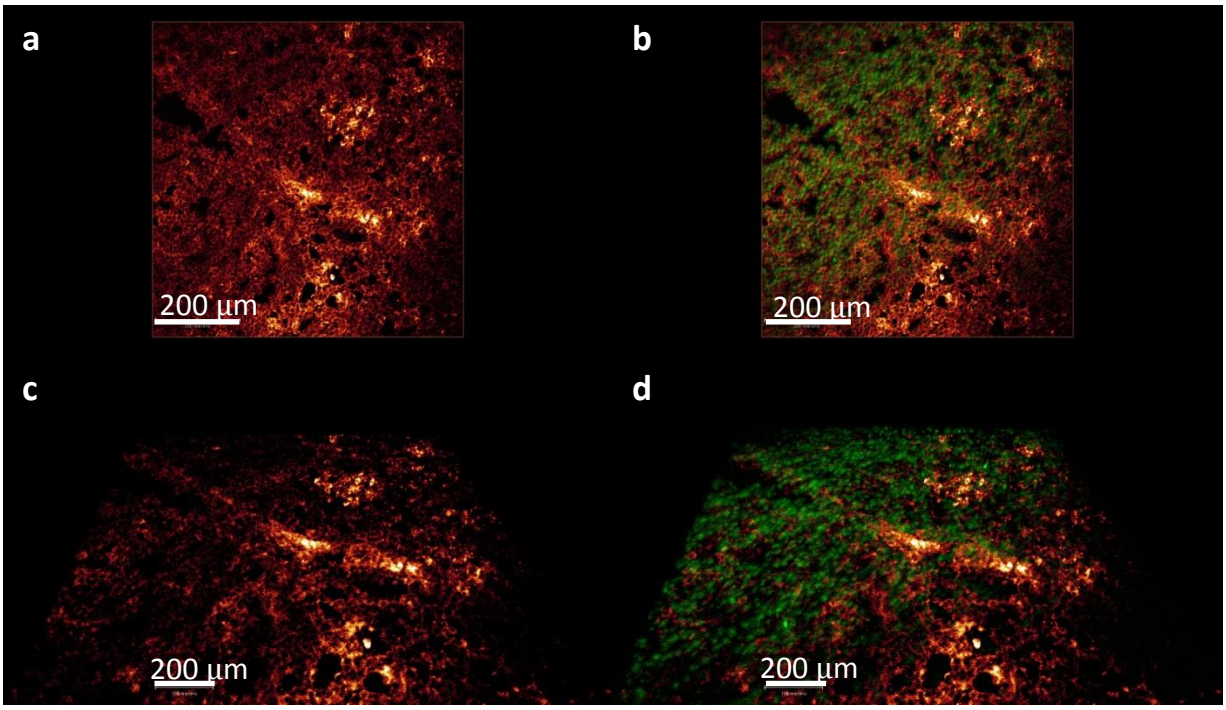


**Figure 23:** 2PFM images of tumor tissue co-stained with **RGD-SDC-SNP** (red) and Hoechst (green) in the view of X-Y plane (a, b) and 3D reconstruction (c, d).

### 3.4 Conclusion

In this study, we report novel two-photon absorbing NIR fluorescent BODIPY derivatives (**DDC** and **SDC**) for 1PFM and 2PFM bioimaging. The linear and nonlinear photophysical properties of the dyes were studied in organic solvents and compared to those of commercially available LT Red in DMSO. Both **DDC** and **SDC** dyes have extraordinary characteristics, such as good photostability and high 2PA cross sections, all leading to excellent $F_M$ values, over LT Red. 1PFM and 2PFM was conducted with COS 7 and HCT 116 cells in order to demonstrate the selectivity of **DDC** to lysosomes. **DDC** exhibited not only low cytotoxicity but also high lysosomal specificity in both cells. These results suggest that the new

**DDC** probe is promising for future lysosome-related studies. To address the potential of **SDC** for fluorescence tissue imaging, **SDC**-encapsulated SiNPs were synthesized and characterized. For specific delivery of the nanoprobe to the tumor, the surface of the SiNPs was modified with a cyclic RGD peptide. As determined by 1PFM and 2PFM, the uptake of RGD-functionalized dye-doped SiNPs by cells was RGD-dependent. Therefore, this nanoprobe possesses promising potential for *in vivo* fluorescence imaging of angiogenesis and RGD receptor-overexpressed cancers.

## 3.5 Experimental Section

### *3.5.1 Synthesis*

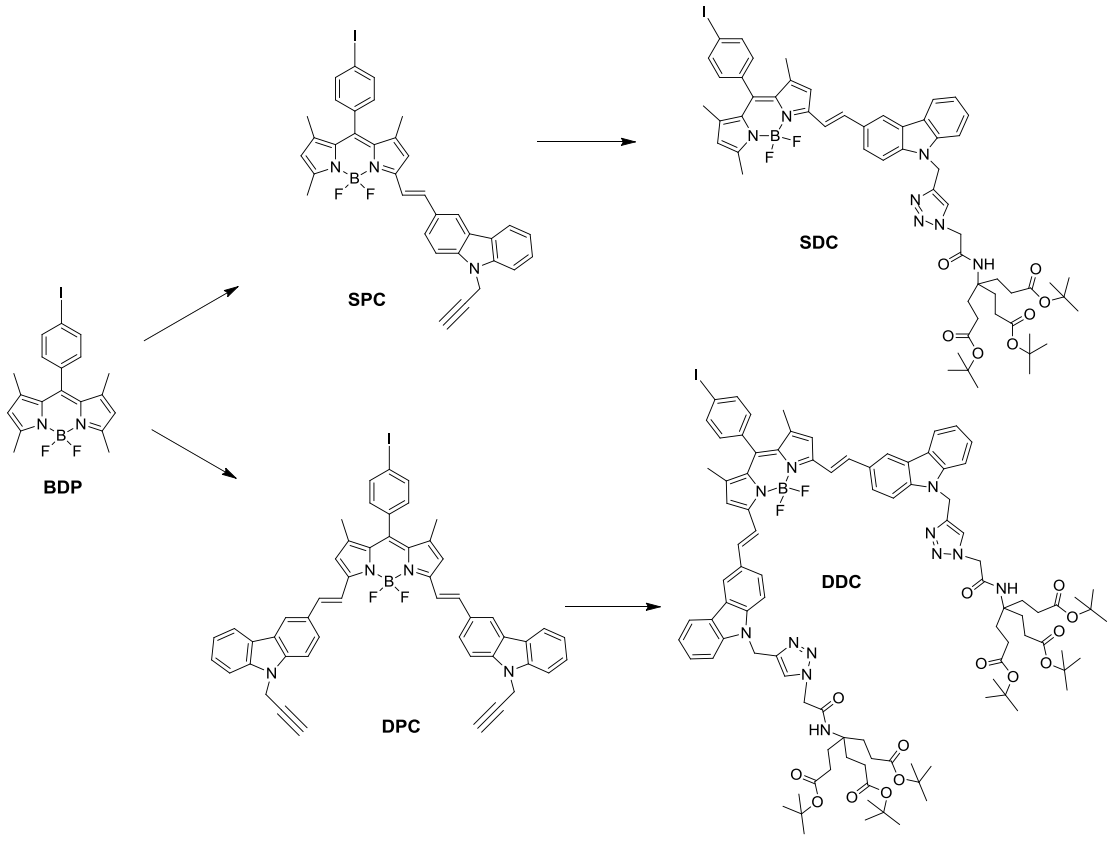


**Scheme 2:** Synthesis of **SDC** and **DDC**.

The intermediates **SPC** and **DPC** are our newly reported fluorophores and they were synthesized as reported previously.[102]

3.5.1.1 SDC

Under a nitrogen atmosphere, $CuSO_4 \cdot 5H_2O$ (2.8 mg, 0.012 mmol) in $H_2O$ (1 mL) and Na-ascorbate (4.2 mg, 0.022 mmol) in $H_2O$ (1 mL) followed by DIPEA (30 $\mu$L, 0.174 mmol) are added to a solution of Newkome dendrimer (52 mg, 0.106 mmol) in EtOH (8 mL). Then a solution of **SPC** (59 mg, 0.086 mmol) in toluene (20 mL) is slowly added dropwise to the mixture in the absence of light. The reaction mixture was stirred in the dark for 12 h at RT. Still in the absence of light, the solvent was evaporated off under vacuum and the product is purified

by silica gel column chromatography using 2:1 hexanes: ethyl acetate as the eluent yielded the desired product **SDC** as purple solid. (96 mg, 96%). m.p. 158−161 °C. $^{1}$H NMR (400 MHz, $CDCl_3$) δ 8.30 (s, 1H), 8.16 (d, 1H), 7.87 (d, 2H), 7.82−7.76 (m, 2H), 7.53−7.44 (m, 4H), 7.40−7.32 (m, 2H), 7.10 (d, 2H), 6.78 (s, 1H), 6.67 (s, 1H), 6.01 (s, 1H), 5.66 (s, 2H), 4.80 (s, 2H), 2.62 (s, 3H), 2.15 (t, 6H), 1.91 (t, 6H), 1.49 (s, 3H), 1.44 (s, 3H), 1.40 (s, 27H). $^{13}$C NMR (100 MHz, $CDCl_3$) δ 172.9, 172.8, 163.9, 163.3, 154.5, 154.2, 140.8, 140.5, 138.3, 130.3, 126.5, 126.3, 123.7, 123.1, 120.9, 120.8, 120.1, 109.5, 109.2, 94.1, 81.1, 81.0, 65.8, 58.2, 53.1, 39.0, 30.6, 29.9, 29.7, 28.1,19.2, 15.0, 13.8. m/z (TOF MS ES): Calcd $M^+$ for $C_{59}H_{69}BIF_2N_7O_7$: 1163.4364, found: 1163.4388

3.5.1.2 DDC

Under a nitrogen atmosphere, $CuSO_4 \cdot 5H_2O$ (5.6 mg, 0.024 mmol) in $H_2O$ (1 mL) and Na-ascorbate (8.4 mg, 0.044 mmol) in $H_2O$ (1 mL) followed by DIPEA (60 $\mu$L, 0.348 mmol) are added to a solution of Newkome dendrimer (104 mg, 0.212 mmol) in EtOH (8 mL). Then a solution of **DPC** (75 mg, 0.086 mmol) in toluene (20 mL) is slowly added dropwise to the mixture in the absence of light. The reaction mixture was stirred in the dark for 12 h at RT. Still in the absence of light, the solvent was evaporated off under vacuum and the product is purified by silica gel column chromatography using 1:1 hexanes: ethyl acetate as the eluent yielded the desired product **DDC** as green solid. (153 mg, 95%). m.p. 134−139 °C. $^{1}$H NMR (400 MHz, $CDCl_3$) δ 8.36 (s, 2H), 8.21 (d, 2H), 7.87 (d, 2H), 7.82−7.76 (m, 4H), 7.54−7.48 (m, 8H), 7.40 (s, 2H), 7.32 (t, 2H), 7.13 (d, 2H), 6.78 (s, 2H), 6.70 (s, 2H), 5.66 (s, 4H), 4.82 (s, 4H), 2.14 (t, 12H), 1.91 (t, 12H), 1.51 (s, 6H), 1.40 (s, 54H). $^{13}$C NMR (100 MHz, $CDCl_3$) δ 172.8, 163.9, 153.1, 144.4, 140.7, 140.6, 138.2, 130.7, 126.5, 126.4, 123.8, 123.4, 123.2, 120.9, 120.2, 120.0, 117.8,

116.8, 109.2, 100.0, 94.7, 81.0, 65.6, 58.2, 53.1, 39.0, 30.6, 29.9, 29.7, 28.1,19.2, 15.0, 13.8. m/z (TOF MS ES): Calcd $[M+H]^+$ for $C_{99}H_{120}BIF_2N_{12}O_{14}$: 1877.8153, found: 1877.8044.

### *3.5.2 Linear Optical Properties*

Linear absorption was determined with an Agilent 8453 UV-visible spectrophotometer. Fluorescence emission spectra were obtained by using a PTI Quantamaster spectrofluorimeter with a Hamamatsu R928 photomultiplier tube (PMT). Fluorescence emission spectra were corrected on the spectral sensitivity of the PMT. All measurements were performed using 10 mm spectrofluorometric quartz cuvettes in spectroscopic grade toluene (TOL), dichloromethatne (DCM), dimethyl sulfoxide (DMSO), acetonitrile (ACN), or ultrapure deionized water. Fluorescence quantum yields were determined in low concentration solutions ($C \leq 10^{-6}$ M) by a standard relative method with cresyl violet in methanol as a reference. The equation used is as follows;[98]

$$\Phi_{FL} = \Phi_R \frac{I}{I_R}\frac{OD_R}{OD}\frac{n^2}{n_R^2}\frac{RP_R}{RP} \quad (2)$$

where $\Phi_{FL}$ is the fluorescence quantum yield, the subscript R refers to the reference, *I* is the integrated emission signal, *OD* is the optical density at the excitation wavelength, *n* is the refractive index of the solvent, and *RP* is the relative power of the light source of the spectrofluorimeter at the excitation wavelength.

Excitation anisotropy spectra were obtained with two Glan-Thomson polarizers in the L-format configuration in viscous polytetrahydrofuran (pTHF). The value of anisotropy was determined by Equation 3;[98]

$$r = \frac{I_{VV} - GI_{VH}}{I_{VV} + 2GI_{VH}}, \left(G = \frac{I_{HV}}{I_{HH}}\right) \quad (3)$$

where *r* is the value of anisotropy, *G* is a factor which is the ratio of the sensitivities of the detection system for vertically and horizontally polarized light, the subscript *V* and *H* refer to vertically and horizontally polarized light, respectively.

### *3.5.3 Nonlinear Optical Properties*

Two-photon absorption (2PA) cross sections of **DDC** and **SDC** dyes in DMSO were measured by the open aperture Z-scan method using a femtosecond laser system (Coherent, Inc.).[103] The output of a Ti:sapphire laser (Mira 900-F, tuned to 800 nm, with a repetition rate 76 MHz, average power ~1.1 W and pulse duration ~200 fs), pumped by the second harmonic of $Nd^{3+}$:YAG laser (Verdi-10), was regeneratively amplified with a 1 kHz repetition rate (Legend Elite USP) providing ~100 fs pulses (FWHM) with energy ~3.6 mJ/pulse. This output at 800 nm was split into two separate beams and pumped two ultrafast optical parametric amplifiers (OPerA Solo (OPA), Coherent Inc.) with a tuning range 0.24−20 $\mu$m, ~100 fs (FWHM), and pulse energies up to ~100 $\mu$J. A single laser beam from the first OPA was used for the open aperture Z-scan method (Figure 24).[104] The 2PA measurements were performed in 1 mm spectrofluorometric quartz cuvettes with concentration of $10^{-3}$ M $\leq$ C $\leq$ $10^{-2}$ M at room temperature.

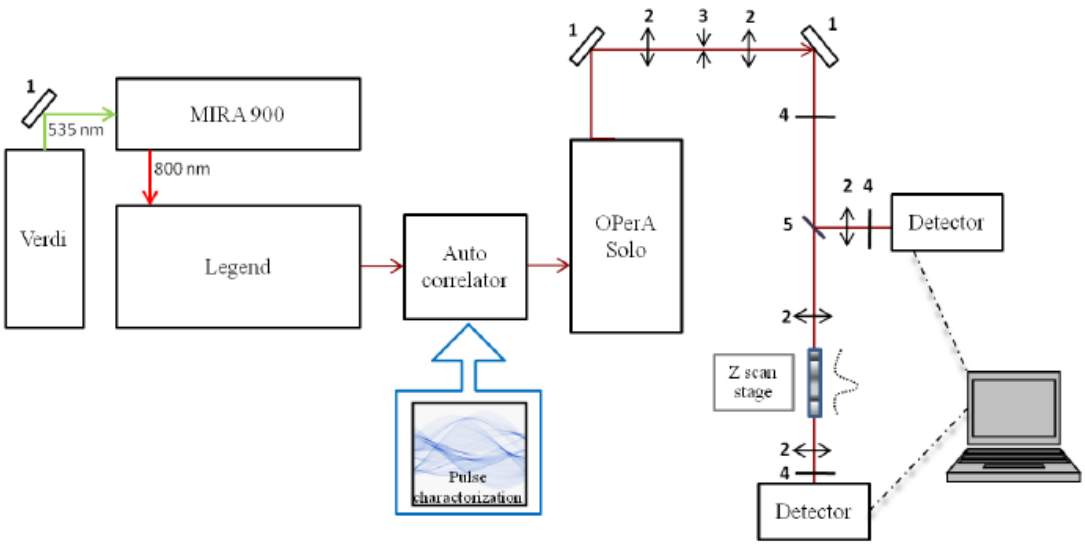


**Figure 24:** Z-scan experiment setup, (1) 100% reflection mirrors, (2) focusing lens, (3) pinhole, (4) neutral density filter, and (5) beam splitter.

### *3.5.4 Photostability*

Photochemical stability measurements of **DDC**, Lysotracker Red (LT Red, Invitrogen, Carlsbad, CA, USA), **SDC** in DMSO, and **SDC-SNP** in water were conducted by calculating photodecomposition quantum yield ($\eta$). **DDC** solution was irradiated with a 650 nm diode laser at 110 mW, whereas a 532 nm diode laser at 35 mW was employed for LT Red. The photostability of **SDC** and **SDC-SNP** were measured by irradiation of solutions using a 532 nm diode laser at 95 mW. The measurements were performed in 1 mm path length quartz cuvettes and photochemical decomposition quantum yields were determined as follows;[100]

$$\eta = \frac{(A_1 - A_0)N_A}{10^3 \times \varepsilon \times I \times (1 - 10^{(A_1 + A_0)/2})(t_1 - t_0)} \quad (4)$$

where $\eta$ is the photochemical decomposition quantum yield, $A_1$ is absorbance maximum at $t_1$, $A_0$ is absorbance maximum at $t_0$, $N_A$ is Avogadro's number, $\varepsilon$ is molar absorbance in $M^{-1} \cdot cm^{-1}$, ($t_1$-$t_0$) is time exposed (s), and $I$ is the intensity of laser in photon$\cdot cm^{-2} \cdot s^{-1}$.

### *3.5.5 Preparation and Characterization of Dye-encapsulating SiNPs*

Mercapto-terminated SiNPs with **SDC** were synthesized according to the method described by Prasad *et al.* with moderate modification.[105] Briefly, the nanoparticles were synthesized in the nonpolar core of Tween 80 micelles in deionized water. N-Methyl-2-pyrrolidone (NMP, Sigma-Aldrich) was used as a hydrophilic solvent which has unlimited water miscibility as well as suitable solubility for **SDC**. First, 0.2 g of the surfactant Tween 80 (Sigma-Aldrich) was dissolved in 2 mL deionized water with magnetic stirring, forming an oil-in-water microemulsion. Pre-polymerized silica solution was prepared by mixing 1.0 g of (3-Mercaptopropyl)trimethoxysilane (MPTS, Sigma-Aldrich) and 0.2 mL 30% Ammonium hydroxide with 10 mL NMP, stirring for 24 h. 0.3 mg of the dye was dissolved in 0.2 mL NMP, followed by addition of 0.02 mL of pre-polymerized MPTS solution. The mixture of dye-MPTS solution was then added into oil-in-water microemulsion dropwise with stirring. After stirring the reaction mixture for 24 h, the polymerized nanoparticles were purified by dialysis against deionized water in a 10 kDa cutoff cellulose membrane (Thermo Slide-A-Lyzer® 10K cut off dialysis cassettes, Fisher Inc.) for 48 h to remove surfactant and other unreacted molecules. The dialyzed solution was then filtered through a 0.22 $\mu$m cutoff membrane filter (Fisher Inc.) and stored at 4 °C for later use.

To functionalize SiNPs with RGD peptides, mercapto-terminated SiNPs were first reacted with 6-maleimidohexanoic acid N-hydroxysuccinimide ester (MAL-SCM, Sigma-Aldrich). Specifically, 0.5 mg MAL-SCM was dissolved in 0.1 mL NMP. This solution was then added into 1 mL mercapto-terminated SiNP solution with stirring. After stirring for 1 h, unreacted MAL-SCM was removed by dialysis against deionized water in a 10 kDa cutoff

cellulose membrane for 48 h. Subsequently, 0.5 mg RGD was dissolved in 0.1 mL of PBS (20×, pH 7.4) and added into MAL-terminated SiNP solution. After stirring for 1 h, the unreacted RGD was removed by dialyzing against deionized water in a 10 kDa cutoff cellulose membrane for 48 h. Finally, the dialyzed solution was filtered through a 0.22 $\mu$m cutoff membrane filter and stored at 4 °C for later use.

The particle size and zeta potential of **SDC-SNP** and **RGD-SDC-SNP** were measured with Zetasizer Nano-ZS90 (Malvern Instruments). The zeta potential was automatically calculated by determining electrophoretic velocity.

### *3.5.6 Cytotoxicity Assay*

COS 7 and HCT 116 cells (America Type Culture Collection, Manssas, VA, USA) were cultured in Dulbecco's modified Eagle's Medium (DMEM, Invitrogen, Carlsbad, CA, USA) and RPMI-1640 (Invitrogen, Carlsbad, CA, USA) media, respectively, supplemented with 10% fetal bovine serum (FBS, Atlanta Biologicals, Lawrenceville, GA, USA), and 1% penicillin-streptomycin (Atlanta Biologicals, Lawrenceville, GA, USA) at 37 °C in a 95% humidified atmosphere containing 5% $CO_2$. Both COS 7 and HCT 116 cells were prepared for cell viability studies in 96-well plates ($5\times10^3$ cells per well). The cells were incubated for an additional 22 h with **DDC** in various concentrations. The dye was first dissolved in DMSO at a concentration of ~$3\times10^{-4}$ M and then, diluted with the appropriate medium. Subsequently, 20 $\mu$L of CellTiter 96® Aqueous One Solution reagent (MTS assay) was added into each well, followed by further incubation for 2 h at 37 °C. The relative viability was determined by measuring the MTS-formazan absorbance on a microplate reader (Spectra Max M5, Molecular Devices, Sunnyvale,

CA, USA) at 490 nm with subtraction of the absorbance of the cell-free blank volume at 490 nm. The results from three individual experiments were averaged.

### *3.5.7 Uptake of DDC by Cancer Cells*

COS 7 and HCT 116 cells were placed onto poly-D-lysine-coated coverslips in 24-well plates ($4\times10^4$ cells per well), and the cells were incubated for 48 h before incubating with **DDC**. From a stock solution (see above) of the dye, 5, 10, or 20 $\mu$M solutions were freshly prepared with medium, while a 100 nM solution of LT Red was used for colocalization study. Cells were incubated for 1, 2, or 4 hours with the dye and 2 hours with LT Red. After incubation, the cells were washed with PBS three times, fixed with 3.7% formaldehyde in PBS at room temperature for 10 min, and treated twice with $NaBH_4$ (1mg/mL) in PBS at room temperature for 15 min each time. The cells were then washed with PBS twice and with water once. Finally, the cover slips were mounted on microscopy slides with ProLong® Gold (Invitrogen, Carlsbad, CA, USA) mounting reagent for imaging.

### *3.5.8 Uptake of SiNPs by Cancer Cells*

U87MG cells were seeded on poly-D-lysine-coated glass coverslips and incubated for 48 h. For RGD-blocked control group, 0.2 mg/mL RGD was added into cells 15 min in advance, and subsequently, free RGD was washed away with PBS. RGD-functionalized **SDC**-doped SiNPs were diluted into 5 $\mu$M and then added into cells. The cells were washed with PBS three times, fixed with 3.7% formaldehyde in PBS after 1 h incubation with **RGD-SDC-SNP**. The coverslips were mounted on microscopy slides with ProLong® Gold antifade reagent.

### *3.5.9 Ex Vivo Studies*

C57BL/6 mice were purchased from Harlan. $0.5\times10^6$ Lewis lung carcinoma (LLC) cells were injected into the flank. 14 days later, tumors were collected, fixed in 4% paraformaldehyde and embedded into Tissue-Tek® O.C.T™. Tumors were then sectioned at 10 $\mu$m thickness.

To stain tumor tissue, slides were first immersed in 100, 95, 70, and 50% ethanol (EtOH) in sequence, each for 10 min. Then, the slides were rinsed with deionized water and rehydrate with PBS buffer for 10 min. After rehydration, 1% bovine serum albumin (BSA) in PBS was added first on top of tissues for 10 min to block non-specific staining. **RGD-SDC-SNP** was then applied at 5 $\mu$M for 30 min and the slides were washed with PBS buffer three times. Finally, the slides were mounted with ProLong Gold® antifade reagent.

### *3.5.10 One-photon Fluorescence Microscopy (1PFM) and Two-photon Fluorescence Microscopy (2PFM) Lysosomal Imaging*

One-photon and two-photon fluorescence microscopy imaging with a 63× water immersion objective (Leica 506279) were recorded on a Leica TCS SP5 II confocal microscope system coupled to Coherent Chameleon Vision S Ti:sapphire laser with repetition rate ~80 MHz and ~70 fs (FWHM). Visible lasers in Leica TCS SP5 II system were employed for 1PFM, while the Coherent Chameleon system was used for 2PFM. The excitation wavelength for **DDC** was 633 nm while collecting the emission between 700 and 800 nm. For LT Red, 561 nm was used for the excitation wavelength and the emission was collected from 570 to 670 nm.

### *3.5.11 RGD Receptor-Targeted in Vitro and ex Vivo 1PFM and 2PFM Imaging with SiNPs*

One-photon fluorescence cell images were obtained using an Olympus IX70 DSU microscope coupled with a 100 W mercury lamp. Fluorescence was collected with a TexRed filter cube (Ex 562/40, DM 593, Em 654/40).

The fluorescence imaging of *ex vivo* tissue sections was performed with Leica SP5 II microscope. The nuclei of the sectioned tissues were stained with Hoechst. For 2PFM imaging, the nanoparticles were excited at 780 nm to avoid the excitation of Hoechst. Scanned images were then processed with Amira software for a 3D visualization.

# CHAPTER 4. *IN VITRO* PHOTODYNAMIC STUDIES OF NOVEL BODIPY DYE

## 4.1 Abstract

A new halogenated BODIPY dye was designed as photodynamic therapy (PDT) agent and its photophysical properties were characterized. The dye, having two iodine atom substitutents, exhibited low fluorescence quantum yield ($\Phi_{FL}$) of 0.02, providing high singlet oxygen generation quantum yield ($\Phi_{\Delta}$) of 0.93. Furthermore, *in vitro* photodynamic activities were evaluated to assess the potential of using the dye for PDT. Propidium iodide (PI) fluorescence assay and live cell imaging in LLC cells demonstrated that photosensitization of the agent can induce cellular damage, subsequently leading to cell death by necrosis.

## 4.2 Introduction

Photodynamic therapy (PDT) has emerged as a potential modality for the treatment of a variety of cancers. By combining PDT agents with light and oxygen, the light-activated photosensitizers transfer energy to surrounding oxygen molecules ($^3O_2$), resulting in the formation of reactive oxygen species (ROS), such as singlet oxygen ($^1O_2$). The generated ROS can induce cellular damage, leading to cell death by apoptotic and/or necrotic process.[4, 6, 7] As $^1O_2$ plays key roles in PDT therapeutic efficacy, it is essential that the optimized photosensitizers possess high efficiency of singlet oxygen generation (SOG) together with minimal dark toxicity and high photostability. In an effort to develop efficient PDT agents, heavy-atom effects have been considered as an effective approach to enhance intersystem crossing (ISC) in several chromophores.[5, 106]

The 4,4-difluoro-4-bora-3a,4a,-diaza-s-indacene (BODIPY) chromophore, since its first discovery,[107] has gained substantial attention. BODIPY dyes have extraordinary photophysical properties including generally high fluorescence quantum yields, excellent photostability, and high extinction coefficient (molar absorptivity).[39, 79, 108] Having readily tunable characteristics, these compounds have been widely studied for various applications such as fluorescent probes for one-photon and two-photon fluorescence bioimaging,[102, 109] sensors for various analytes,[110-112] and sensitizers for dye-sensitized solar cells (DSSC).[113, 114] Recently, there have been considerable research efforts in developing BODIPY dyes for PDT. By introducing heavy atoms, such as halogens, to the BODIPY core, BODIPY derivatives showed improved SOG, which renders them to be potential photosensitizers for PDT.[115-117] This is most likely due to the internal heavy-atom effect that enhances spin-orbit coupling and consequently, the efficiency of ISC from an excited singlet state ($S_1$) to an excited triplet state ($T_n$).[5]

In this study, we report not only the synthesis of a novel halogenated BODIPY dye (**BDP 3**), but the analysis of its photophysical properties including SOG. In order to demonstrate preliminary potential PDT efficacies of the agent, *in vitro* photodynamic activities were conducted.

### 4.3 Results and Discussion

The synthesis of **BDP 3** began with 4-hydroxybenzaldehyde, which was used to prepare compound **1** (4,4-difluoro-8-(4-hydroxyphenyl)-1,3,5,7-tetramethyl-4-bora-3a,4a-diaza-s-indacene), a BODIPY derivative (Scheme 3). According to a literature procedure,[118] **1** was prepared via a condensation reaction of 4-hydroxybenzaldehyde with 2,4-dimethylpyrrole in $CH_2Cl_2$ in the presence of a catalytic amount of trifluoroacetic acid at room temperature,

followed by an oxidation reaction with DDQ (2,3-dichloro-5,6-dicyano-1,4-benzoquinone) and a subsequent chelation reaction with $BF_3 \cdot OEt_2$ in the presence of triethylamine at room temperature. Then, it reacted with triethyleneglycol monotosylate in the presence of potassium carbonate to produce compound **2** in acetonitrile. Iodination of **2** with N-iodosuccinimide in the dark at room temperature afforded **BDP 3** (4,4-difluoro-8-(4-{2-[2-(2-hydroxyethoxy)ethoxy]ethoxy}phenyl)-1,3,5,7-tetramethyl-2,6-diiodo-4-bora-3a,4a-diaza-s-indacene) as a red solid.

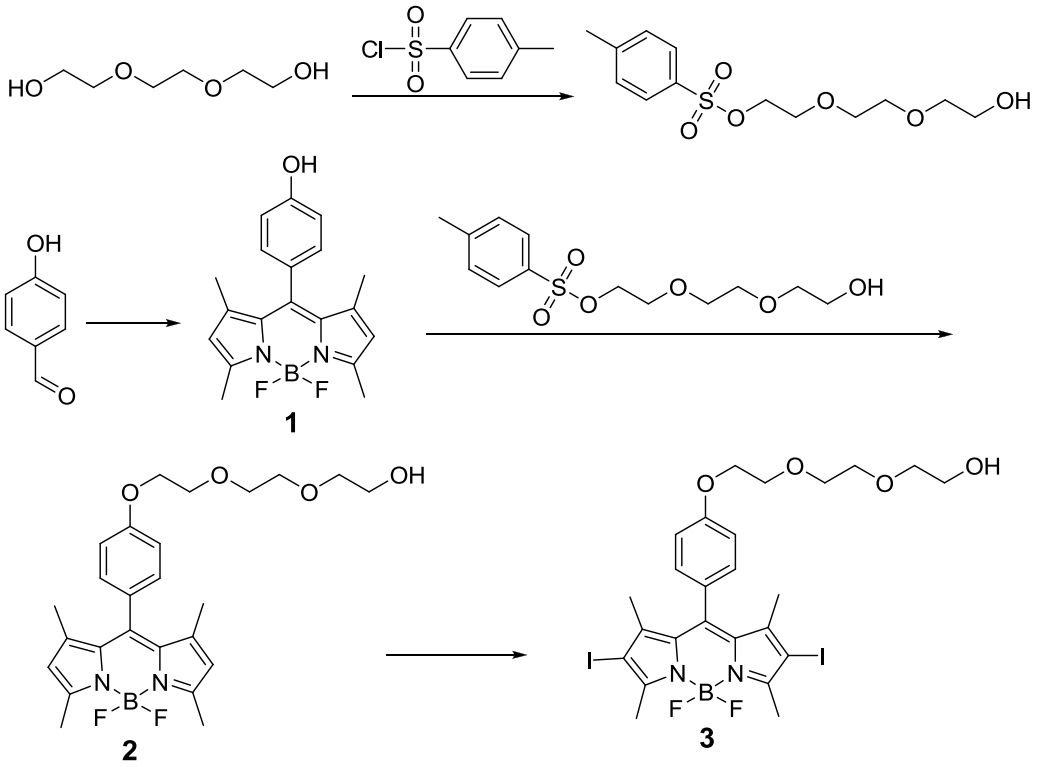


**Scheme 3:** Synthetic route for **BDP 3**.

The photophysical properties of **BDP 3** were characterized to assess the potential as an efficient PDT agent and are summarized in Table 5 along with those of Acridine, a commonly used photosensitizer for oxidative stress studies,[119, 120] for comparison purposes. As shown in Figure 25(A), **BDP 3** in acetonitrile (ACN) exhibited sharp steady-state absorption and fluorescence emission spectra with a fluorescence quantum yield ($\Phi_{FL}$) of 0.02. The low fluorescence quantum efficiency of the dye can be attributed to the introduction of two iodine atoms at the 2- and 6- positions, which enhances the ISC efficiency from an excited singlet state ($S_1$) to an excited triplet state ($T_n$). Additionally, the ability of the agent to generate $^1O_2$ was assessed by a direct measurement of near-infrared luminescence at 1270 nm. As presented in Figure 25(B), **BDP 3** exhibited characteristic luminescence of $^1O_2$ at 1270 nm with a singlet oxygen generation quantum yield ($\Phi_\Delta$) of 0.93, which is higher than that of Acridine. This result is a clear indication that **BDP 3** is potentially promising as a PDT agent.

**Table 5:** Photophysical Properties for **BDP 3** and Acridine

| **Dye** | **BDP 3** | **Acridine** |
|---|---|---|
| Solvent | ACN | ACN |
| $\lambda_{Abs}$ (nm) | 528 ± 1 | 356 ± 1 |
| $\lambda_{Em}$ (nm) | 546 ± 1 | 403 ± 1 |
| $\Delta\lambda$ (nm) | 18 ± 2 | 47 ± 2 |
| $\varepsilon^{max} \times 10^{-3}$ ($M^{-1}$ $cm^{-1}$) | 75.5 ± 8 | 9.3 ± 1 |
| $\Phi_{FL}$ | 0.02 ± 0.002 | ND |
| $\Phi_\Delta$ | 0.93 ± 0.09 | 0.82 ± 0.08 |

Maxima of Absorption $\lambda_{Abs}$ and Fluorescence $\lambda_{Em}$, Stokes shift $\Delta\lambda$, Maximum molar absorptivity $\varepsilon^{max}$, Fluorescence quantum yield $\Phi_{FL}$, and Singlet oxygen generation quantum yield $\Phi_\Delta$. ND, not determined.

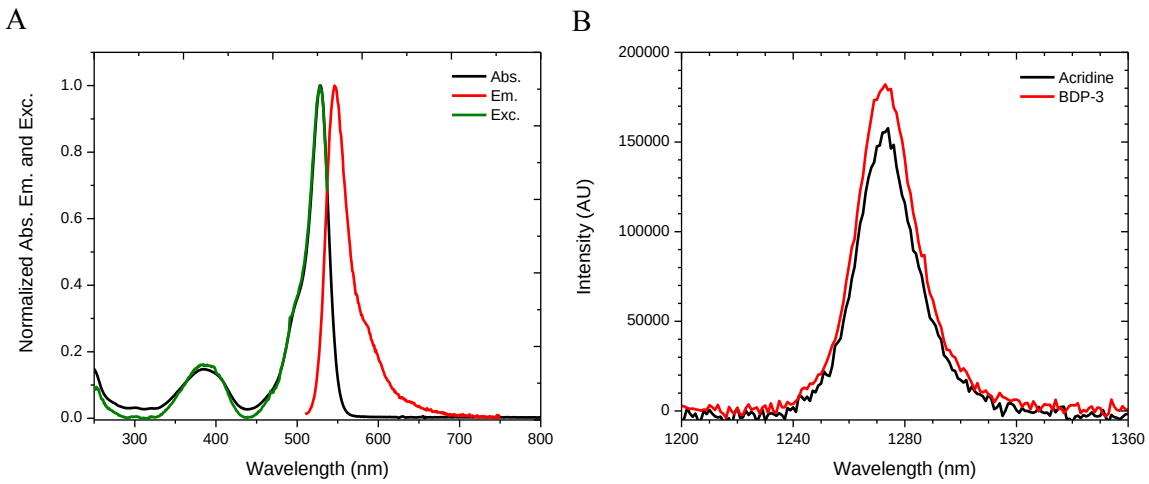


**Figure 25:** (A) Normalized absorption (black), emission (red), and excitation (green) spectra of **BDP 3** in ACN. (B) Near-infrared singlet oxygen luminescence spectra of **BDP 3** (red) and Acridine (black) in ACN.

*In vitro* photodynamic activities of **BDP 3** were evaluated against LLC cells, a Lewis lung carcinoma cell line. First, dark cytotoxicity with the dye concentration ranging from 1 to 20 $\mu$M and photoinduced cytotoxicity of the photosensitizer were assessed via an MTS assay. As shown in Figure 26(A), cell viability remained over 70% until 15 $\mu$M, providing good cellular biocompatibility of the agent. At the dye concentration of 10 $\mu$M with a light dose of 2.1 J/cm$^2$, ~50% of the cells appeared to be killed indicating highly efficient light-induced toxicity of the agent (Figure 26(B)).

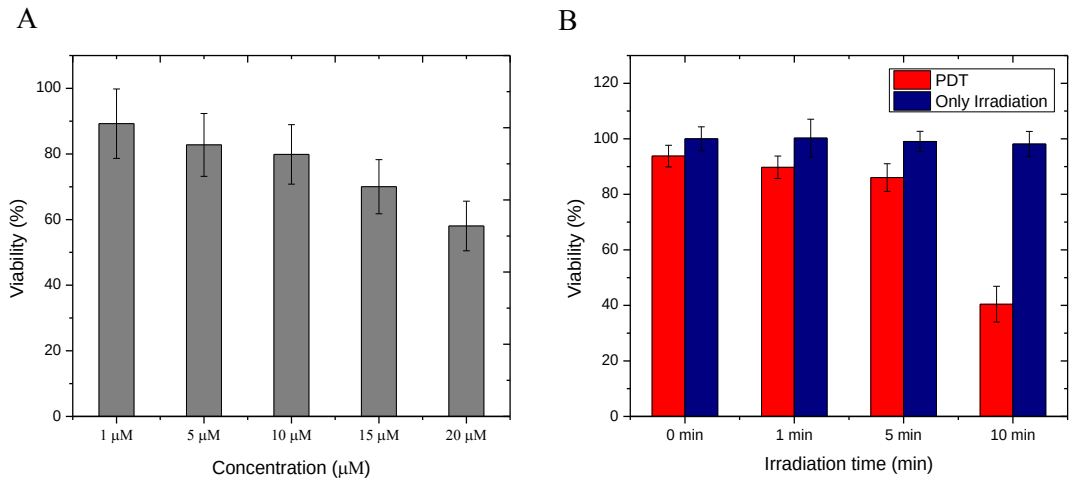


**Figure 26:** (A) Dark cytotoxicity toward LLC cells after incubation with increasing concentrations of **BDP 3**. (B) Cell viability of LLC cells in the absence (blue) or presence (red) of 10 $\mu$M of **BDP 3** under a different period of irradiation time in the spectral range 502-542 nm.

Furthermore, PDT-induced cell necrosis was demonstrated by a propidium iodide (PI) fluorescence assay. The PI, a membrane impermeant marker, can stain only dead cells and becomes fluorescent mainly due to the loss of membrane integrity.[121] Control cells without **BDP 3** exhibited healthy morphology and negative staining with PI (Figure 27(A) to (C)), suggesting irradiation alone in this wavelength range is nontoxic to the cells. In contrast, the cells treated with the combination of **BDP 3** and irradiation showed red fluorescence from PI (Figure 27(D) to (F)). These results suggest that photosensitization of the agent can induce cellular damage, subsequently leading to cell death by a necrotic mechanism.

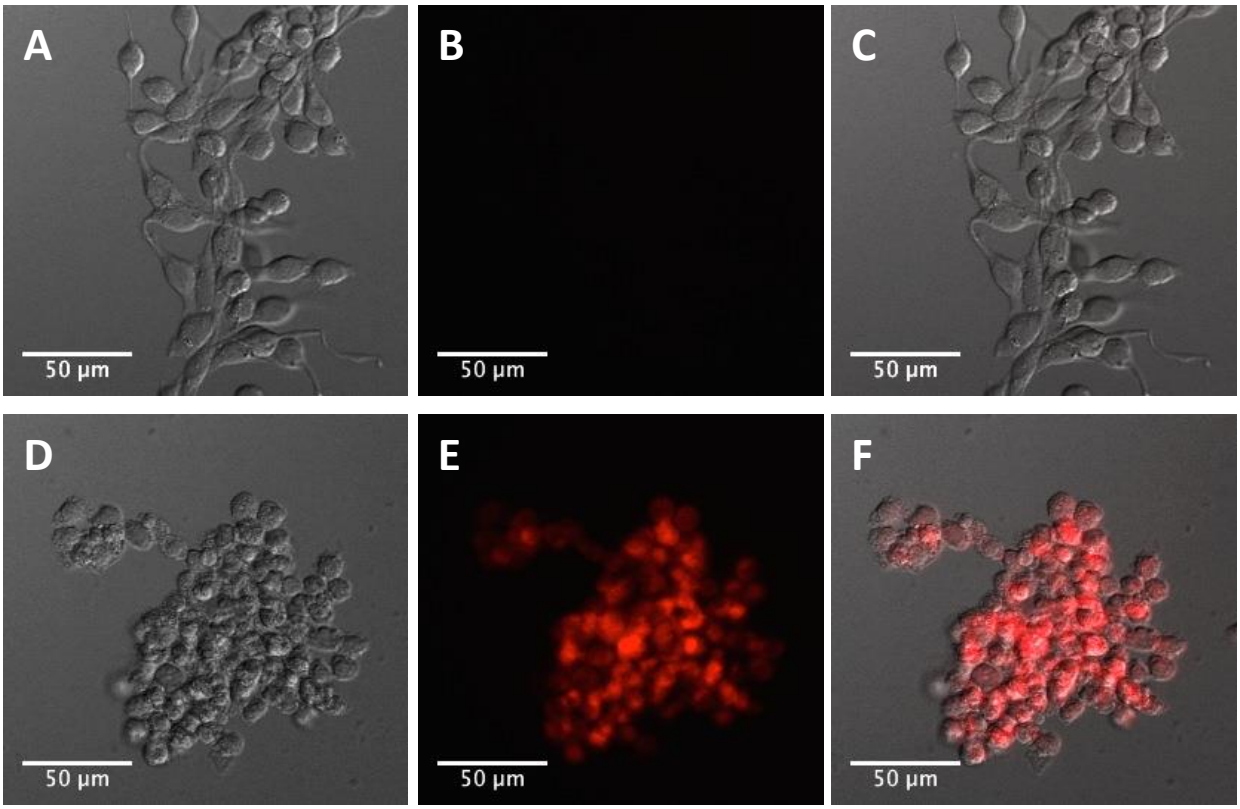


**Figure 27:** Differential interference contrast, DIC, (A, D) and confocal fluorescence (B, E) images of LLC cells stained with propidium iodide after irradiation in the absence (A−C) or presence (D−F) of **BDP 3**. Scale bars show 50 $\mu$m.

Finally, we examined time-lapsed live cell imaging to provide insight on cell morphological changes. Cells incubated with **BDP 3** showed cell swelling-like activities, a characteristic of necrosis, immediately after irradiation (Figure 28(C) and (D)). Eight minutes after irradiation, all the cells in the observation window appeared to undergo necrosis, supporting that cell death is not caused via an apoptotic mechanism. As shown in Figure 28(A) and (B), control cells without the dye exhibited no detectable cellular damage, even 30 min after irradiation, confirming nontoxicity of the light alone.

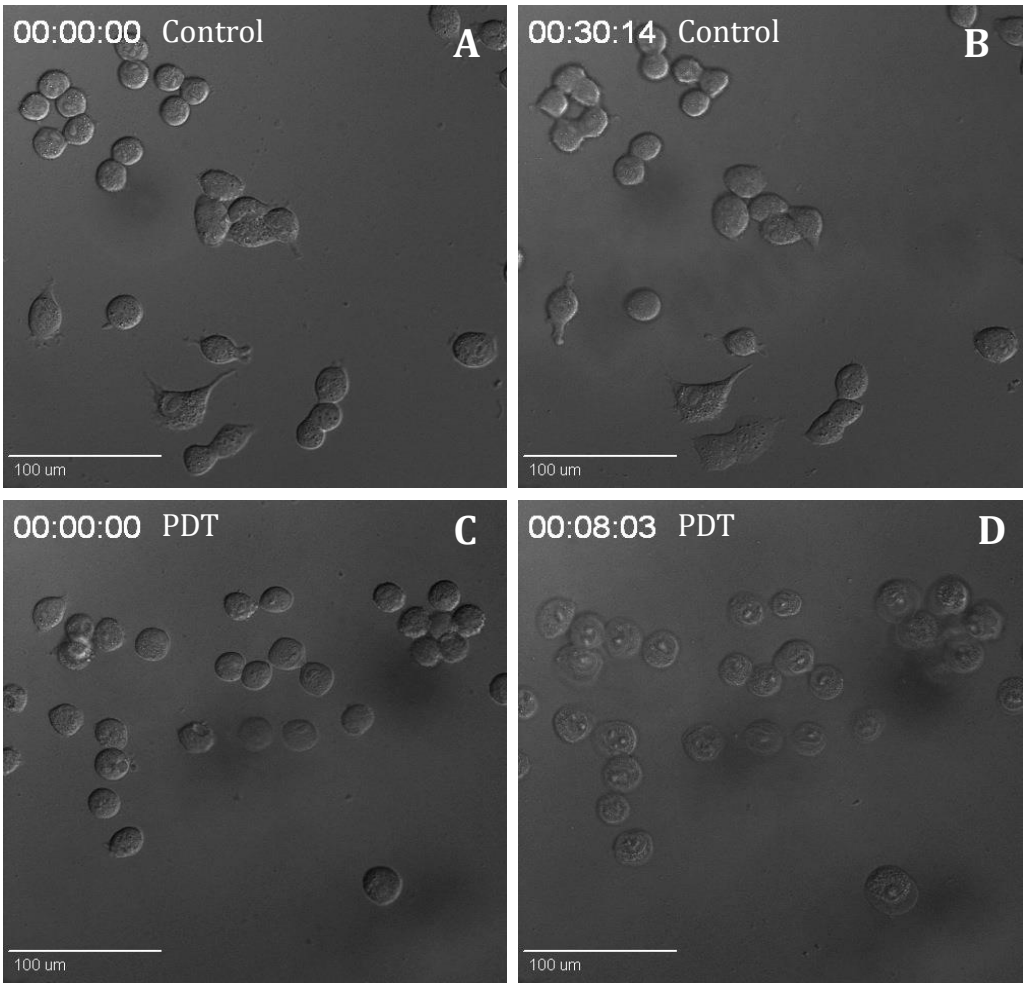


**Figure 28:** DIC images of LLC cells after irradiation in the absence (A, B) or presence (C, D) of **BDP 3**. Scale bars show 100 $\mu$m.

## 4.4 Conclusion

In conclusion, we developed a novel photosensitizer, **BDP 3**, and assessed its *in vitro* photodynamic activities. The photophysical properties, including $\Phi_{\Delta}$, were characterized and compared to those of Acridine, a commonly used photosensitizer. The introduction of heavy halogen atoms to the BODIPY core was designed to enhance the efficiency of ISC, and resulted

in higher $\Phi_\Delta$ for **BDP 3** than that of Acridine. Moreover, the dye exhibited significant PDT-induced cell necrosis along with minimal dark toxicity, strongly suggesting that **BDP 3** is a promising candidate as a PDT agent.

## 4.5 Experimental Section

### *4.5.1 Synthesis*

#### 4.5.1.1 General

All reagents and solvents were purchased from commercial suppliers and used without further purification. Triethyleneglycol monotosylate[122] and compound **1**[118] were prepared according to their respective literature reports. Flash column chromatography was performed on a CombiFlash® Rf+ automated flash chromatography using RediSep Rf Gold® normal-phase HP silica columns. $^1$H and $^{13}$C NMR spectra were carried out in $CDCl_3$ solution on a Bruker AVANCE spectrometer (400 MHz).

#### 4.5.1.2 Synthesis of 4,4-difluoro-8-(4-{2-[2-(2-hydroxyethoxy)ethoxy]ethoxy}phenyl)-1,3,5,7-tetramethyl-4-bora-3a,4a-diaza-s-indacene (2)

A mixture of **1** (3.40 g, 10 mmol), triethyleneglycol monotosylate (4.57 g, 15 mmol), and $K_2CO_3$ (2.76 g, 20 mmol) in 100 mL dry acetonitrile was heated to reflux for 20 h under argon atmosphere. After cooling to room temperature, the solvent was removed under reduced pressure. The residue was added 100 mL water and extracted with $CH_2Cl_2$ (100 mL×2). The organic layer was washed with brine (100 mL×2), dried over $MgSO_4$, and evaporated. The crude mixture was purified by flash column chromatography using 0.4% methanol/$CH_2Cl_2$, giving the desired compound **2** as a red liquid (3.81 g, 80.7%). $^1$H NMR (400 MHz, $CDCl_3$): δ (ppm) 7.16 (d, *J* =

8.6 Hz, 2H), 7.03 (d, *J* = 8.6 Hz, 2H), 5.97 (s, 2H), 4.21 – 4.17 (m, 2H), 3.93–3.89 (m, 2H), 3.78–3.72 (m, 6H), 3.66–3.62 (m, 2H), 2.55 (s, 6H), 2.33 (t, *J* = 6.1 Hz, 1H), 1.42 (s, 6H). $^{13}$C NMR (101 MHz, $CDCl_3$): δ (ppm) 159.43, 155.42, 143.30, 141.91, 131.97, 129.34, 127.47, 121.25, 115.32, 77.48, 77.16, 76.84, 72.58, 71.01, 70.54, 69.87, 67.57, 61.95, 14.73. HRMS (ESI, m/z): calcd for $C_{25}H_{31}BF_2N_2O_4$ ($[M+H]^+$) 473.2422; found 473.2436.

4.5.1.3 Synthesis of 4,4-difluoro-8-(4-{2-[2-(2-hydroxyethoxy)ethoxy]ethoxy}phenyl)-1,3,5,7-tetramethyl-2,6-diiodo-4-bora-3a,4a-diaza-s-indacene (3)

To a solution of **2** (3.78 g, 8.0 mmol) in 50 mL anhydrous $CH_2Cl_2$ was added N-iodosuccinimide (NIS) (3.69 g, 16.4 mmol), and the resulting mixture was stirred for 8 h in the dark at room temperature. Then the reaction mixture was diluted with 50 mL $CH_2Cl_2$ and washed with brine (100 mL×2). The organic layer was dried over $MgSO_4$, and concentrated under reduced pressure. The residue was purified by flash column chromatography using 0.3% methanol/$CH_2Cl_2$ as the eluent to give compound **3** (**BDP 3**) as a red solid (5.29 g, 91.3%). $^1$H NMR (400 MHz, $CDCl_3$): δ (ppm) 7.12 (d, *J* = 8.7 Hz, 2H), 7.05 (d, *J* = 8.7 Hz, 2H), 4.23–4.17 (m, 2H), 3.95–3.89 (m, 2H), 3.79–3.72 (m, 6H), 3.67–3.61 (m, 2H), 2.63 (s, 6H), 2.42 (s, 1H), 1.43 (s, 6H). $^{13}$C NMR (101 MHz, $CDCl_3$): δ (ppm) 159.82, 156.69, 145.48, 141.62, 131.82, 129.20, 127.06, 115.61, 85.65, 77.48, 77.16, 76.84, 72.58, 70.99, 70.48, 69.79, 67.61, 61.90, 17.31, 16.13. HRMS (MALDI-TOF, m/z): calcd for $C_{25}H_{29}BF_2I_2N_2O_4$ ($[M+H]^+$) 724.0276; found 724.0297.

### *4.5.2 Photophysical Properties*

#### 4.5.2.1 Spectroscopic Characterization

Linear spectroscopic measurements of all materials were investigated in 10 mm path length quartz cuvettes at room temperature. Steady-state absorption was measured with an Agilent 8453 UV-visible spectrophotometer. Fluorescence emission and excitation spectra were obtained using an Edinburgh Photonics FLS980 spectrometer equipped with a thermoelectrical cooled photomultiplier (Hamamatsu). All the measurements were carried out with the optical density below 0.12 at excitation wavelength to avoid reabsorption. The excitation and fluorescence emission spectra were corrected for the spectral sensitivity of Edinburgh Photonics excitation and detection system by using factory measured correction files.

Fluorescence quantum yields were determined by a standard relative method (Equation 2 in Chapter 3) with Rhodamine 6G ($\Phi_{FL} \approx 0.94$ in ethanol) as a reference.[98]

#### 4.5.2.2 Quantum Yields Determination for Singlet Oxygen Generation ($\Phi_{\Delta}$)

Singlet oxygen generation quantum yields were determined using a direct measurement of near-infrared luminescence at 1270 nm.[123-125] The 1270 nm singlet oxygen emission was monitored by Edinburgh Photonics FLS980 spectrometer equipped with a liquid nitrogen cooled NIR-photomultiplier (Hamamatsu) with a long-pass filter (780LP). The single oxygen measurements of **BDP 3** in acetonitrile (ACN) were carried out with the optical density of 0.4 at excitation wavelength, while Acridine in ACN ($\Phi_{\Delta} \approx 0.82$)[126] was used as a reference.

### *4.5.3 Cytotoxicity Assay*

LLC cells, a Lewis lung carcinoma cell line, were cultured in Dulbecco's modified Eagle's Medium (DMEM, Invitrogen, Carlsbad, CA, USA) supplemented with 10% fetal bovine serum (FBS, Atlanta Biologicals, Lawrenceville, GA, USA), and 1% penicillin-streptomycin (Atlanta Biologicals, Lawrenceville, GA, USA) at 37 °C in a 95% humidified atmosphere containing 5% $CO_2$. The LLC cells were prepared for cell viability studies in 96-well plates ($5\times10^3$ cells per well). The cells were incubated for an additional 24 h with 10 $\mu$M **BDP 3**. The dye was first dissolved in DMSO at a concentration of ~$1\times10^{-3}$ M and then, diluted with the medium. After incubation, the cells were washed with PBS three times and fresh medium was added into each well. Subsequently, the cells were irradiated with a light dose of 3.5 mW/cm$^2$ from a filtered light source (522 ± 40 nm) for a different period of time. Following irradiation, the cells were further incubated for 22 h and then, 20 $\mu$L of CellTiter 96® Aqueous One Solution reagent (MTS assay) was added into each well, followed by further incubation for 2 h at 37 °C. The relative viability was determined by measuring the MTS-formazan absorbance on a microplate reader (Spectra Max M5, Molecular Devices, Sunnyvale, CA, USA) at 490 nm with subtraction of the absorbance of the cell-free blank volume at 490 nm. In addition to photoinduced cytotoxicity assay, dark cytotoxicity assay was conducted with the dye concentration range from 1 $\mu$M to 20 $\mu$M. Each assay was performed three times and the results from three individual experiments were averaged.

### *4.5.4 In Vitro Photosensitization Assay*

LLC cells were incubated for 24 h with 5 $\mu$M **BDP 3** on poly-D-lysin coated glass-bottomed petri dishes. The cells were then washed with PBS three times. Petri dishes were filled with fresh medium and irradiated with a mercury lamp (0.6 mW/cm$^2$) with a band pass filter (HQ522/40, Chroma Tech.Corp) for 10 min. Control cells were irradiated with the same power of light, but no **BDP 3** incubation in advance. Followed by 24 h incubation, the cells were further incubated with propidium iodide (PI) for 10 min. Glass bottoms were mounted with ProLong® Gold antifade reagent (Invitrogen, USA). Images were taken with Olympus IX-81 confocal microscope coupled with a 100 W mercury lamp. Fluorescence was collected using a TexRed filter cube (Ex 562/40, DM 593, Em 654/40).

### *4.5.5 Live Cell Imaging*

LLC cells were incubated for 24 h with 5 $\mu$M **BDP 3** on poly-D-lysine coated 40 mm coverslip. Coverslip was then washed with PBS three times and mounted onto bioptics live cell imaging chamber with warm culture medium. After irradiation with a mercury lamp (0.2 mW/cm$^2$) which was filtered with a band pass filter (HQ522/40) for 5 min, the cells were imaged with Olympus IX-81 DSU microscope at 1 min intervals for 30 min in DIC channel. Control cells were irradiated with the same power of light, but no **BDP 3** incubation in advance.

# APPENDIX A: PUBLICATIONS TO DATE FROM DISSERTATION WORK

1. Ahn, H. Y.; Fairfull-Smith, K. E.; Morrow, B. J.; Lussini, V.; Kim, B.; Bondar, M. V.; Bottle, S. E.; Belfield, K. D., Two-Photon Fluorescence Microscopy Imaging of Cellular Oxidative Stress Using Profluorescent Nitroxides. *J Am Chem Soc* **2012,** *134* (10), 4721-4730.
2. Sui, B.; Kim, B.; Zhang, Y.; Frazer, A.; Belfield, K. D., Highly Selective Fluorescence Turn-On Sensor for Fluoride Detection. *Acs Appl Mater Inter* **2013**, *5* (8), 2920-2923.
3. Zhang, Y.; Kim, B.; Yao, S.; Bondar, M. V.; Belfield, K. D., Controlled Aggregation and Enhanced Two-Photon Absorption of a Water-Soluble Squaraine Dye with a Poly(acrylic acid) Template. *Langmuir* **2013,** *29* (35), 11005-11012.
4. Zhang, Y.; Yue, X.; Kim, B.; Yao, S.; Bondar, M. V.; Belfield, K. D., Bovine Serum Albumin Nanoparticles with Fluorogenic Near-IR-Emitting Squaraine Dyes. *Acs Appl Mater Inter* **2013,** *5* (17), 8710-8717.
5. Zhang, X.; Xiao, Y.; Qi, J.; Qu, J.; Kim, B.; Yue, X.; Belfield, K. D., Long-Wavelength, Photostable, Two-Photon Excitable BODIPY Fluorophores Readily Modifiable for Molecular Probes. *J Org Chem* **2013,** *78* (18), 9153-9160.
6. Zhang, Y.; Yue, X.; Kim, B.; Yao, S.; Belfield, K. D., Deoxyribonucleoside-Modified Squaraines as Near-IR Viscosity Sensors. *Chem-Eur J* **2014,** *20* (24), 7249-7253.
7. Sui, B.; Tang, S.; Liu, T.; Kim, B.; Belfield, K. D., Novel BODIPY-Based Fluorescence Turn-on Sensor for $Fe^{3+}$ and Its Bioimaging Application in Living Cells. *Acs Appl Mater Inter* **2014**, *6* (21), 18408-14812

# APPENDIX B: SUPPORTING INFORMATION OF CHAPTER 2

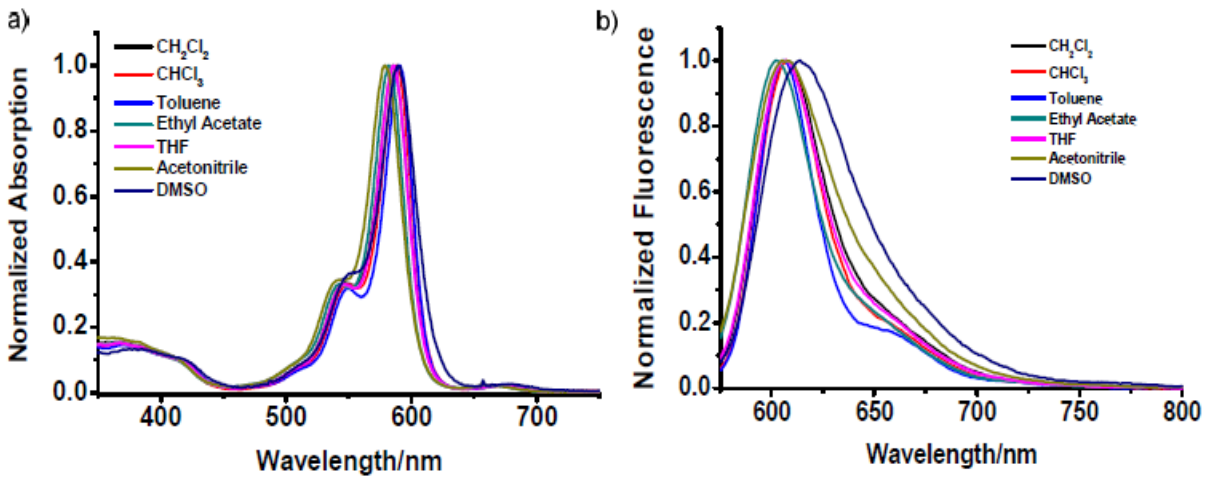


**Figure B-1:** Absorption (a) and fluorescence (b) spectra of **SPC** in different solvents.

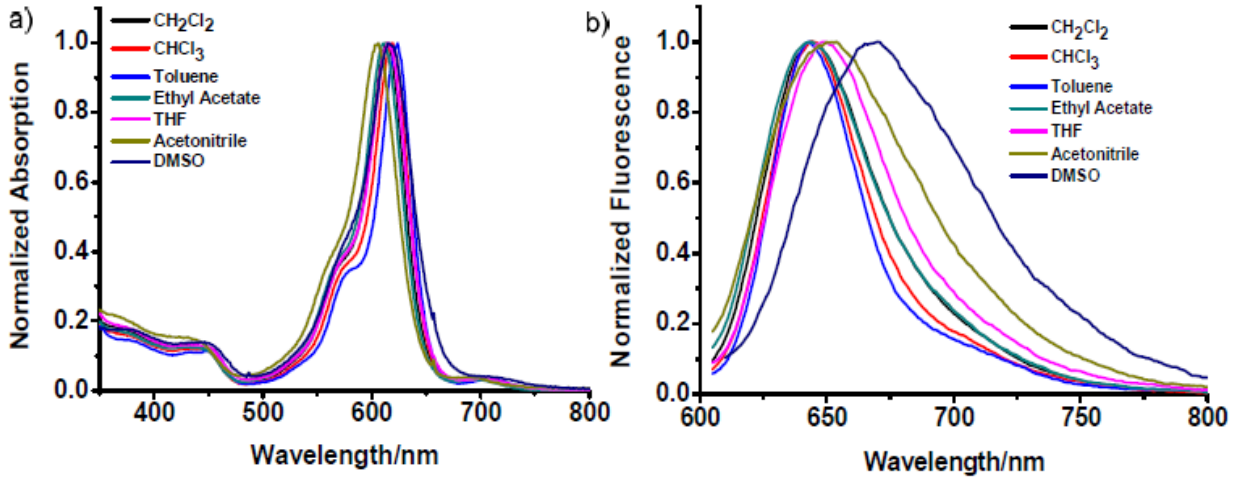


**Figure B-2:** Absorption (a) and fluorescence (b) spectra of **DC-SPC** in different solvents.

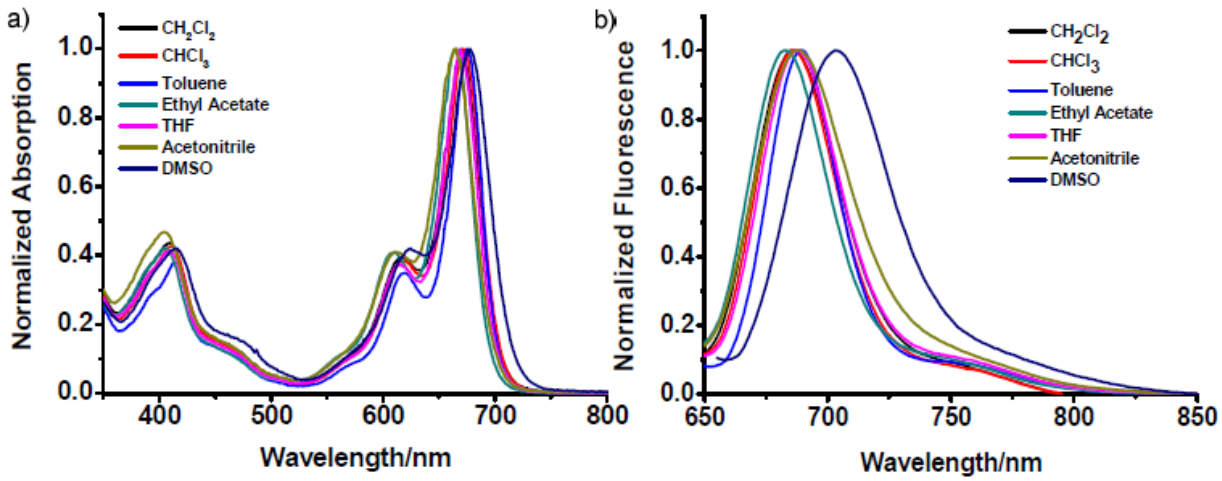


**Figure B-3:** Absorption (a) and fluorescence (b) spectra of **DPC** in different solvents.

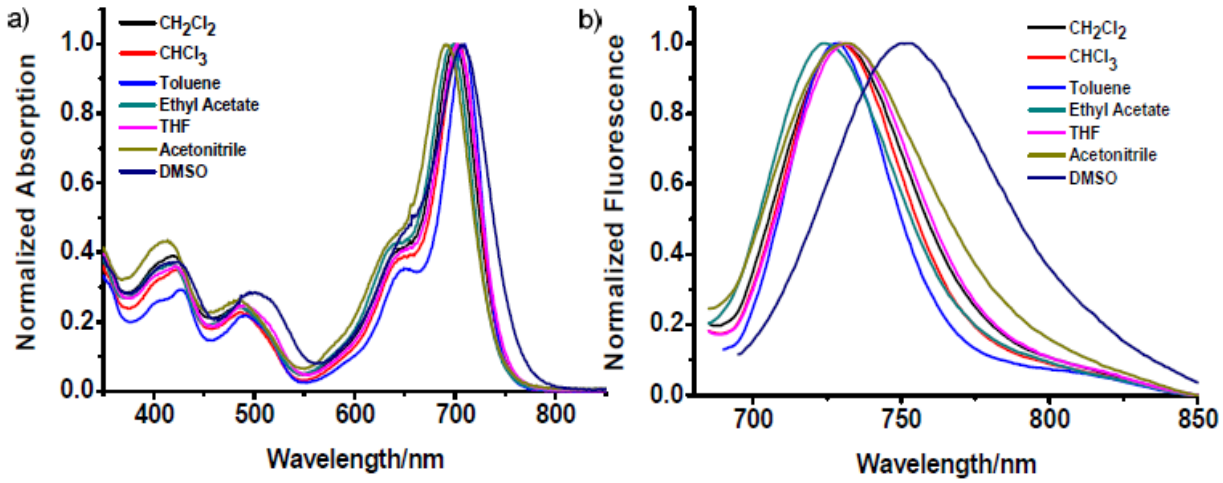


**Figure B-4:** Absorption (a) and fluorescence (b) spectra of **DC-DPC** in different solvents.

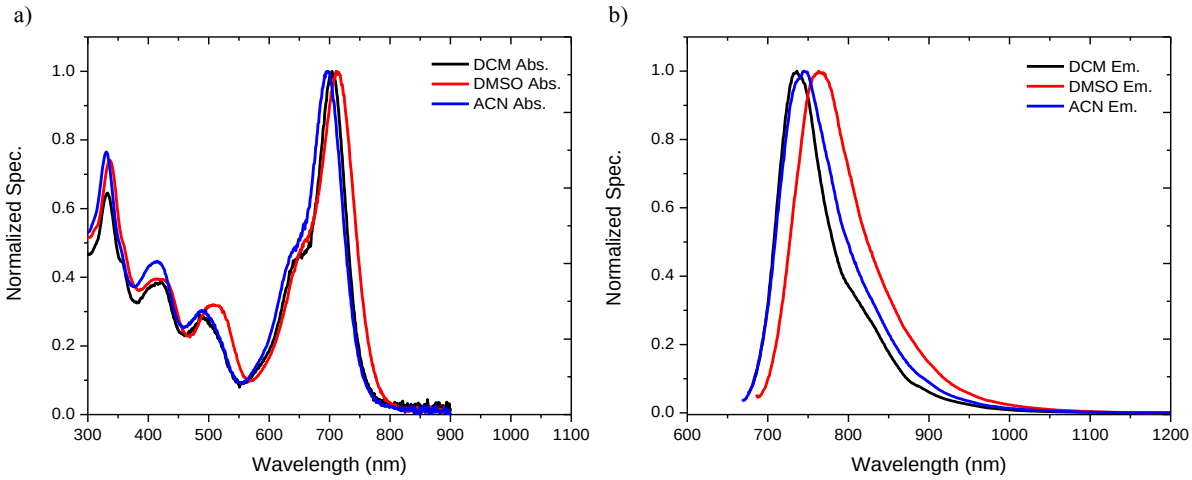


**Figure B-5:** Absorption (a) and fluorescence (b) spectra of **DC-DPC-PPh3** in different solvents.

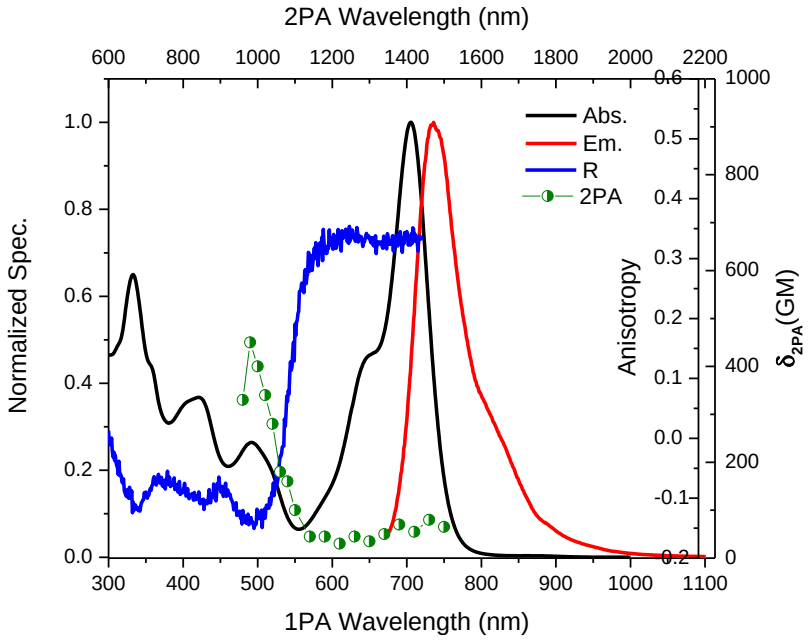


**Figure B-6:** Linear and nonlinear optical spectra of **DC-DPC-PPh3** in DCM (1 GM (Göppert Mayer) = $10^{-50}$·cm$^4$·s·photon$^{-1}$). Linear absorption (black), emission (red), excitation anisotropy (blue) spectra, and 2PA cross sections (green circles).

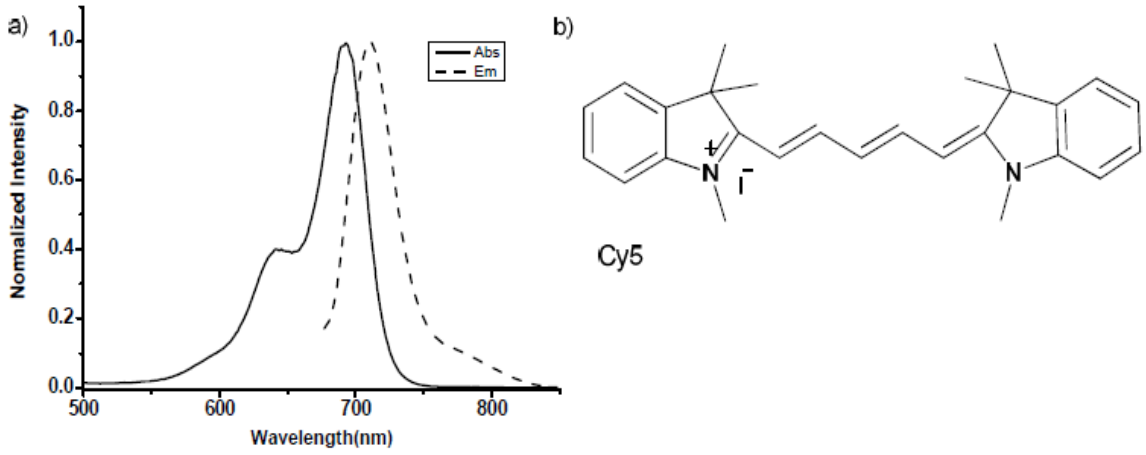


**Figure B-7:** (a) Absorbance (solid) and fluorescence (dash) spectra of Cy5 in $CHCl_3$. (b) Structure of Cy5.

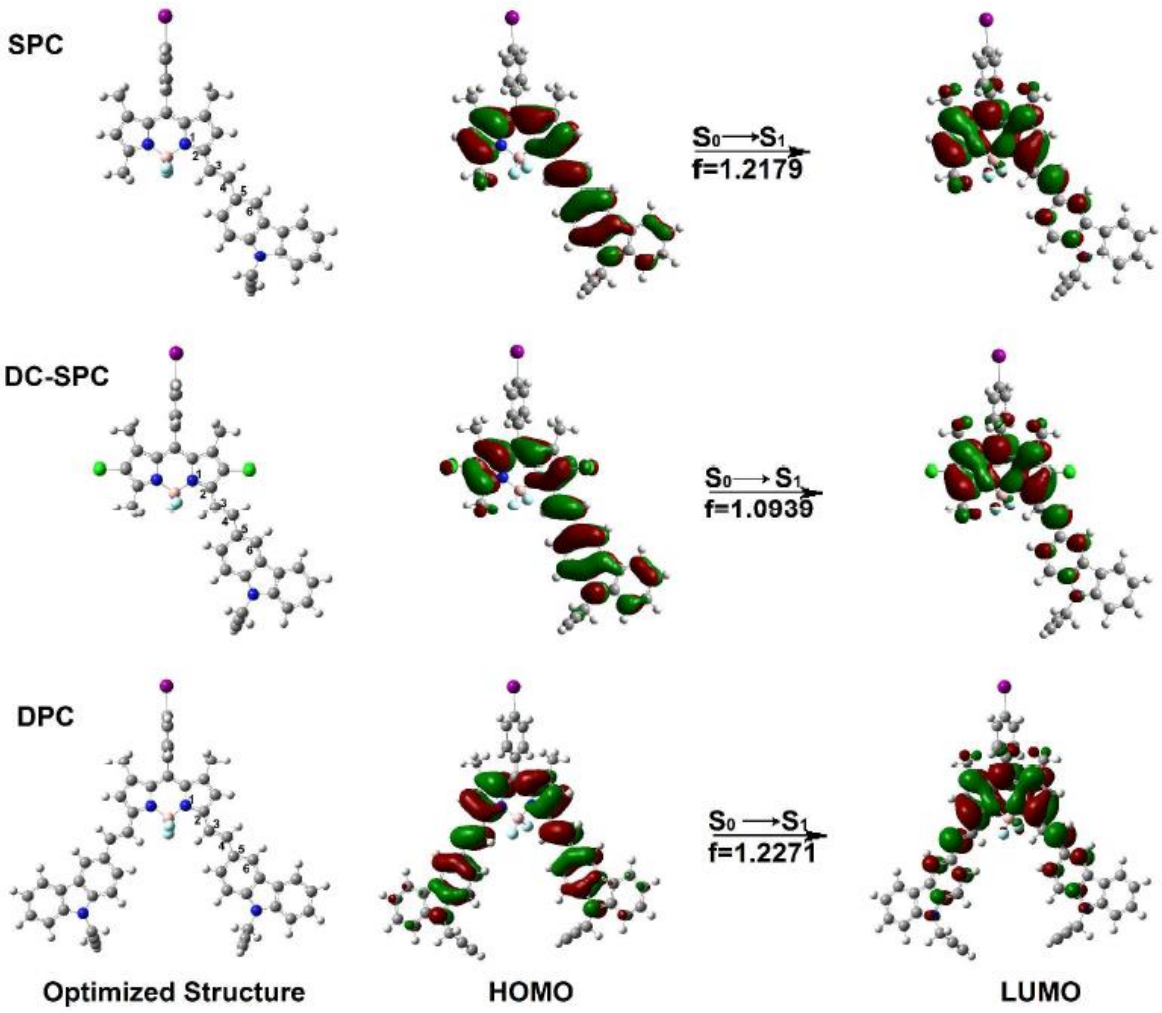


**Figure B-8:** The HOMO and LUMO electron distribution of **SPC**, **DC-SPC** and **DPC**.

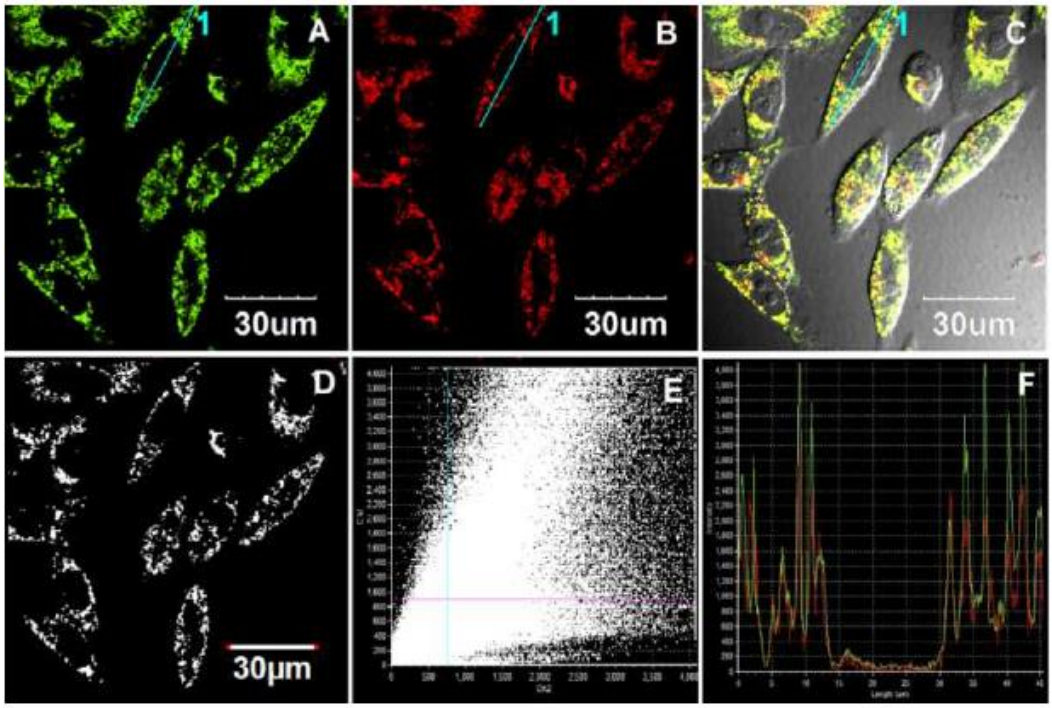


**Figure B-9:** Fluorescence image of MCF-7 cells costained with **DC-SPC-PPh3** and Rh-123. (A) 1PFM image of MCF-7 stained with Rh-123 (25 nM) ($\lambda_{ex}$ = 488 nm, $\lambda_{em}$ = 500−560 nm, pseudo-color green). (B) 1PFM image of MCF-7 incubated with **DC-SPC-PPh3** (37.5 nM) ($\lambda_{ex}$ = 559 nm, $\lambda_{em}$ = 600−660 nm, pseudo-color red). (C) Overlay of (A), (B) and brightfield. (D) Simulate image (the white pixels represented by the scatter plot (E) is on the up right corner. Pearson's coefficient 0.863). (E) Intensity correlation plot of stain Rh-123 and **DC-SPC-PPh3**. (F) Intensity profile of region of interest (ROI) cross MCF-7 cell.

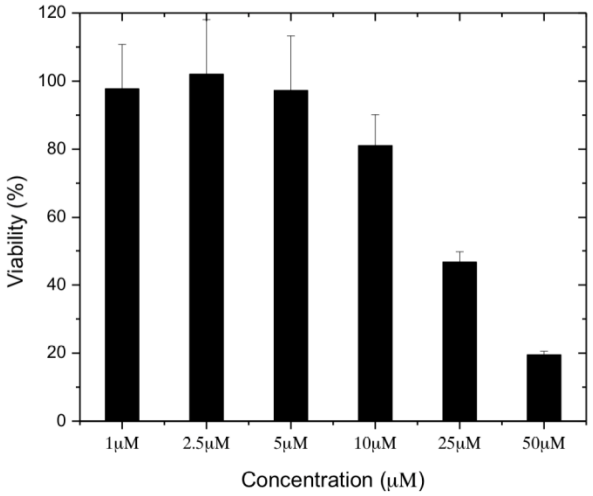


**Figure B-10:** Viability of HCT 116 cells with **DC-DPC-PPh3**.

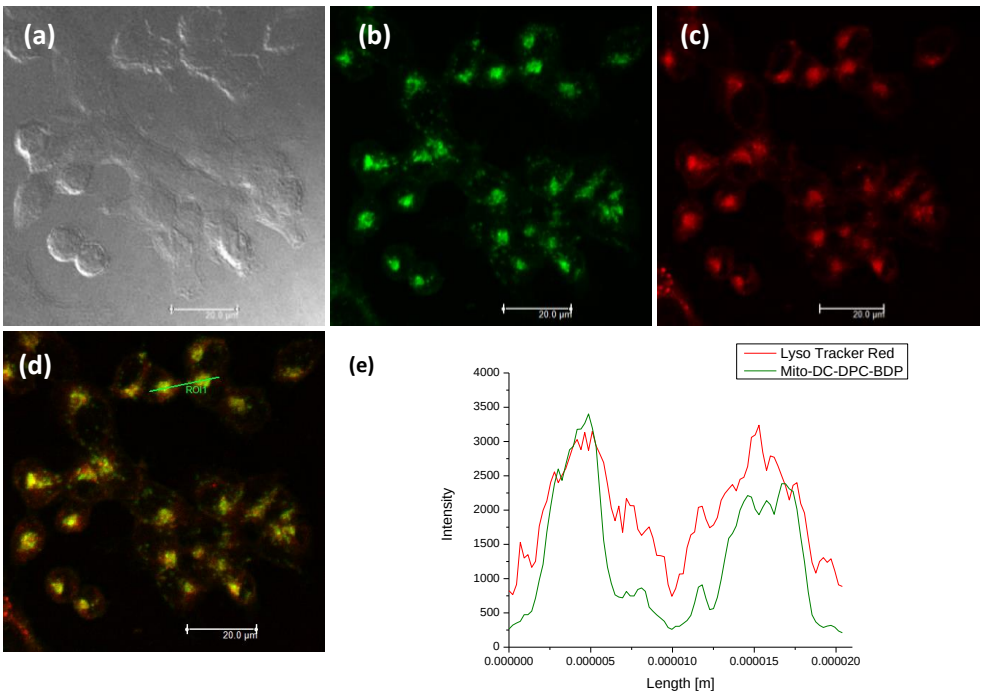


**Figure B-11:** Colocalization images of HCT 116 cells incubated with **DC-DPC-PPh3** (1 *u*M, 4 h) and Lysotracker Red (100 nM, 1 h). (a) differential interference contrast (DIC) image, (b) channel to observe **DC-DPC-PPh3**, (c) channel to observe Lysotracker Red, (d) overlaid image of panels b and c, (e) fluorescence intensity distribution through green line in panel d (Manders' colocalization coefficient 0.90).

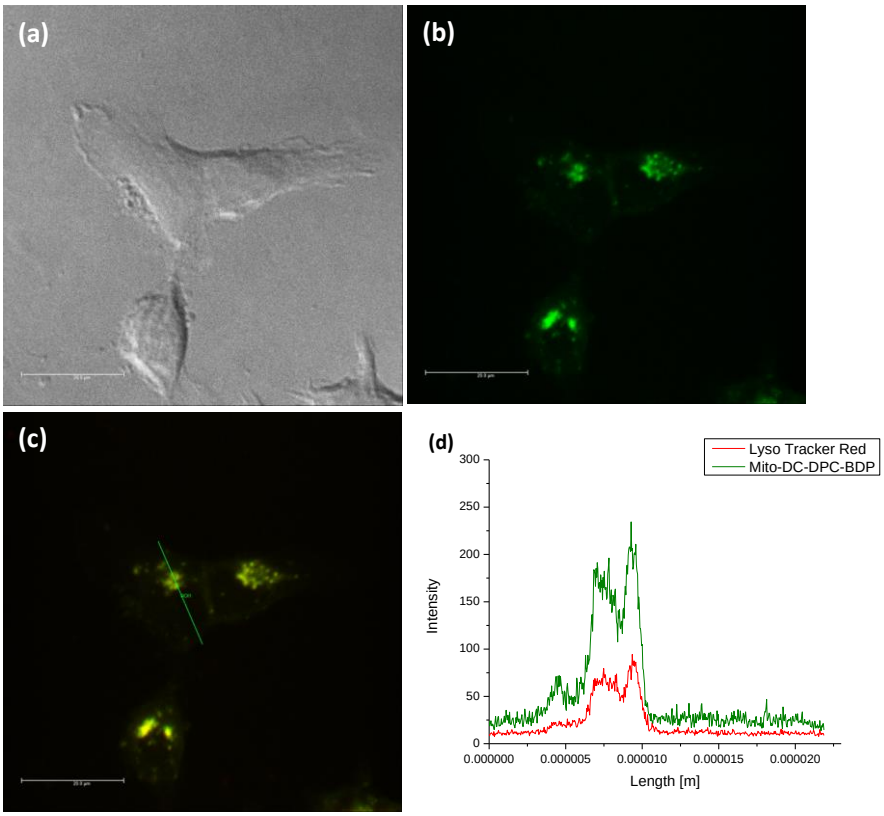


**Figure B-12:** 2PFM images from excitation at 1000 nm of HCT 116 cells with **DC-DPC-PPh3** (1 *u*M, 4 h). (a) DIC, (b) two-photon fluorescence image, exciting at 1000 nm, (c) overlaid image of panel b and one-photon fluorescence image of Lysotracker Red, and (d) fluorescence intensity distribution through green line in panel c (Manders' colocalization coefficient 0.95).

$^{1}$H NMR spectrum of **SPC**

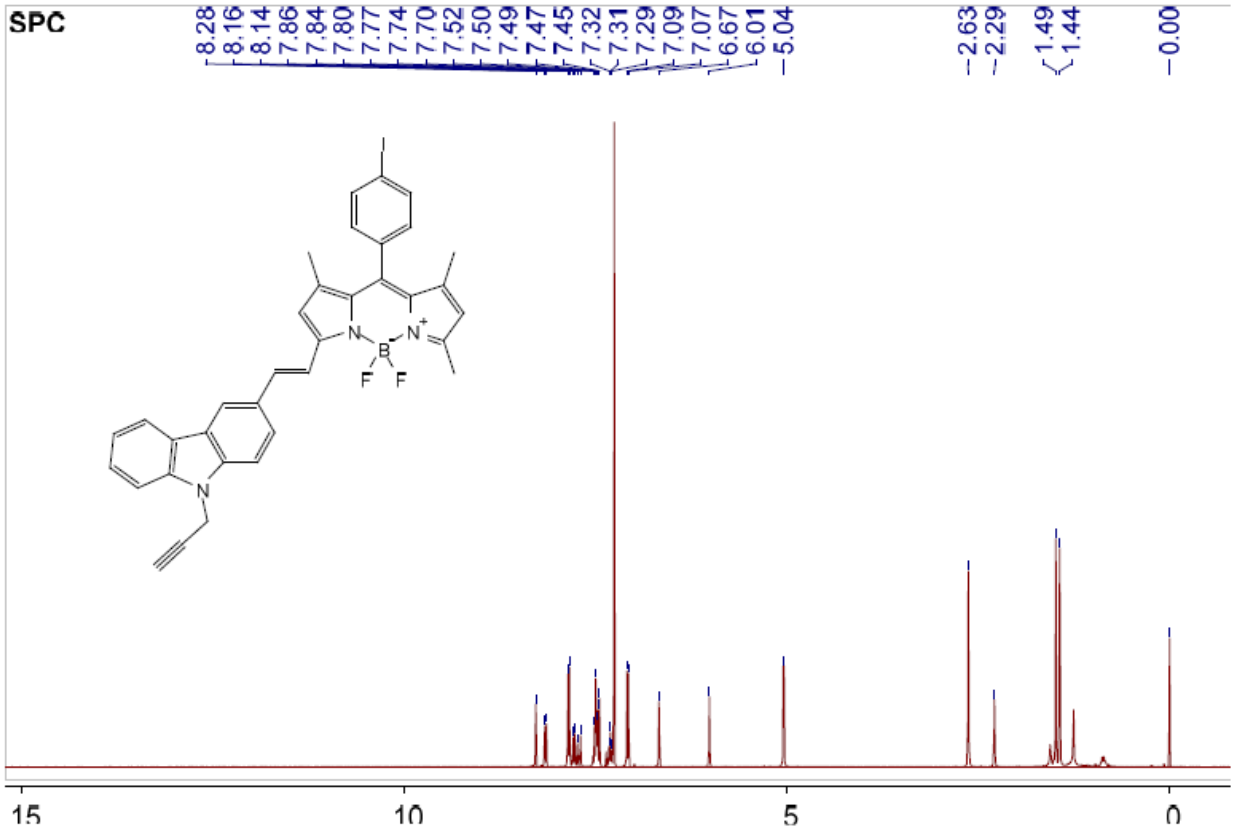

$^{13}$C NMR spectrum of **SPC**

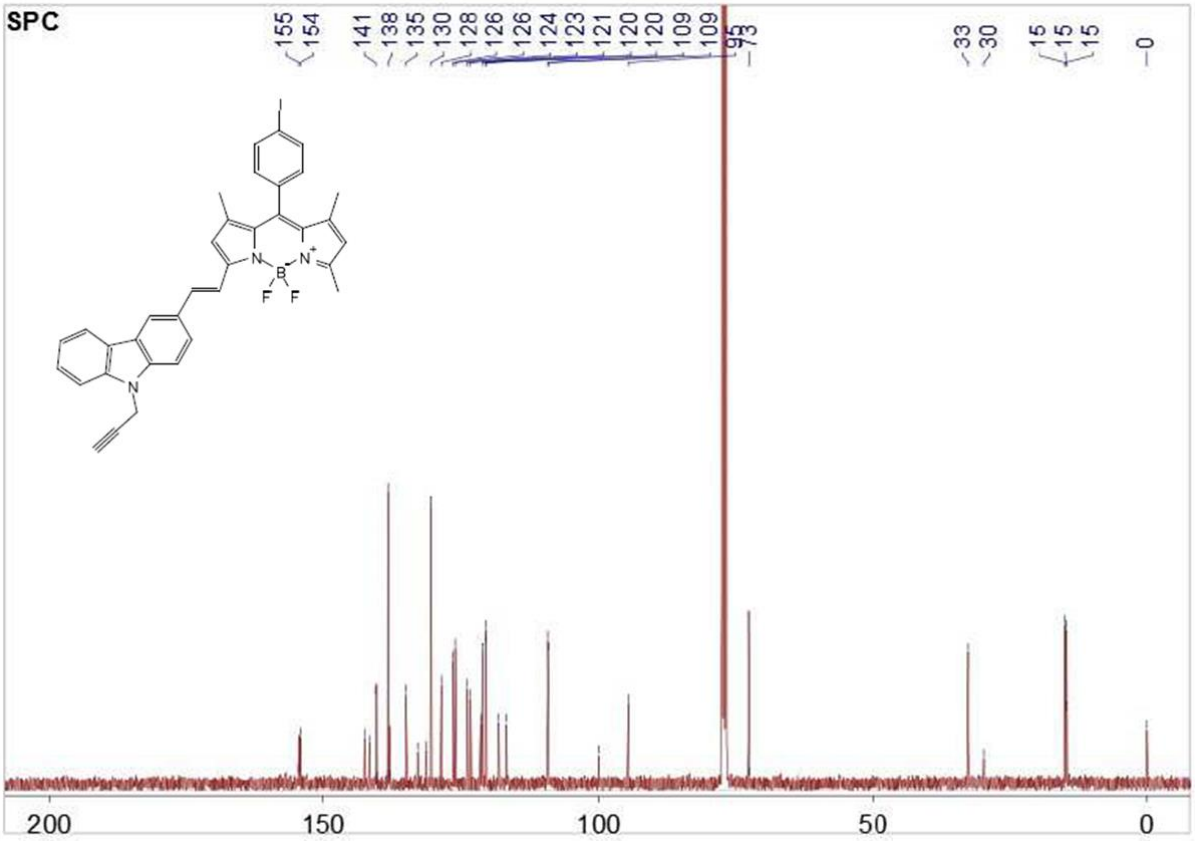

$^{1}$H NMR spectrum of **DC-SPC**

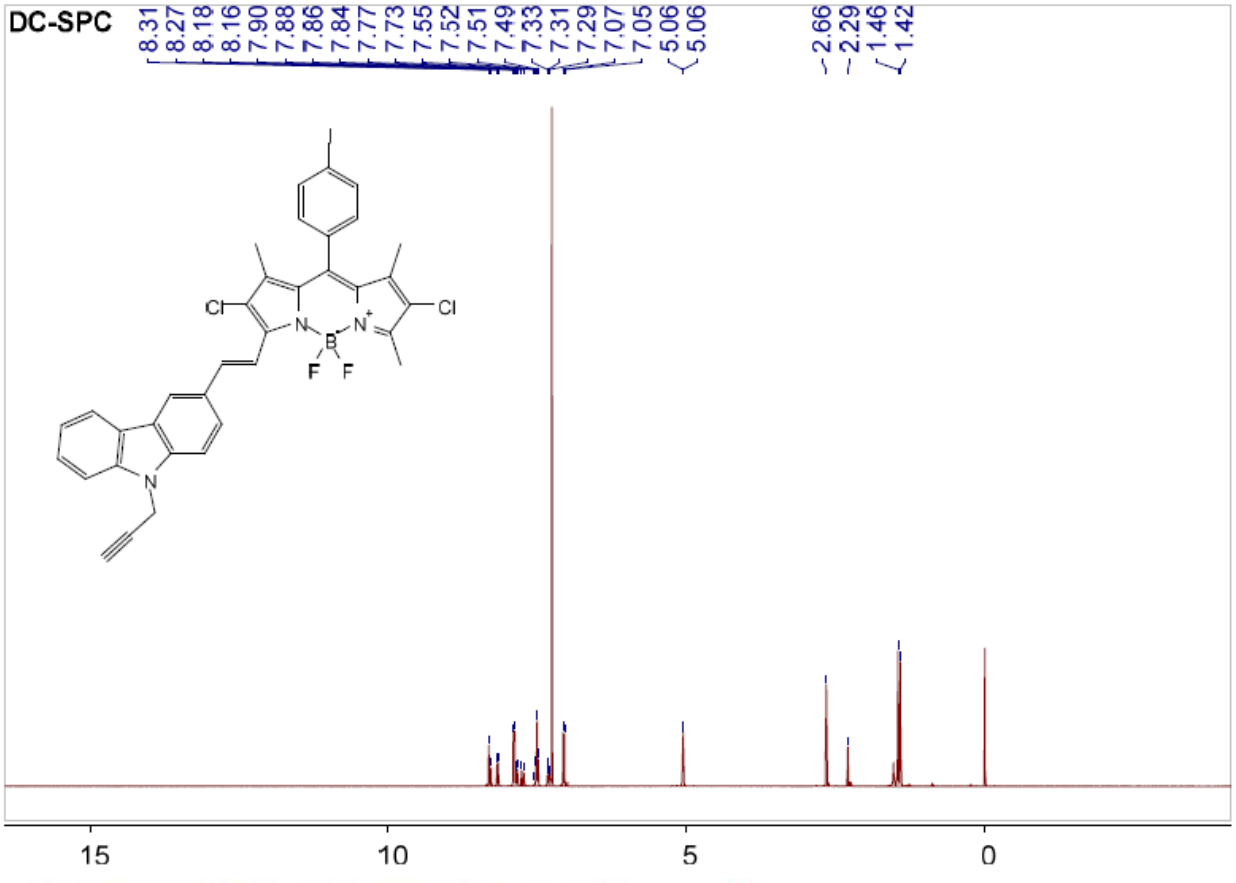

$^{13}$C NMR spectrum of **DC-SPC**

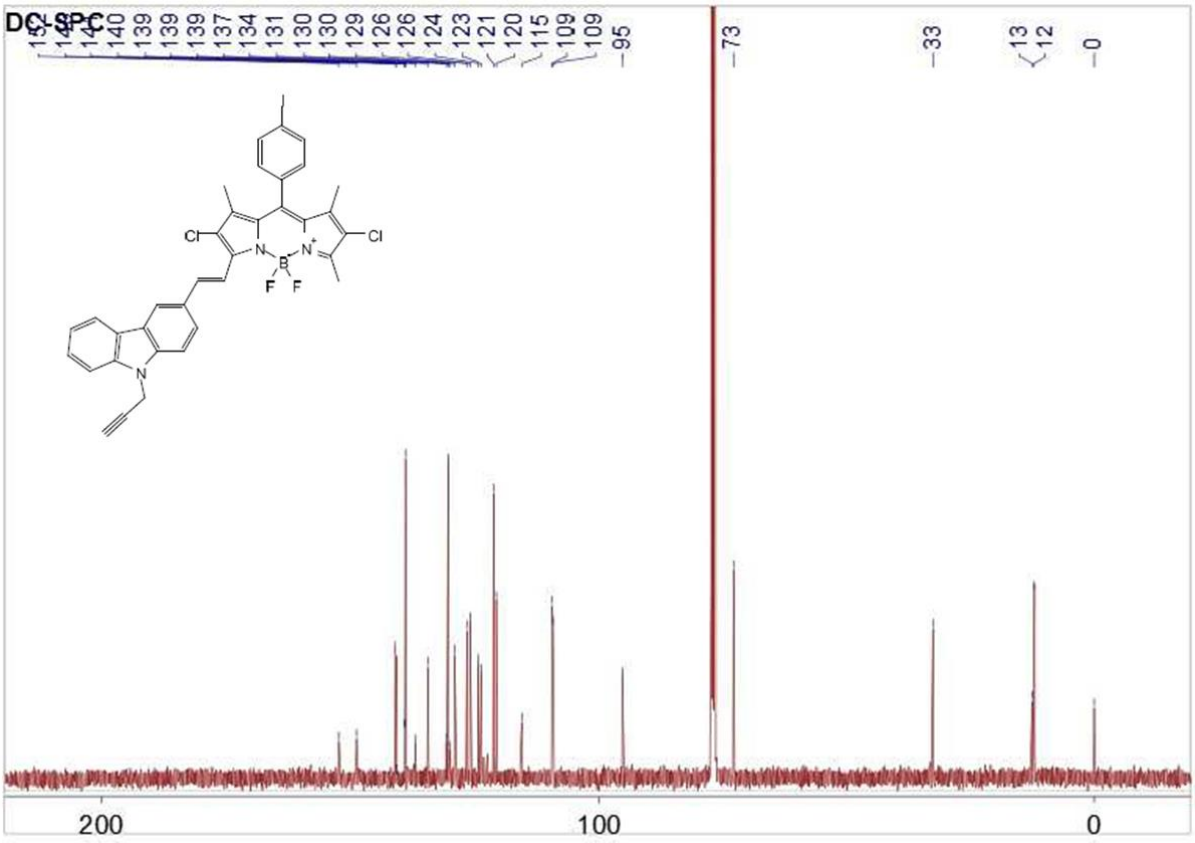

$^{1}$H NMR spectrum of **DPC**

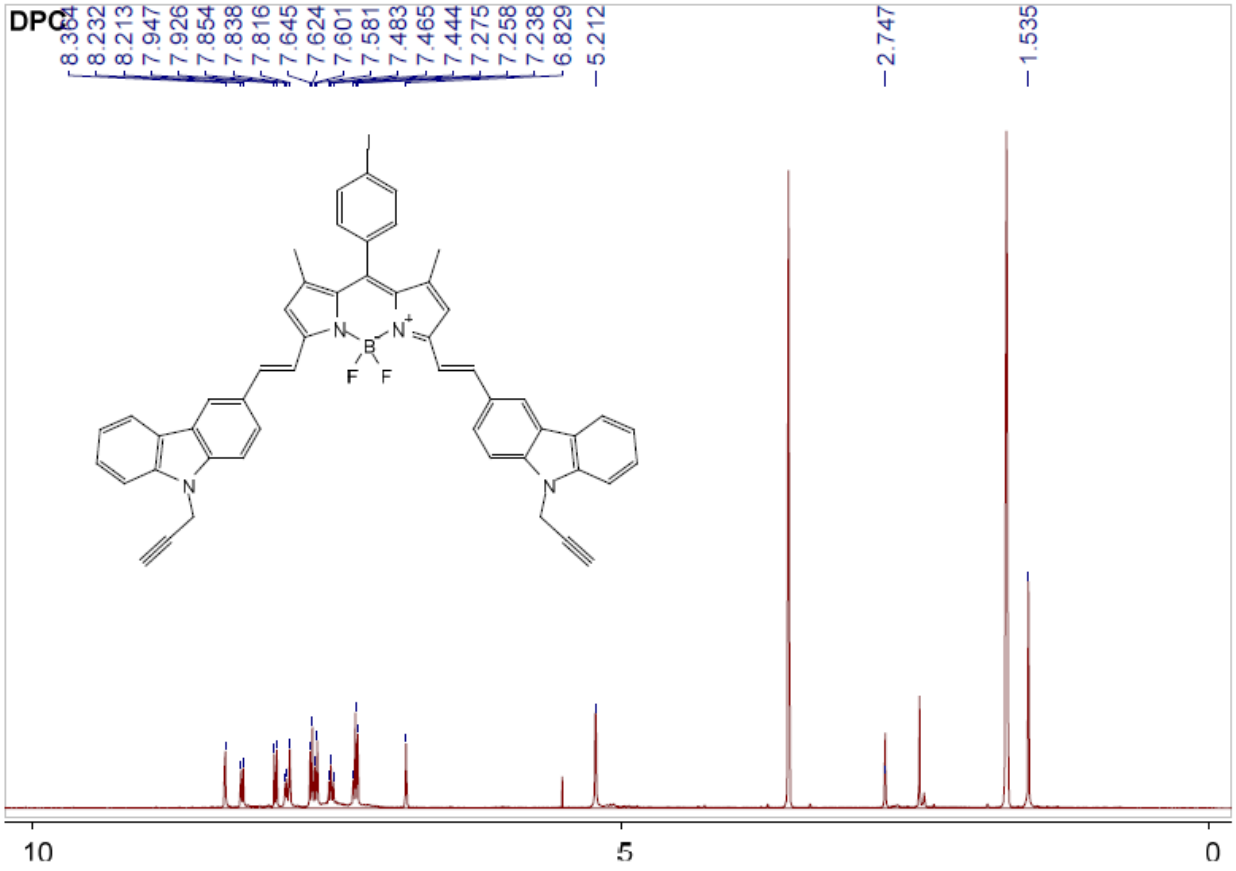

$^{13}$C NMR spectrum of **DPC**

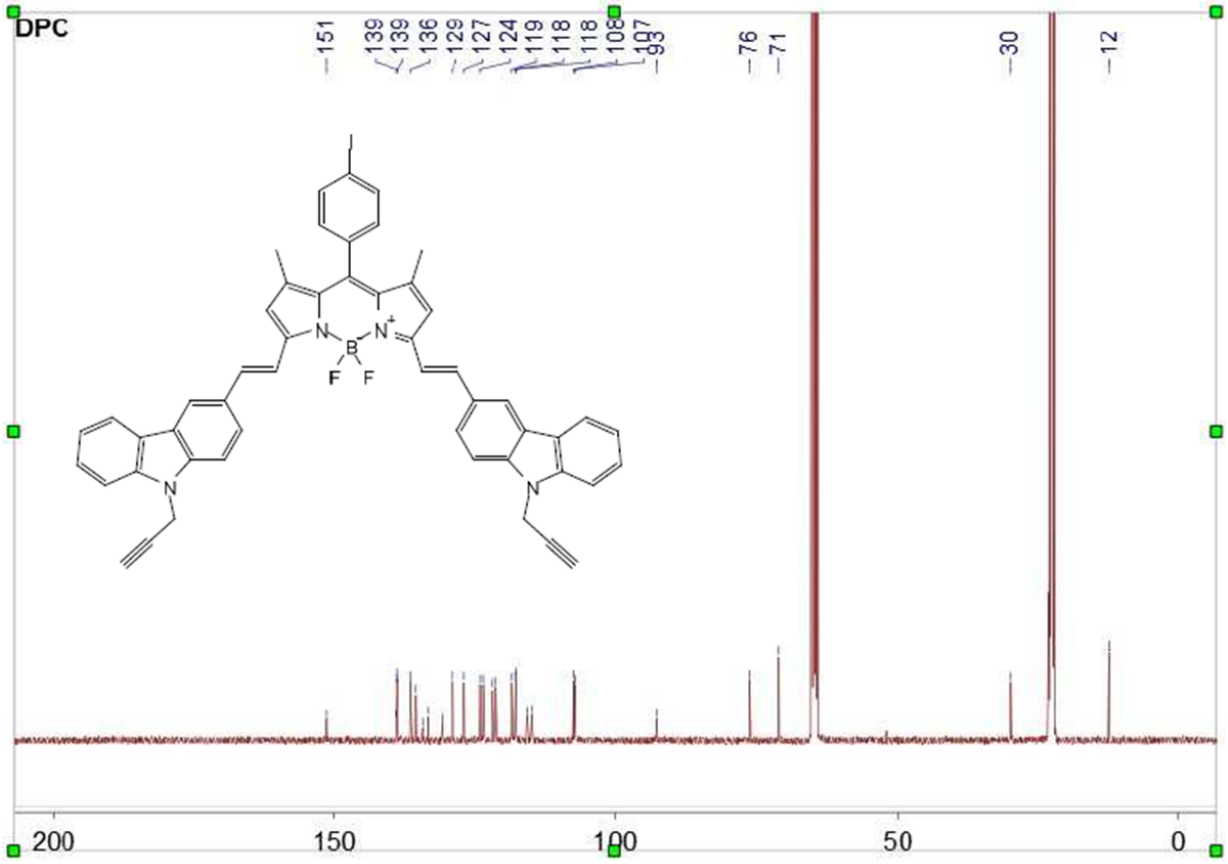

$^{1}$H NMR spectrum of **DC-DPC**

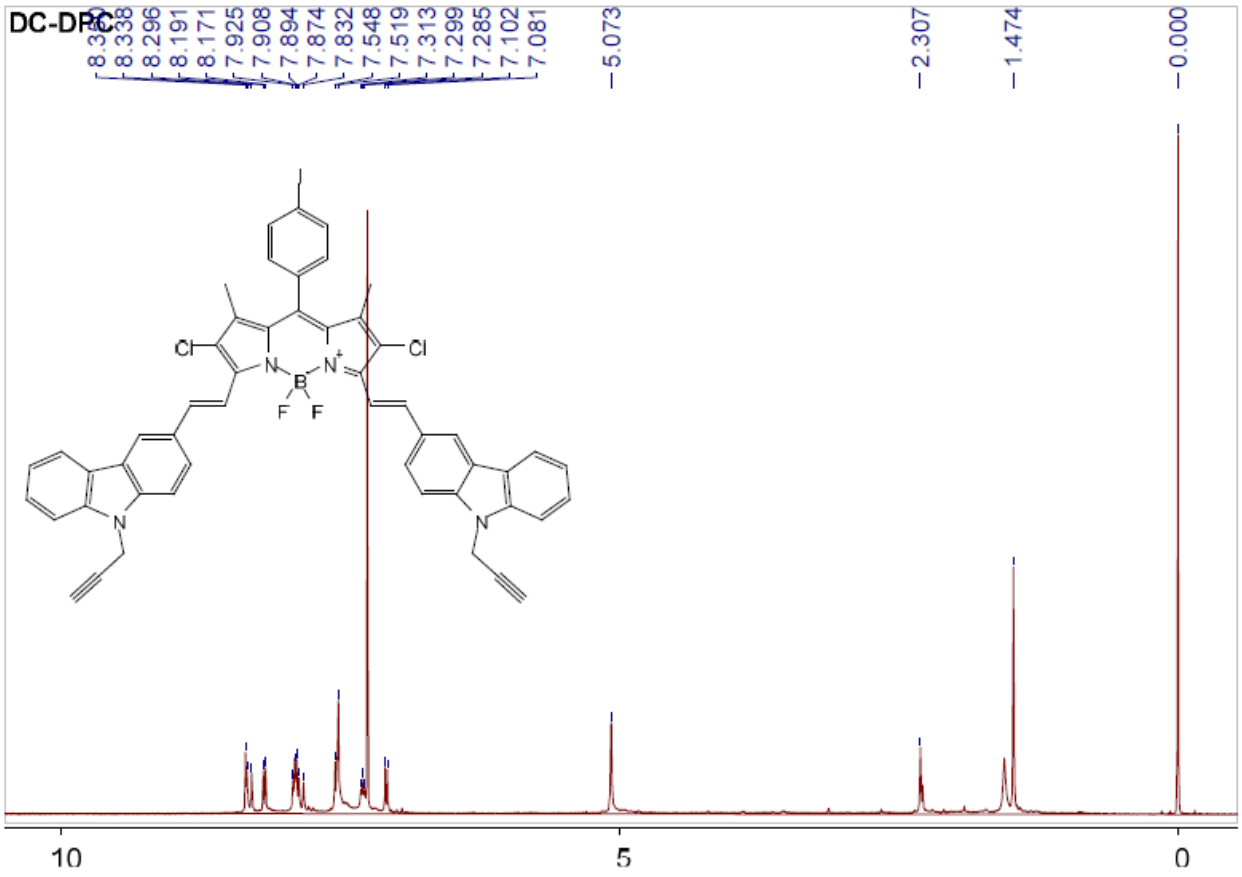

$^{1}$H NMR spectrum of **DC-SPC-PPh3**

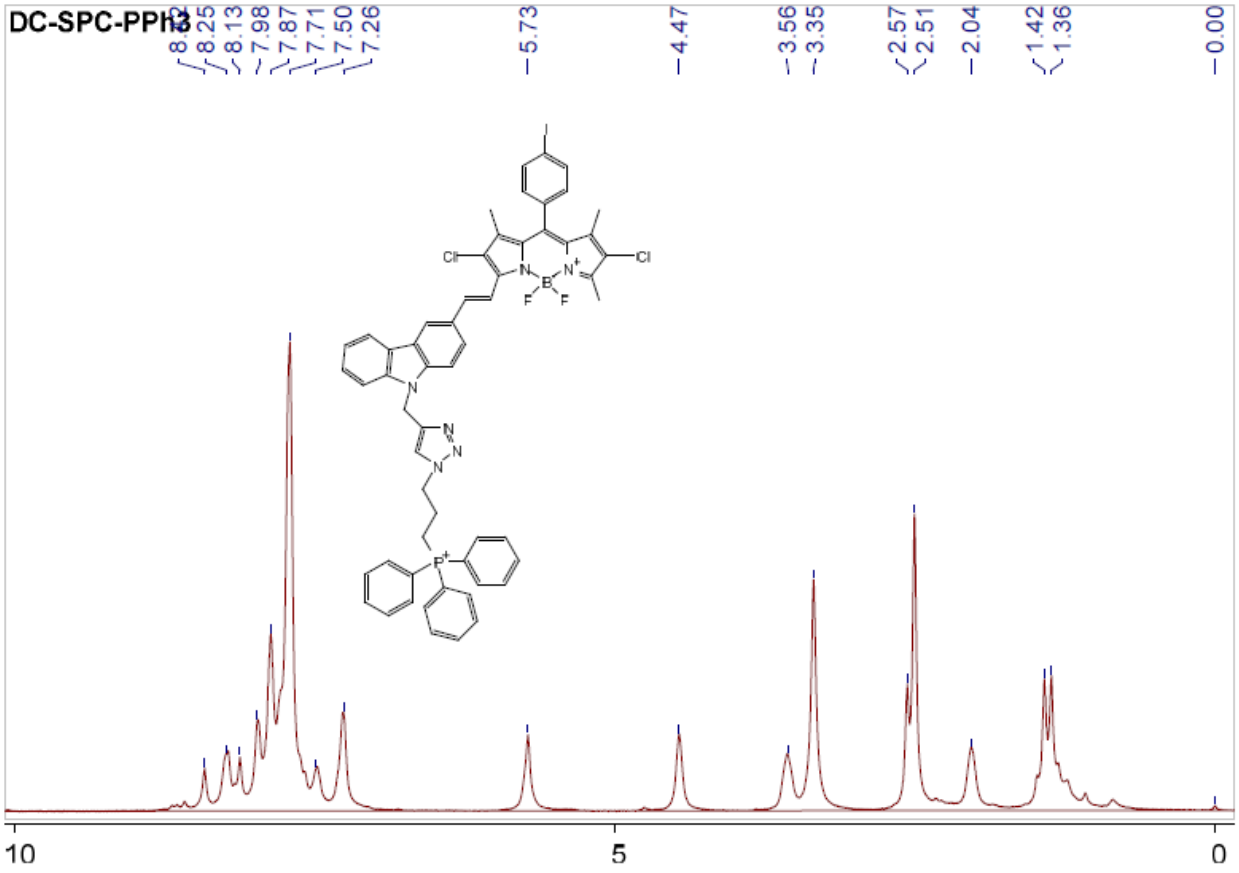

$^{13}$C NMR spectrum of **DC-SPC-PPh3**

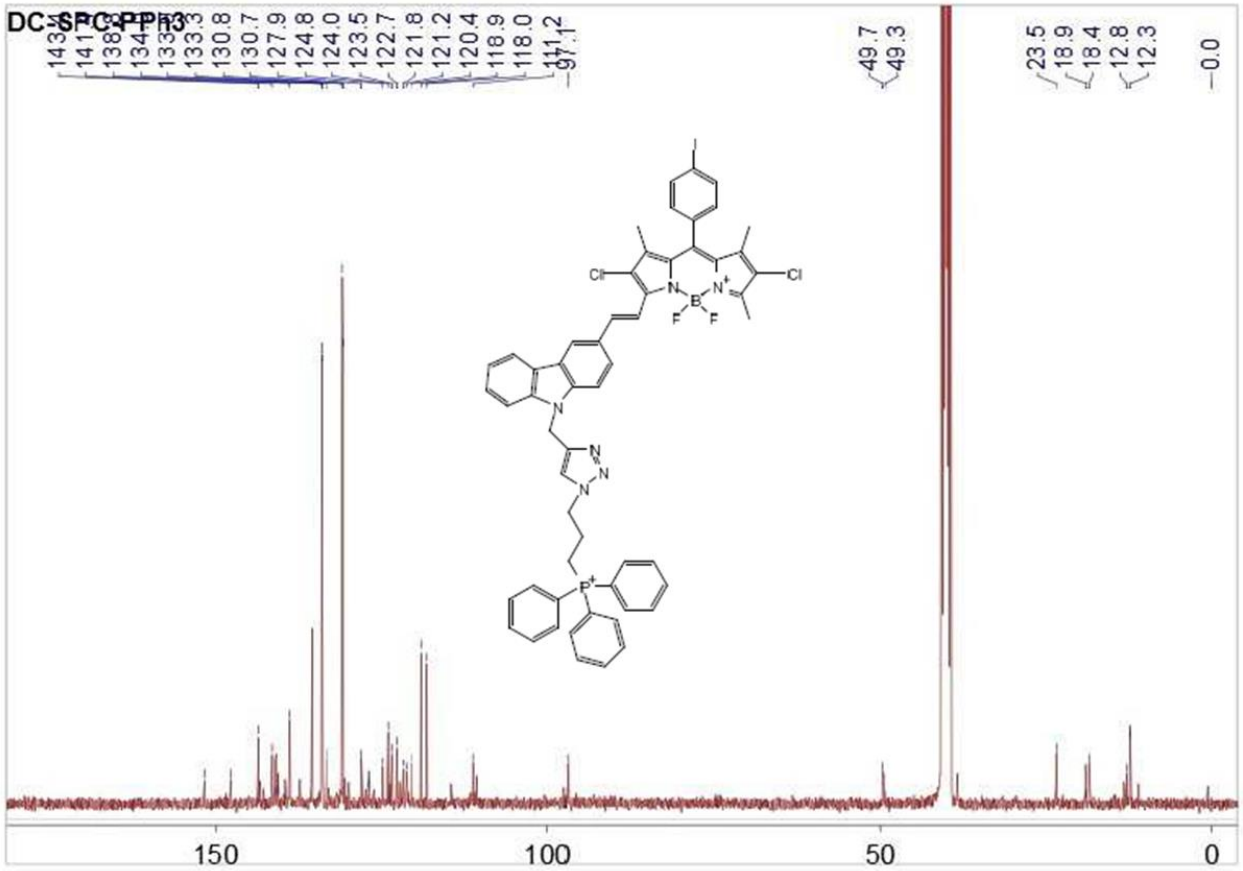

# APPENDIX C: SUPPORTING INFORMATION OF CHAPTER 3

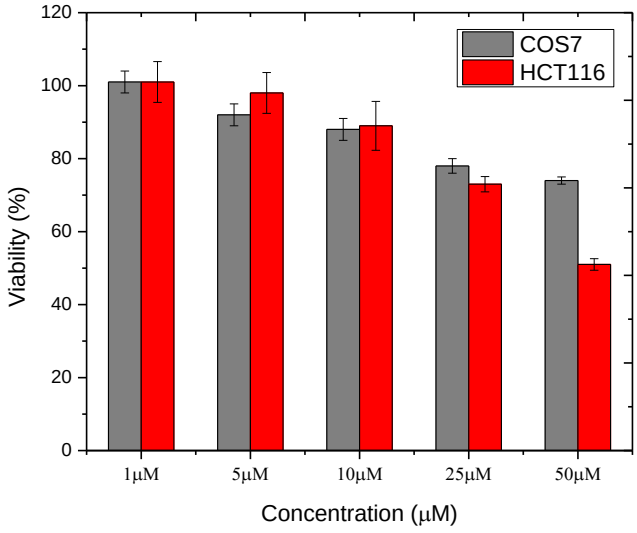


**Figure C-1:** Cell viability of COS 7 (gray) and HCT 116 (red) cells with **DDC**.

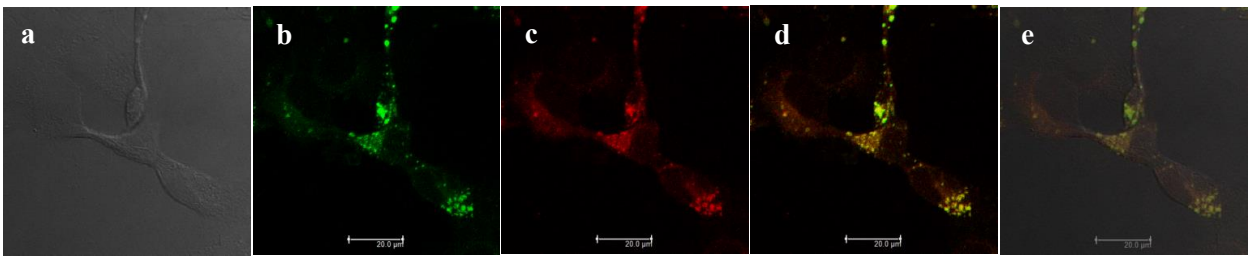


**Figure C-2:** Colocalization images of COS 7 cells incubated with **DDC** (20 $\mu$M, 2 h) and LT Red (100 nM, 2 h). (a) differential interference contrast (DIC) image, (b) one-photon fluorescence image of **DDC**, (c) one-photon fluorescence image of LT Red, (d) overlaid image of b and c, (e) overlaid image of a, b, and c (Pearson's correlation coefficient 0.91). 20 $\mu$m scale bar

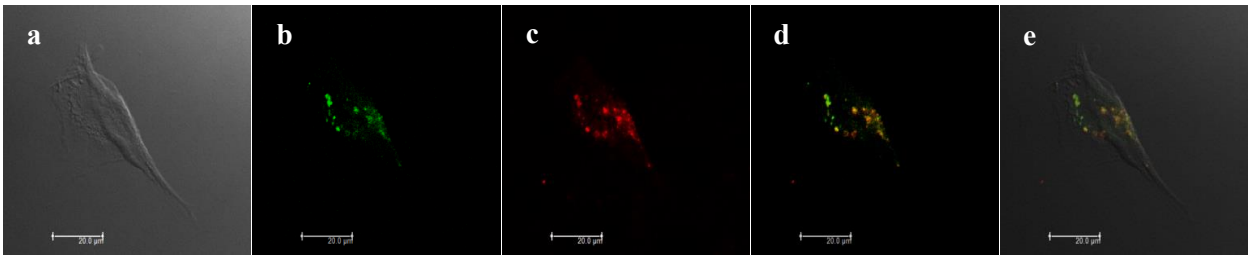


**Figure C-3:** Colocalization images of COS 7 cells incubated with **DDC** (20 $\mu$M, 2 h) and LT Red (100 nM, 2 h). (a) DIC image, (b) two-photon fluorescence image of **DDC**, (c) one-photon fluorescence image of LT Red, (d) overlaid image of b and c, (e) overlaid image of a, b, and c (Pearson's correlation coefficient 0.96). 20 $\mu$m scale bar

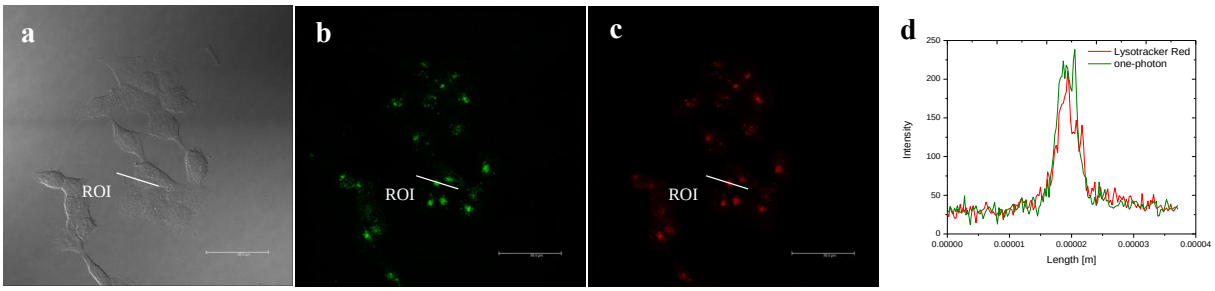


**Figure C-4:** Images of HCT 116 cells incubated with **DDC** (10 $\mu$M, 4 h) and LT Red (100 nM, 2 h). (a) DIC image, (b) one-photon fluorescence image of **DDC**, (c) one-photon fluorescence image of LT Red, and (d) fluorescence intensity profile of region of interest (ROI, white line) in (b) and (c); **DDC** (green) and LT Red (red). 50 $\mu$m scale bar

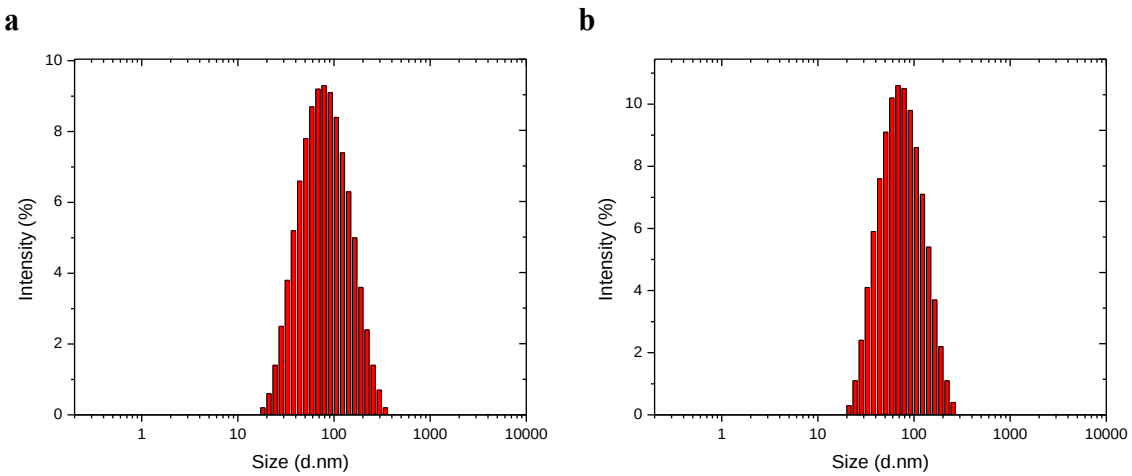


**Figure C-5:** Particle size distributions of (a) **SDC-SNP** in water and (b) **RGD-SDC-SNP** in water.

$^{1}$H NMR spectrum of **SDC**

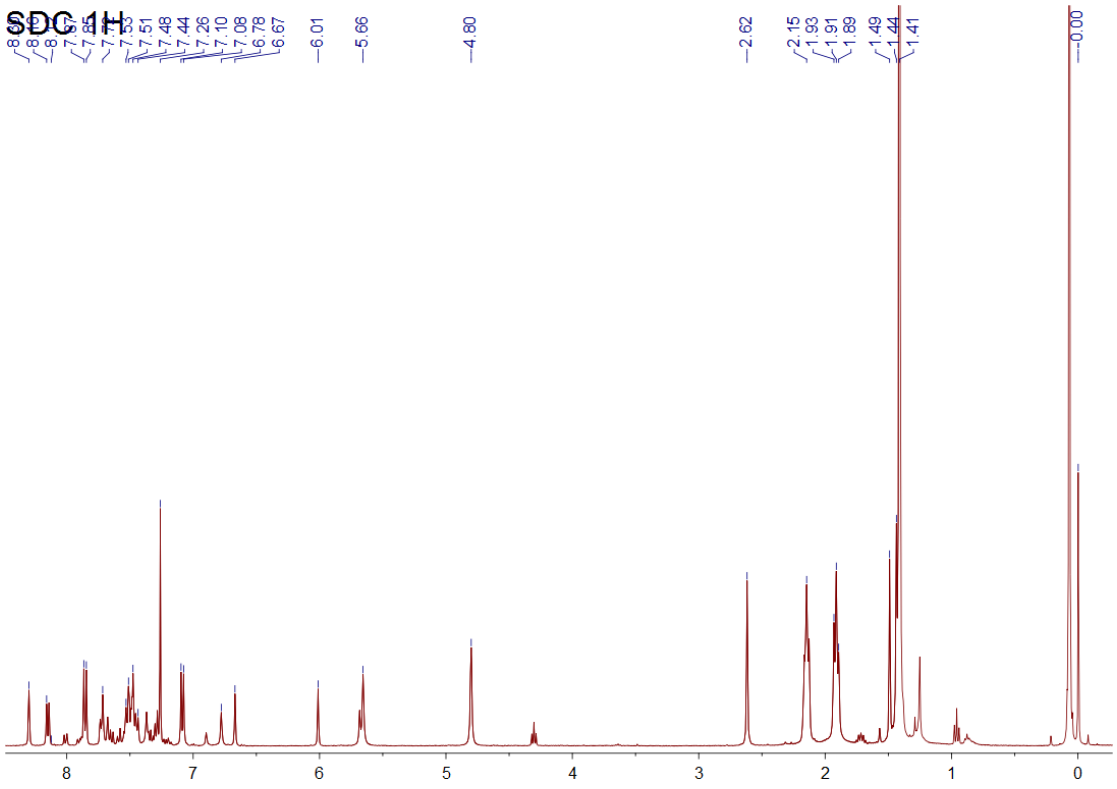

$^{13}$C NMR spectrum of **SDC**

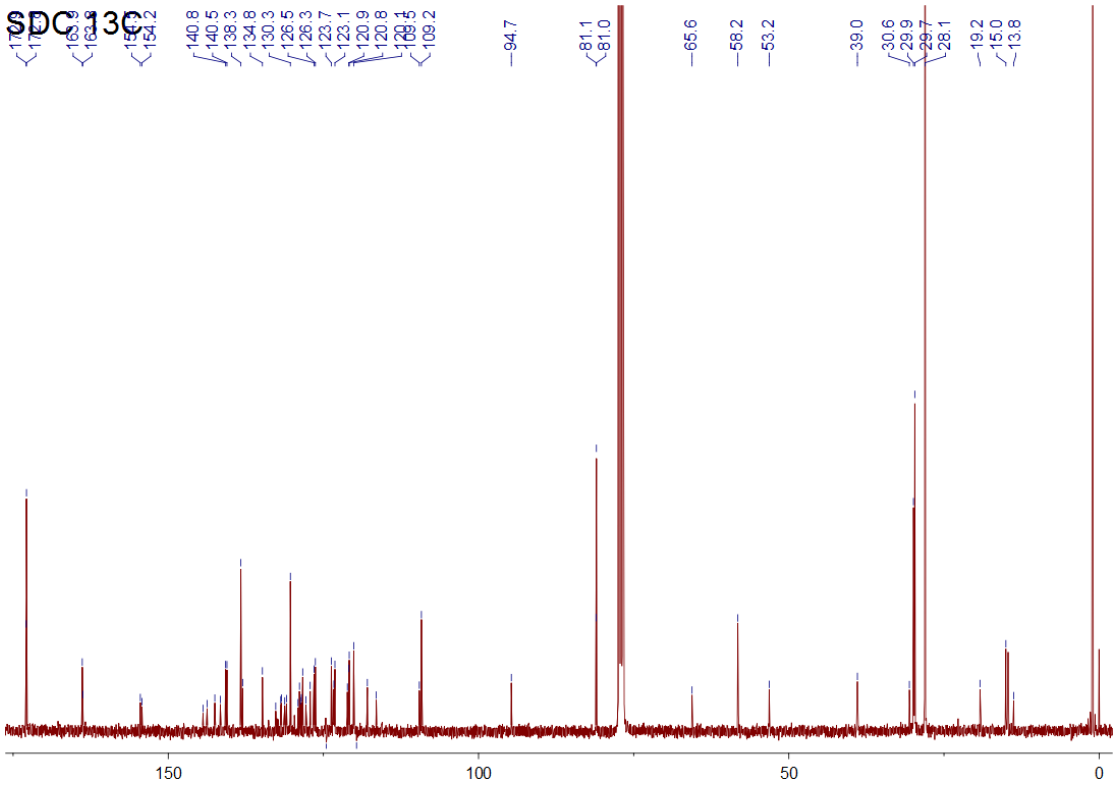

$^{1}$H NMR spectrum of **DDC**

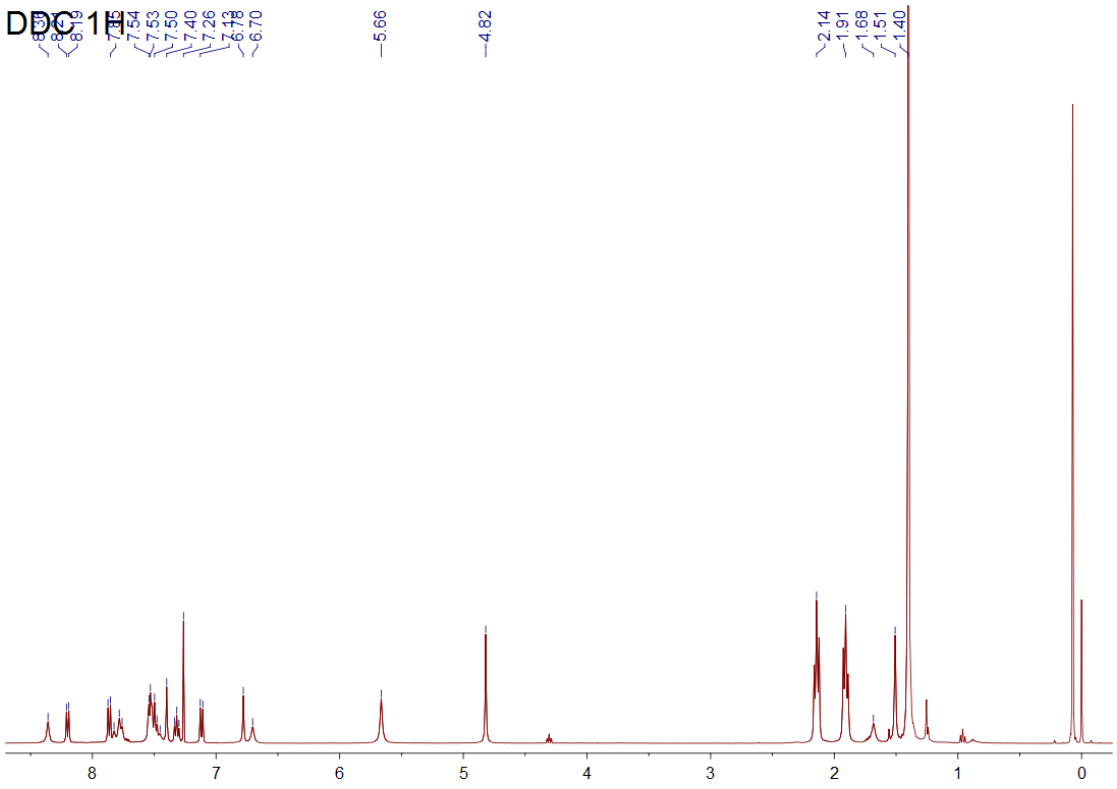

$^{13}$C NMR spectrum of **DDC**

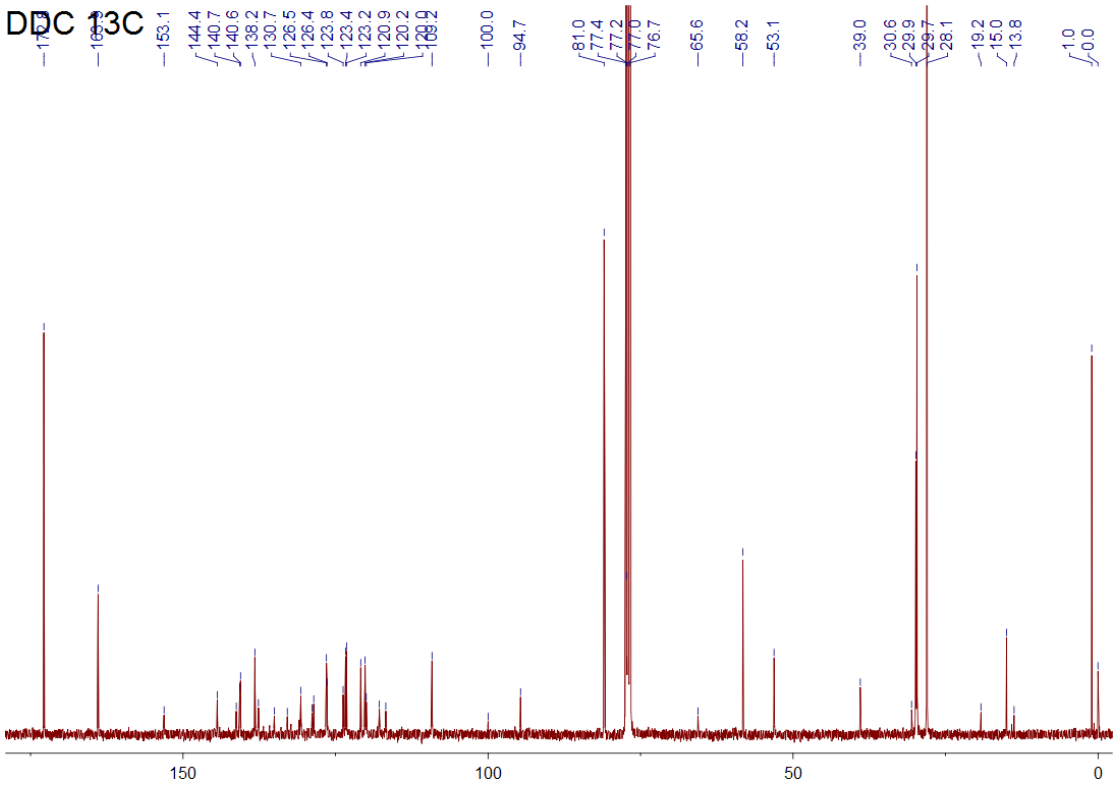

# APPENDIX D: SUPPORTING INFORMATION OF CHAPTER 4

$^{1}$H NMR spectrum of compound **2**

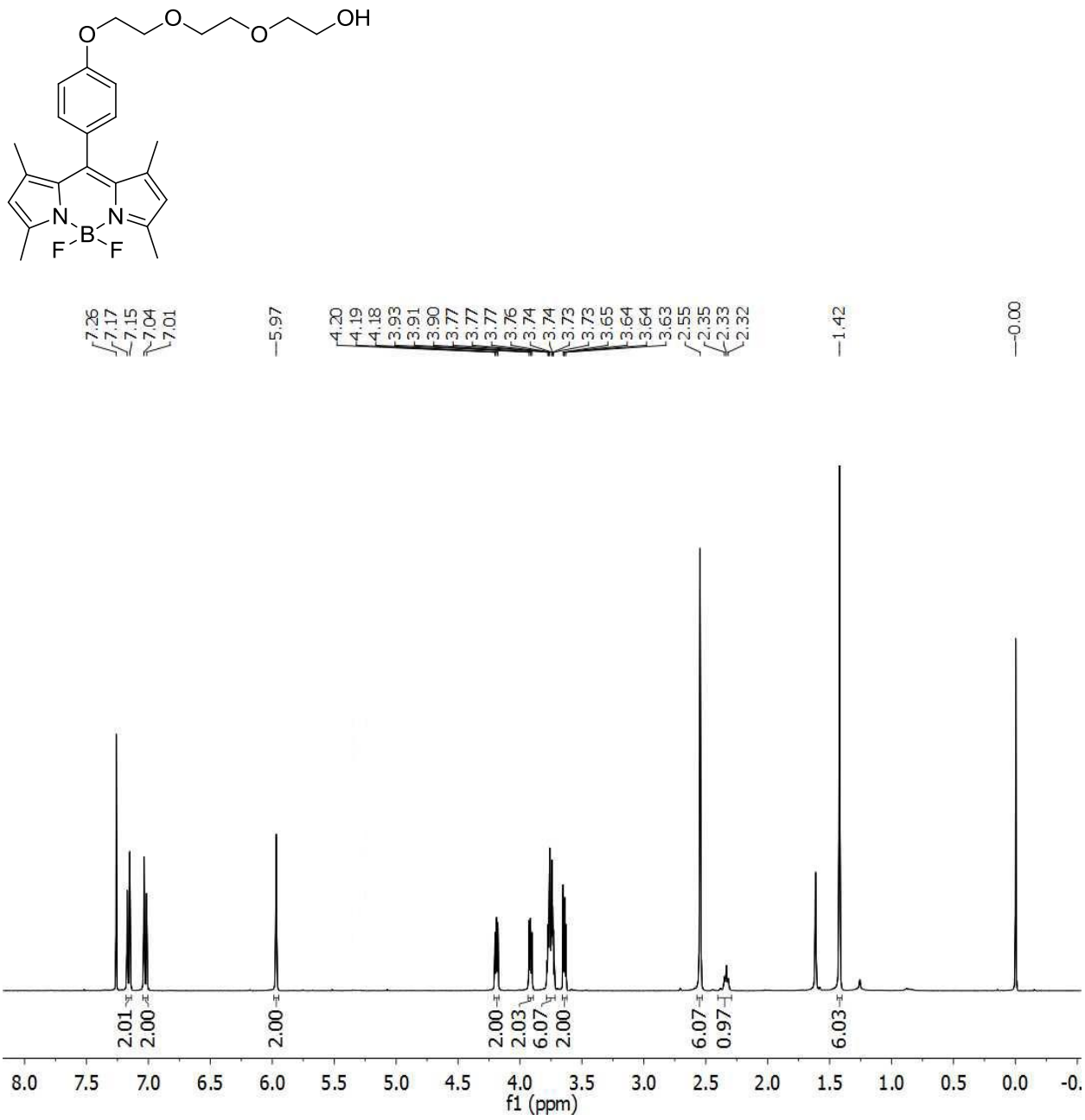

$^{13}$C NMR spectrum of compound **2**

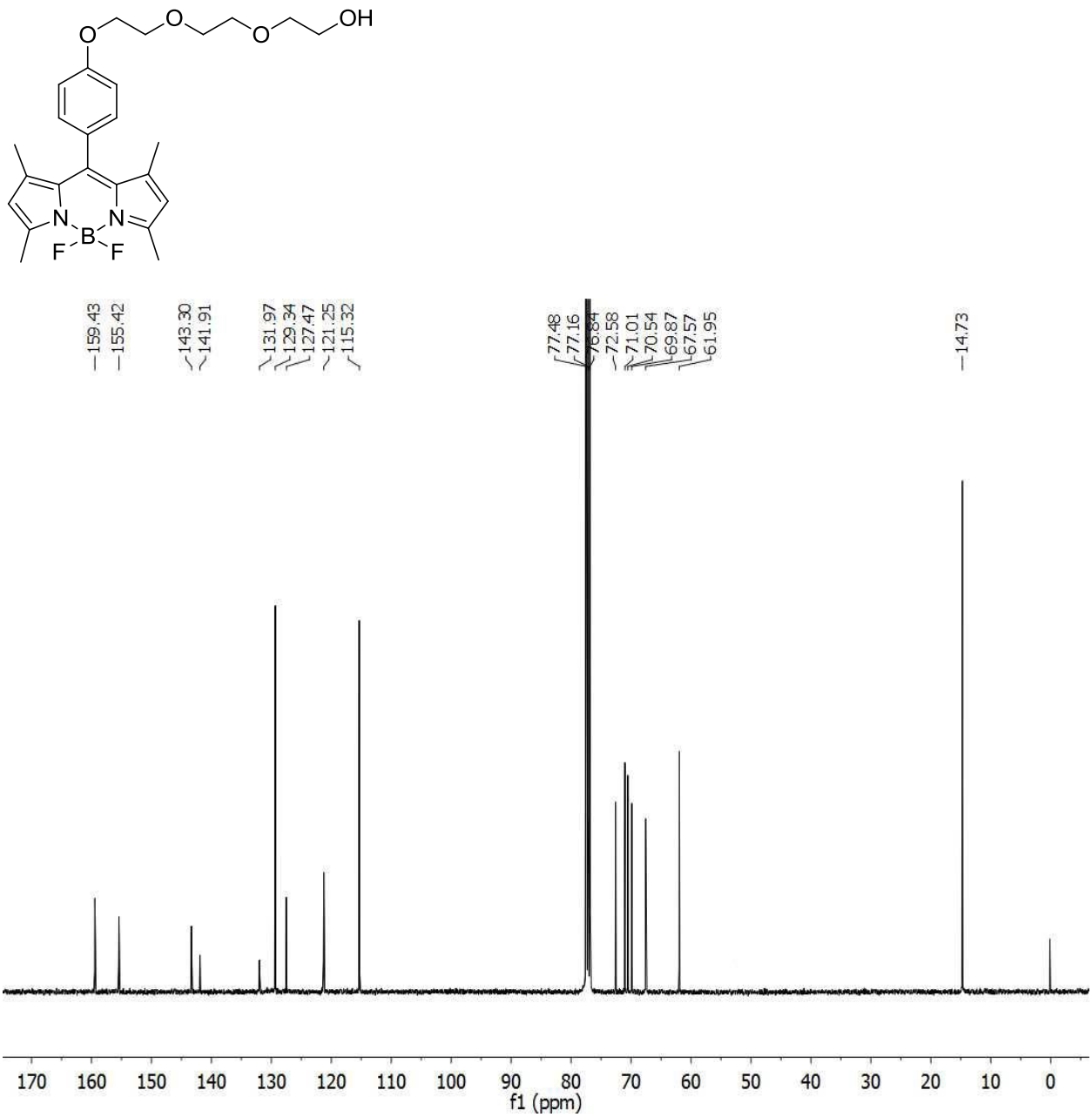

$^{1}$H NMR spectrum of compound **3**

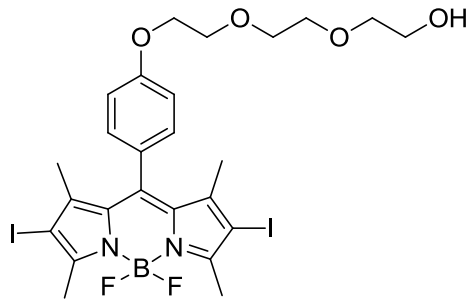


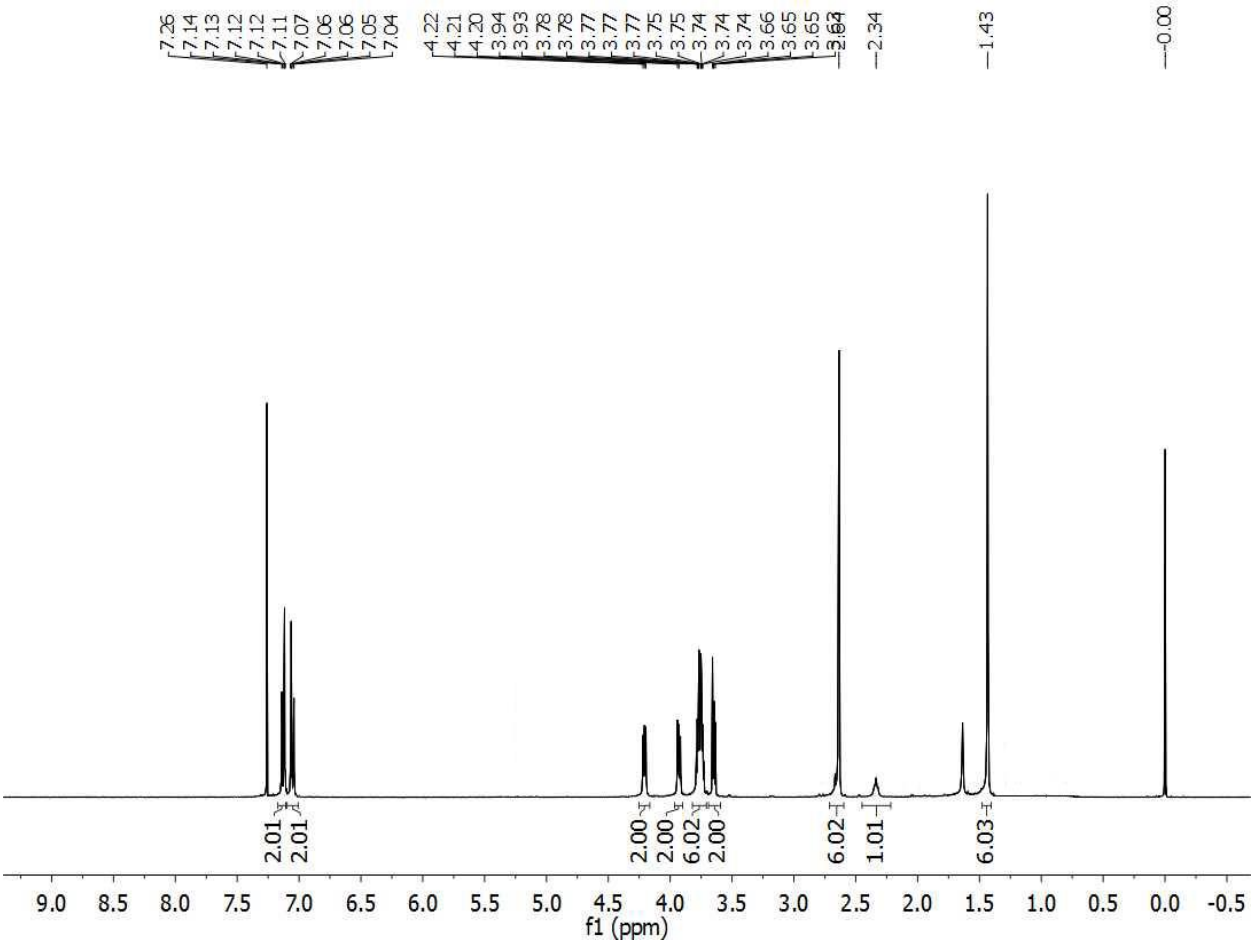

$^{13}$C NMR spectrum of compound **3**

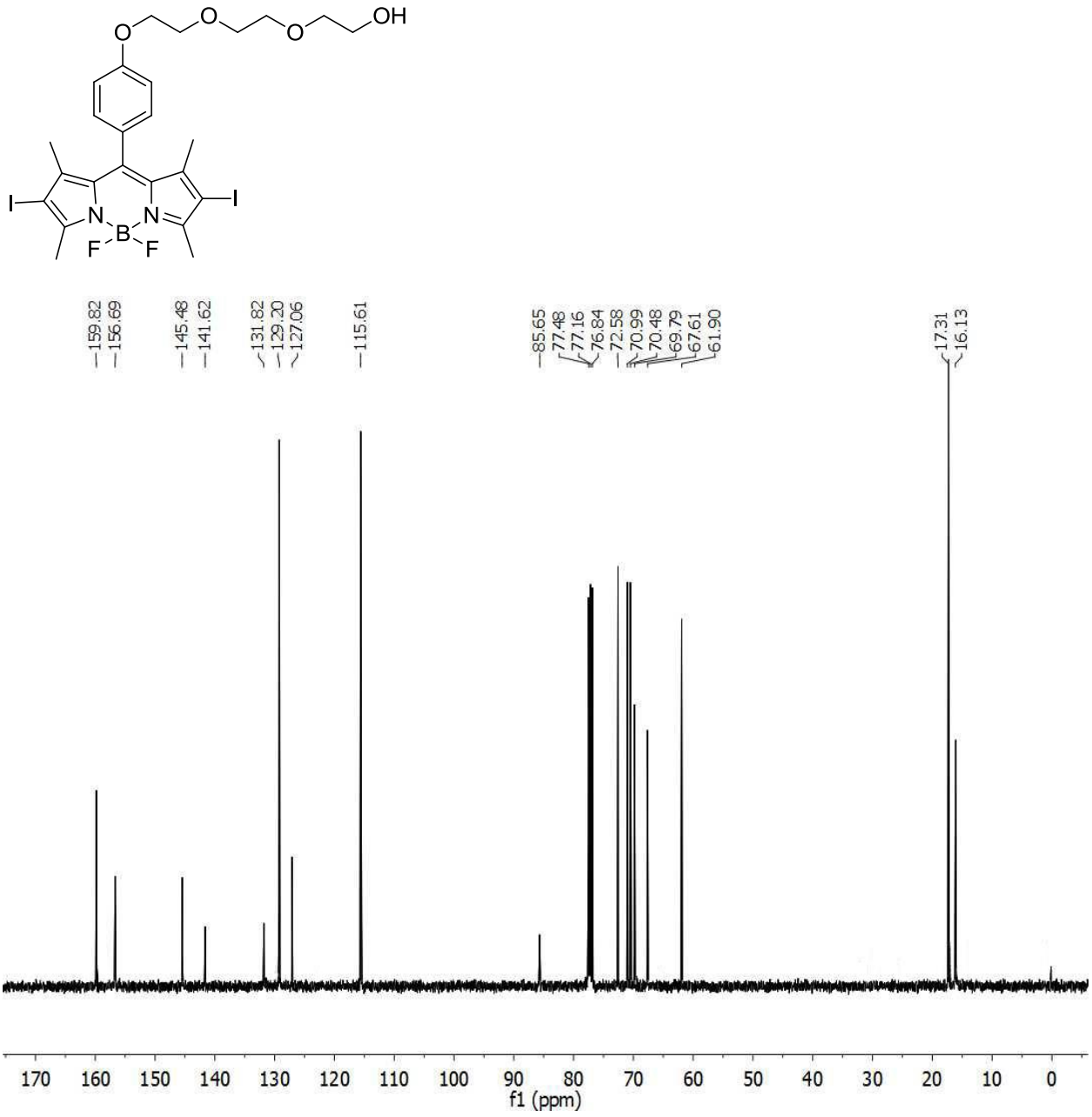

# LIST OF REFERENCES


1. Göppert-Mayer, M., Über Elementarakte mit zwei Quantensprüngen. *Ann Phys-Berlin* **1931,** *401* (3), 273-294.

2. Kaiser, W.; Garrett, C. G. B., Two-Photon Excitation in $CaF_2 : Eu^{2+}$. *Phys Rev Lett* **1961,** *7* (6), 229-231.

3. Ustione, A.; Piston, D. W., A simple introduction to multiphoton microscopy. *Journal of Microscopy* **2011,** *243* (3), 221-226.

4. Dolmans, D. E. J. G. J.; Fukumura, D.; Jain, R. K., Photodynamic therapy for cancer. *Nature Reviews Cancer* **2003,** *3* (5), 380-387.

5. Detty, M. R.; Merkel, P. B., Chalcogenapyrylium Dyes as Potential Photochemotherapeutic Agents - Solution Studies of Heavy-Atom Effects on Triplet Yields, Quantum Efficiencies of Singlet Oxygen Generation, Rates of Reaction with Singlet Oxygen, and Emission Quantum Yields. *J Am Chem Soc* **1990,** *112* (10), 3845-3855.

6. Dougherty, T. J.; Gomer, C. J.; Henderson, B. W.; Jori, G.; Kessel, D.; Korbelik, M.; Moan, J.; Peng, Q., Photodynamic therapy. *J Natl Cancer I* **1998,** *90* (12), 889-905.

7. Oleinick, N. L.; Morris, R. L.; Belichenko, T., The role of apoptosis in response to photodynamic therapy: what, where, why, and how. *Photoch Photobio Sci* **2002,** *1* (1), 1-21.

8. Weissleder, R., A clearer vision for in vivo imaging. *Nat Biotechnol* **2001,** *19* (4), 316-317.

9. Kiyose, K.; Kojima, H.; Nagano, T., Functional near-infrared fluorescent probes. *Chem-Asian J* **2008,** *3* (3), 506-515.

10. Peng, X. J.; Yang, Z. G.; Wang, J. Y.; Fan, J. L.; He, Y. X.; Song, F. L.; Wang, B. S.; Sun, S. G.; Qu, J. L.; Qi, J.; Yang, M., Fluorescence Ratiometry and Fluorescence Lifetime Imaging: Using a Single Molecular Sensor for Dual Mode Imaging of Cellular Viscosity. *J Am Chem Soc* **2011,** *133* (17), 6626-6635.

11. Yu, F. B. A.; Li, P.; Li, G. Y.; Zhao, G. J.; Chu, T. S.; Han, K. L., A Near-IR Reversible Fluorescent Probe Modulated by Selenium for Monitoring Peroxynitrite and Imaging in Living Cells. *J Am Chem Soc* **2011,** *133* (29), 11030-11033.

12. Myochin, T.; Kiyose, K.; Hanaoka, K.; Kojima, H.; Terai, T.; Nagano, T., Rational Design of Ratiometric Near-Infrared Fluorescent pH Probes with Various pK(a) Values, Based on Aminocyanine. *J Am Chem Soc* **2011,** *133* (10), 3401-3409.

13. Benson, R. C.; Kues, H. A., Absorption and Fluorescence Properties of Cyanine Dyes. *J Chem Eng Data* **1977,** *22* (4), 379-383.

14. Fu, M. Y.; Xiao, Y.; Qian, X. H.; Zhao, D. F.; Xu, Y. F., A design concept of long-wavelength fluorescent analogs of rhodamine dyes: replacement of oxygen with silicon atom. *Chem Commun* **2008,** (15), 1780-1782.

15. Koide, Y.; Urano, Y.; Hanaoka, K.; Terai, T.; Nagano, T., Evolution of Group 14 Rhodamines as Platforms for Near-Infrared Fluorescence Probes Utilizing Photoinduced Electron Transfer. *Acs Chem Biol* **2011,** *6* (6), 600-608.

16. Zhang, X. F.; Yu, H. B.; Xiao, Y., Replacing Phenyl Ring with Thiophene: An Approach to Longer Wavelength Aza-dipyrromethene Boron Difluoride (Aza-BODIPY) Dyes. *J Org Chem* **2012,** *77* (1), 669-673.

17. Bellier, Q.; Pegaz, S.; Aronica, C.; Le Guennic, B.; Andraud, C.; Maury, O., Near-Infrared Nitrofluorene Substitued Aza-Boron-dipyrromethenes Dyes. *Org Lett* **2011,** *13* (1), 22-25.

18. Loudet, A.; Bandichhor, R.; Wu, L. X.; Burgess, K., Functionalized BF(2) chelated azadipyrromethene dyes. *Tetrahedron* **2008,** *64* (17), 3642-3654.

19. Loudet, A.; Bandichhor, R.; Burgess, K.; Palma, A.; McDonnell, S. O.; Hall, M. J.; O'Shea, D. F., B,O-Chelated Azadipyrromethenes as Near-IR Probes. *Org Lett* **2008,** *10* (21), 4771-4774.

20. Yuan, L.; Lin, W. Y.; Yang, Y. T.; Chen, H., A Unique Class of Near-Infrared Functional Fluorescent Dyes with Carboxylic-Acid-Modulated Fluorescence ON/OFF Switching: Rational Design, Synthesis, Optical Properties, Theoretical Calculations, and Applications for Fluorescence Imaging in Living Animals. *J Am Chem Soc* **2012,** *134* (2), 1200-1211.

21. Buyukcakir, O.; Bozdemir, O. A.; Kolemen, S.; Erbas, S.; Akkaya, E. U., Tetrastyryl-Bodipy Dyes: Convenient Synthesis and Characterization of Elusive Near IR Fluorophores. *Org Lett* **2009,** *11* (20), 4644-4647.

22. Bura, T.; Retailleau, P.; Ulrich, G.; Ziessel, R., Highly Substituted Bodipy Dyes with Spectroscopic Features Sensitive to the Environment. *J Org Chem* **2011,** *76* (4), 1109-1117.

23. Ahn, H. Y.; Yao, S.; Wang, X.; Belfield, K. D., Near-Infrared-Emitting Squaraine Dyes with High 2PA Cross-Sections for Multiphoton Fluorescence Imaging. *Acs Appl Mater Inter* **2012,** *4* (6), 2847-2854.

24. Yu, H. B.; Xiao, Y.; Jin, L. J., A Lysosome-Targetable and Two-Photon Fluorescent Probe for Monitoring Endogenous and Exogenous Nitric Oxide in Living Cells. *J Am Chem Soc* **2012,** *134* (42), 17486-17489.

25. Dodani, S. C.; Leary, S. C.; Cobine, P. A.; Winge, D. R.; Chang, C. J., A Targetable Fluorescent Sensor Reveals That Copper-Deficient SCO1 and SCO2 Patient Cells Prioritize Mitochondrial Copper Homeostasis. *J Am Chem Soc* **2011,** *133* (22), 8606-8616.

26. Masanta, G.; Lim, C. S.; Kim, H. J.; Han, J. H.; Kim, H. M.; Cho, B. R., A Mitochondrial-Targeted Two-Photon Probe for Zinc Ion. *J Am Chem Soc* **2011,** *133* (15), 5698-5700.

27. Goeb, S.; Ziessel, R., Convenient synthesis of green diisoindolodithienylpyrromethene-dialkynyl borane dyes. *Org Lett* **2007,** *9* (5), 737-740.

28. Shen, Z.; Rohr, H.; Rurack, K.; Uno, H.; Spieles, M.; Schulz, B.; Reck, G.; Ono, N., Boron-diindomethene (BDI) dyes and their tetrahydrobicyclo precursors - en route to a new class of highly emissive fluorophores for the red spectral range. *Chem-Eur J* **2004,** *10* (19), 4853-4871.

29. Rurack, K.; Kollmannsberger, M.; Daub, J., Molecular switching in the near infrared (NIR) with a functionalized boron - Dipyrromethene dye. *Angew Chem Int Edit* **2001,** *40* (2), 385-387.

30. Burghart, A.; Kim, H. J.; Welch, M. B.; Thoresen, L. H.; Reibenspies, J.; Burgess, K.; Bergstrom, F.; Johansson, L. B. A., 3,5-diaryl-4,4-difluoro-4-bora-3a,4a-diaza-s-indacene (BODIPY) dyes: Synthesis, spectroscopic, electrochemical, and structural properties. *J Org Chem* **1999,** *64* (21), 7813-7819.

31. Gorman, A.; Killoran, J.; O'Shea, C.; Kenna, T.; Gallagher, W. M.; O'Shea, D. F., In vitro demonstration of the heavy-atom effect for photodynamic therapy. *J Am Chem Soc* **2004,** *126* (34), 10619-10631.

32. Yu, Y. H.; Descalzo, A. B.; Shen, Z.; Rohr, H.; Liu, Q.; Wang, Y. W.; Spieles, M.; Li, Y. Z.; Rurack, K.; You, X. Z., Mono- and di(dimethylamino) styryl-substituted borondipyrromethene and borondiindomethene dyes with intense near-infrared fluorescence. *Chem-Asian J* **2006,** *1* (1-2), 176-187.

33. Zhao, W. L.; Carreira, E. M., Conformationally restricted aza-bodipy: A highly fluorescent, stable, near-infrared-absorbing dye. *Angew Chem Int Edit* **2005,** *44* (11), 1677-1679.

34. Umezawa, K.; Matsui, A.; Nakamura, Y.; Citterio, D.; Suzuki, K., Bright, Color-Tunable Fluorescent Dyes in the Vis/NIR Region: Establishment of New "Tailor-Made" Multicolor Fluorophores Based on Borondipyrromethene. *Chem-Eur J* **2009,** *15* (5), 1096-1106.

35. Baruah, M.; Qin, W. W.; Flors, C.; Hofkens, J.; Vallee, R. A. L.; Beljonne, D.; Van der Auweraer, M.; De Borggraeve, W. M.; Boens, N., Solvent and pH dependent fluorescent properties of a dimethylaminostyryl borondipyrromethene dye in solution. *J Phys Chem A* **2006,** *110* (18), 5998-6009.

36. Zhang, D. K.; Wang, Y. C.; Xiao, Y.; Qian, S. X.; Qian, X. H., Long-wavelength boradiazaindacene derivatives with two-photon absorption activity and strong emission: versatile candidates for biological imaging applications. *Tetrahedron* **2009,** *65* (39), 8099-8103.

37. Zhang, D. K.; Martin, V.; Garcia-Moreno, I.; Costela, A.; Perez-Ojeda, M. E.; Xiao, Y., Development of excellent long-wavelength BODIPY laser dyes with a strategy that combines

extending pi-conjugation and tuning ICT effect. *Phys Chem Chem Phys* **2011,** *13* (28), 13026-13033.

38. Deniz, E.; Isbasar, G. C.; Bozdemir, O. A.; Yildirim, L. T.; Siemiarczuk, A.; Akkaya, E. U., Bidirectional switching of near IR emitting boradiazaindacene fluorophores. *Org Lett* **2008,** *10* (16), 3401-3403.

39. Loudet, A.; Burgess, K., BODIPY dyes and their derivatives: Syntheses and spectroscopic properties. *Chem Rev* **2007,** *107* (11), 4891-4932.

40. Helmchen, F.; Denk, W., Deep tissue two-photon microscopy. *Nat Methods* **2005,** *2* (12), 932-940.

41. Zipfel, W. R.; Williams, R. M.; Webb, W. W., Nonlinear magic: multiphoton microscopy in the biosciences. *Nat Biotechnol* **2003,** *21* (11), 1368-1376.

42. Kim, H. M.; Cho, B. R., Two-Photon Probes for Intracellular Free Metal Ions, Acidic Vesicles, And Lipid Rafts in Live Tissues. *Accounts Chem Res* **2009,** *42* (7), 863-872.

43. Kim, H. M.; Cho, B. R., Two-Photon Fluorescent Probes for Metal Ions. *Chem-Asian J* **2011,** *6* (1), 58-69.

44. Rihn, S.; Retailleau, P.; Bugsaliewicz, N.; De Nicola, A.; Ziessel, R., Versatile synthetic methods for the engineering of thiophene-substituted Bodipy dyes. *Tetrahedron Lett* **2009,** *50* (50), 7008-7013.

45. Han, F.; Chi, L. N.; Liang, X. F.; Ji, S. M.; Liu, S. S.; Zhou, F. K.; Wu, Y. B.; Han, K. L.; Zhao, J. Z.; James, T. D., 3,6-Disubstituted Carbazole-Based Bisboronic Acids with Unusual Fluorescence Transduction as Enantioselective Fluorescent Chemosensors for Tartaric Acid. *J Org Chem* **2009,** *74* (3), 1333-1336.

46. Lakowicz, J. R., *Principles of fluorescence spectroscopy*. 2nd ed.; Kluwer Academic/Plenum: New York, 1999; p xxiii, 698 p.

47. Valeur, B., *Molecular fluorescence : principles and applications*. Wiley-VCH: Weinheim ; New York, 2002; p xiv, 387 p.

48. Parson, W. W., *Modern optical spectroscopy : with examples from biophysics and biochemistry*. Springer: Berlin ; New York, 2007; p x, 512 p.

49. Heilemann, M.; Margeat, E.; Kasper, R.; Sauer, M.; Tinnefeld, P., Carbocyanine dyes as efficient reversible single-molecule optical switch. *J Am Chem Soc* **2005,** *127* (11), 3801-3806.

50. Cordes, T.; Vogelsang, J.; Anaya, M.; Spagnuolo, C.; Gietl, A.; Summerer, W.; Herrmann, A.; Mullen, K.; Tinnefeld, P., Single-Molecule Redox Blinking of Perylene Diimide Derivatives in Water. *J Am Chem Soc* **2010,** *132* (7), 2404-2409.

51. Haase, M.; Hubner, C. G.; Nolde, F.; Mullen, K.; Basche, T., Photoblinking and photobleaching of rylene diimide dyes. *Phys Chem Chem Phys* **2011,** *13* (5), 1776-1785.

52. Chalmers, S.; Caldwell, S. T.; Quin, C.; Prime, T. A.; James, A. M.; Cairns, A. G.; Murphy, M. P.; McCarron, J. G.; Hartley, R. C., Selective Uncoupling of Individual Mitochondria within a Cell Using a Mitochondria-Targeted Photoactivated Protonophore. *J Am Chem Soc* **2012,** *134* (2), 758-761.

53. Dickinson, B. C.; Chang, C. J., A targetable fluorescent probe for imaging hydrogen peroxide in the mitochondria of living cells. *J Am Chem Soc* **2008,** *130* (30), 9638-+.

54. Horobin, R. W.; Stockert, J. C.; Rashid-Doubell, F., Fluorescent cationic probes for nuclei of living cells: why are they selective? A quantitative structure-activity relations analysis. *Histochem Cell Biol* **2006,** *126* (2), 165-175.

55. Poole, B.; Ohkuma, S., Effect of Weak Bases on the Intralysosomal Ph in Mouse Peritoneal-Macrophages. *J Cell Biol* **1981,** *90* (3), 665-669.

56. Cousin, M. A.; Nicholls, D. G., Synaptic vesicle recycling in cultured cerebellar granule cells: Role of vesicular acidification and refilling. *J Neurochem* **1997,** *69* (5), 1927-1935.

57. Li, Z.; Wu, S. Q.; Han, J. H.; Han, S. F., Imaging of intracellular acidic compartments with a sensitive rhodamine based fluorogenic pH sensor. *Analyst* **2011,** *136* (18), 3698-3706.

58. Zhou, X. F.; Su, F. Y.; Lu, H. G.; Senechal-Willis, P.; Tian, Y. Q.; Johnson, R. H.; Meldrum, D. R., An FRET-based ratiometric chemosensor for in vitro cellular fluorescence analyses of pH. *Biomaterials* **2012,** *33* (1), 171-180.

59. Kim, H. M.; An, M. J.; Hong, J. H.; Jeong, B. H.; Kwon, O.; Hyon, J. Y.; Hong, S. C.; Lee, K. J.; Cho, B. R., Two-photon fluorescent probes for acidic vesicles in live cells and tissue. *Angew Chem Int Edit* **2008,** *47* (12), 2231-2234.

60. Belfield, K. D.; Bondar, M. V.; Morales, A. R.; Yue, X. L.; Luchita, G.; Przhonska, O. V.; Kachkovsky, O. D., Two-Photon Absorption and Time-Resolved Stimulated Emission Depletion Spectroscopy of a New Fluorenyl Derivative. *Chemphyschem : a European journal of chemical physics and physical chemistry* **2012,** *13* (15), 3481-3491.

61. Jiang, P. J.; Guo, Z. J., Fluorescent detection of zinc in biological systems: recent development on the design of chemosensors and biosensors. *Coordin Chem Rev* **2004,** *248* (1-2), 205-229.

62. Hilderbrand, S. A.; Weissleder, R., Near-infrared fluorescence: application to in vivo molecular imaging. *Curr Opin Chem Biol* **2010,** *14* (1), 71-79.

63. Denk, W.; Strickler, J. H.; Webb, W. W., 2-Photon Laser Scanning Fluorescence Microscopy. *Science* **1990,** *248* (4951), 73-76.

64. So, P. T. C.; Dong, C. Y.; Masters, B. R.; Berland, K. M., Two-photon excitation fluorescence microscopy. *Annu Rev Biomed Eng* **2000,** *2*, 399-429.

65. Andrade, C. D.; Yanez, C. O.; Rodriguez, L.; Belfield, K. D., A Series of Fluorene-Based Two-Photon Absorbing Molecules: Synthesis, Linear and Nonlinear Characterization, and Bioimaging. *J Org Chem* **2010,** *75* (12), 3975-3982.

66. Morales, A. R.; Schafer-Hales, K. J.; Marcus, A. I.; Belfield, K. D., Amine-Reactive Fluorene Probes: Synthesis, Optical Characterization, Bioconjugation, and Two-Photon Fluorescence Imaging. *Bioconjugate Chem* **2008,** *19* (12), 2559-2567.

67. Ferrari, M., Cancer nanotechnology: Opportunities and challenges. *Nature Reviews Cancer* **2005,** *5* (3), 161-171.

68. Li, Z. M.; Huang, P.; Zhang, X. J.; Lin, J.; Yang, S.; Liu, B.; Gao, F.; Xi, P.; Ren, Q. S.; Cui, D. X., RGD-Conjugated Dendrimer-Modified Gold Nanorods for in Vivo Tumor Targeting and Photothermal Therapy. *Mol Pharmaceut* **2010,** *7* (1), 94-104.

69. Ruoslahti, E.; Bhatia, S. N.; Sailor, M. J., Targeting of drugs and nanoparticles to tumors. *J Cell Biol* **2010,** *188* (6), 759-768.

70. Wu, W. B.; Liu, C.; Wang, M. L.; Huang, W.; Zhou, S. R.; Jiang, W.; Sun, Y. M.; Cui, Y. P.; Xu, C. X., Uniform silica nanoparticles encapsulating two-photon absorbing fluorescent dye. *J Solid State Chem* **2009,** *182* (4), 862-868.

71. Wang, X. H.; Morales, A. R.; Urakami, T.; Zhang, L. F.; Bondar, M. V.; Komatsu, M.; Belfield, K. D., Folate Receptor-Targeted Aggregation-Enhanced Near-IR Emitting Silica

Nanoprobe for One-Photon in Vivo and Two-Photon ex Vivo Fluorescence Bioimaging. *Bioconjugate Chem* **2011,** *22* (7), 1438-1450.

72. Qian, J.; Wang, D.; Cai, F. H.; Zhan, Q. Q.; Wang, Y. L.; He, S. L., Photosensitizer encapsulated organically modified silica nanoparticles for direct two-photon photodynamic therapy and In Vivo functional imaging. *Biomaterials* **2012,** *33* (19), 4851-4860.

73. Lebret, V.; Raehm, L.; Durand, J. O.; Smaihi, M.; Gerardin, C.; Nerambourg, N.; Werts, M. H. V.; Blanchard-Desce, M., Synthesis and characterization of fluorescently doped mesoporous nanoparticles for two-photon excitation. *Chem Mater* **2008,** *20* (6), 2174-2183.

74. Kim, S.; Ohulchanskyy, T. Y.; Pudavar, H. E.; Pandey, R. K.; Prasad, P. N., Organically modified silica nanoparticles co-encapsulating photosensitizing drug and aggregation-enhanced two-photon absorbing fluorescent dye aggregates for two-photon photodynamic therapy. *J Am Chem Soc* **2007,** *129* (9), 2669-2675.

75. Corredor, C. C.; Huang, Z. L.; Belfield, K. D.; Morales, A. R.; Bondar, M. V., Photochromic polymer composites for two-photon 3D optical data storage. *Chem Mater* **2007,** *19* (21), 5165-5173.

76. Santos, P. F.; Reis, L. V.; Almeida, P.; Serrano, J. P.; Oliveira, A. S.; Ferreira, L. F. V., Efficiency of singlet oxygen generation of aminosquarylium cyanines. *J Photoch Photobio A* **2004,** *163* (1-2), 267-269.

77. Ramaiah, D.; Eckert, I.; Arun, K. T.; Weidenfeller, L.; Epe, B., Squaraine dyes for photodynamic therapy: Mechanism of cytotoxicity and DNA damage induced by halogenated squaraine dyes plus light (> 600 nm). *Photochem Photobiol* **2004,** *79* (1), 99-104.

78. Morales, A. R.; Yanez, C. O.; Schafer-Hales, K. J.; Marcus, A. I.; Belfield, K. D., Biomolecule Labeling and Imaging with a New Fluorenyl Two-Photon Fluorescent Probe. *Bioconjugate Chem* **2009,** *20* (10), 1992-2000.

79. Ulrich, G.; Ziessel, R.; Harriman, A., The chemistry of fluorescent bodipy dyes: Versatility unsurpassed. *Angew Chem Int Edit* **2008,** *47* (7), 1184-1201.

80. Lim, S. H.; Thivierge, C.; Nowak-Sliwinska, P.; Han, J. Y.; van den Bergh, H.; Wagnieres, G.; Burgess, K.; Lee, H. B., In Vitro and In Vivo Photocytotoxicity of Boron Dipyrromethene Derivatives for Photodynamic Therapy. *J Med Chem* **2010,** *53* (7), 2865-2874.

81. Karolin, J.; Johansson, L. B. A.; Strandberg, L.; Ny, T., Fluorescence and Absorption Spectroscopic Properties of Dipyrrometheneboron Difluoride (Bodipy) Derivatives in Liquids, Lipid-Membranes, and Proteins. *J Am Chem Soc* **1994,** *116* (17), 7801-7806.

82. Renfrew, C. A.; Hubbard, A. L., Degradation of Epidermal Growth-Factor Receptor in Rat-Liver - Membrane Topology through the Lysosomal Pathway. *J Biol Chem* **1991,** *266* (31), 21265-21273.

83. Marks, M. S.; Roche, P. A.; Vandonselaar, E.; Woodruff, L.; Peters, P. J.; Bonifacino, J. S., A Lysosomal Targeting Signal in the Cytoplasmic Tail of the Beta-Chain Directs Hla-Dm to Mhc Class-Ii Compartments. *J Cell Biol* **1995,** *131* (2), 351-369.

84. Saftig, P.; Klumperman, J., Lysosome biogenesis and lysosomal membrane proteins: trafficking meets function. *Nat Rev Mol Cell Bio* **2009,** *10* (9), 623-635.

85. Soreghan, M.; Thomas, S. N.; Yang, A. J., Aberrant sphingomyelin/ceramide metabolic-induced neuronal endosomal/lysosomal dysfunction: potential pathological consequences in age-related neurodegeneration. *Adv Drug Deliver Rev* **2003,** *55* (11), 1515-1524.

86. Mohamed, M. M.; Sloane, B. F., Cysteine cathepsins: multifunctional enzymes in cancer. *Nature Reviews Cancer* **2006,** *6* (10), 764-775.

87. Dobrucki, L. W.; de Muinck, E. D.; Lindner, J. R.; Sinusas, A. J., Approaches to Multimodality Imaging of Angiogenesis. *J Nucl Med* **2010,** *51*, 66s-79s.

88. Morlieras, J.; Dufort, S.; Sancey, L.; Truillet, C.; Mignot, A.; Rossetti, F.; Dentamaro, M.; Laurent, S.; Vander Elst, L.; Muller, R. N.; Antoine, R.; Dugourd, P.; Roux, S.; Perriat, P.; Lux, F.; Coll, J. L.; Tillement, O., Functionalization of Small Rigid Platforms with Cyclic RGD Peptides for Targeting Tumors Overexpressing alpha(v)beta(3)-Integrins. *Bioconjugate Chem* **2013,** *24* (9), 1584-1597.

89. Ishikawa, A.; Zhou, Y. M.; Kambe, N.; Nakayama, Y., Enhancement of star vector-based gene delivery to endothelial cells by addition of RGD-peptide. *Bioconjugate Chem* **2008,** *19* (2), 558-561.

90. Cai, W. B.; Wu, Y.; Chen, K.; Cao, Q. Z.; Tice, D. A.; Chen, X. Y., In vitro and in vivo characterization of Cu-64-labeled Abegrin (TM) a humanized monoclonal antibody against integrin alpha(v)beta(3). *Cancer Res* **2006,** *66* (19), 9673-9681.

91. Wong, N. C.; Mueller, B. M.; Barbas, C. F.; Ruminski, P.; Quaranta, V.; Lin, E. C. K.; Smith, J. W., alpha(v) integrins mediate adhesion and migration of breast carcinoma cell lines. *Clin Exp Metastas* **1998,** *16* (1), 50-61.

92. Hood, J. D.; Cheresh, D. A., Role of integrins in cell invasion and migration. *Nature Reviews Cancer* **2002,** *2* (2), 91-+.

93. Varner, J. A.; Cheresh, D. A., Integrins and cancer. *Curr Opin Cell Biol* **1996,** *8* (5), 724-730.

94. Felding-Habermann, B.; O'Toole, T. E.; Smith, J. W.; Fransvea, E.; Ruggeri, Z. M.; Ginsberg, M. H.; Hughes, P. E.; Pampori, N.; Shattil, S. J.; Saven, A.; Mueller, B. M., Integrin activation controls metastasis in human breast cancer. *P Natl Acad Sci USA* **2001,** *98* (4), 1853-1858.

95. Morales, A. R.; Belfield, K. D.; Hales, J. M.; Van Stryland, E. W.; Hagan, D. J., Synthesis of two-photon absorbing unsymmetrical fluorenyl-based chromophores. *Chem Mater* **2006,** *18* (20), 4972-4980.

96. Jager, W. F.; Volkers, A. A.; Neckers, D. C., Solvatochromic Fluorescent-Probes for Monitoring the Photopolymerization of Dimethacrylates. *Macromolecules* **1995,** *28* (24), 8153-8158.

97. Yao, S.; Ahn, H. Y.; Wang, X. H.; Fu, J.; Van Stryland, E. W.; Hagan, D. J.; Belfield, K. D., Donor-Acceptor-Donor Fluorene Derivatives for Two-Photon Fluorescence Lysosomal Imaging. *J Org Chem* **2010,** *75* (12), 3965-3974.

98. Lakowicz, J. R., *Principles of fluorescence spectroscopy*. 3rd ed.; Springer: New York, 2006; p xxvi, 954 p.

99. Wang, X. H.; Nguyen, D. M.; Yanez, C. O.; Rodriguez, L.; Ahn, H. Y.; Bonder, M. V.; Belfield, K. D., High-Fidelity Hydrophilic Probe for Two-Photon Fluorescence Lysosomal Imaging. *J Am Chem Soc* **2010,** *132* (35), 12237-12239.

100. Corredor, C. C.; Belfield, K. D.; Bondar, M. V.; Przhonska, O. V.; Yao, S., One- and two-photon photochemical stability of linear and branched fluorene derivatives. *J Photoch Photobio A* **2006,** *184* (1-2), 105-112.

101. Beer, A. J.; Kessler, H.; Wester, H. J.; Schwaiger, M., PET Imaging of Integrin alpha V beta 3 Expression. *Theranostics* **2011,** *1*, 48-57.

102. Zhang, X. F.; Xiao, Y.; Qi, J.; Qu, J. L.; Kim, B.; Yue, X. L.; Belfield, K. D., Long-Wavelength, Photostable, Two-Photon Excitable BODIPY Fluorophores Readily Modifiable for Molecular Probes. *J Org Chem* **2013,** *78* (18), 9153-9160.

103. Sheikbahae, M.; Said, A. A.; Wei, T. H.; Hagan, D. J.; Vanstryland, E. W., Sensitive Measurement of Optical Nonlinearities Using a Single Beam. *Ieee J Quantum Elect* **1990,** *26* (4), 760-769.

104. Biswas, S.; Ahn, H. Y.; Bondar, M. V.; Belfield, K. D., Two-Photon Absorption Enhancement of Polymer-Templated Porphyrin-Based J-Aggregates. *Langmuir* **2012,** *28* (2), 1515-1522.

105. Kumar, R.; Roy, I.; Hulchanskyy, T. Y.; Goswami, L. N.; Bonoiu, A. C.; Bergey, E. J.; Tramposch, K. M.; Maitra, A.; Prasad, P. N., Covalently dye-linked, surface-controlled, and bioconjugated organically modified silica nanoparticles as targeted probes for optical imaging. *Acs Nano* **2008,** *2* (3), 449-456.

106. Avirah, R. R.; Jayaram, D. T.; Adarsh, N.; Ramaiah, D., Squaraine dyes in PDT: from basic design to in vivo demonstration. *Org Biomol Chem* **2012,** *10* (5), 911-920.

107. Treibs, A.; Kreuzer, F. H., Di- and Tri-Pyrrylmethene Complexes with Di-Fluoro Boron. *Liebigs Ann Chem* **1968,** *718* (Dec), 208-+.

108. Ziessel, R.; Ulrich, G.; Harriman, A., The chemistry of Bodipy: a new El Dorado for fluorescence tools. *New J Chem* **2007,** *31* (4), 496-501.

109. Zheng, Q. D.; Xu, G. X.; Prasad, P. N., Conformationally restricted dipyrromethene boron difluoride (BODIPY) dyes: Highly fluorescent, multicolored probes for cellular imaging. *Chem-Eur J* **2008,** *14* (19), 5812-5819.

110. Lee, J. S.; Kang, N. Y.; Kim, Y. K.; Samanta, A.; Feng, S. H.; Kim, H. K.; Vendrell, M.; Park, J. H.; Chang, Y. T., Synthesis of a BODIPY Library and Its Application to the Development of Live Cell Glucagon Imaging Probe. *J Am Chem Soc* **2009,** *131* (29), 10077-10082.

111. Peng, X. J.; Du, J. J.; Fan, J. L.; Wang, J. Y.; Wu, Y. K.; Zhao, J. Z.; Sun, S. G.; Xu, T., A selective fluorescent sensor for imaging Cd2+ in living cells. *J Am Chem Soc* **2007,** *129* (6), 1500-+.

112. Domaille, D. W.; Zeng, L.; Chang, C. J., Visualizing Ascorbate-Triggered Release of Labile Copper within Living Cells using a Ratiometric Fluorescent Sensor. *J Am Chem Soc* **2010,** *132* (4), 1194-+.

113. Erten-Ela, S.; Yilmaz, M. D.; Icli, B.; Dede, Y.; Icli, S.; Akkaya, E. U., A panchromatic boradiazaindacene (BODIPY) sensitizer for dye-sensitized solar cells. *Org Lett* **2008,** *10* (15), 3299-3302.

114. Kolemen, S.; Cakmak, Y.; Erten-Ela, S.; Altay, Y.; Brendel, J.; Thelakkat, M.; Akkaya, E. U., Solid-State Dye-Sensitized Solar Cells Using Red and Near-IR Absorbing Bodipy Sensitizers. *Org Lett* **2010,** *12* (17), 3812-3815.

115. Yogo, T.; Urano, Y.; Ishitsuka, Y.; Maniwa, F.; Nagano, T., Highly efficient and photostable photosensitizer based on BODIPY chromophore. *J Am Chem Soc* **2005,** *127* (35), 12162-12163.

116. Erbas, S.; Gorgulu, A.; Kocakusakogullari, M.; Akkaya, E. U., Non-covalent functionalized SWNTs as delivery agents for novel Bodipy-based potential PDT sensitizers. *Chem Commun* **2009,** (33), 4956-4958.

117. Atilgan, S.; Ekmekci, Z.; Dogan, A. L.; Guc, D.; Akkaya, E. U., Water soluble distyryl-boradiazaindacenes as efficient photosensitizers for photodynamic therapy. *Chem Commun* **2006,** (42), 4398-4400.

118. Liu, J. Y.; Yeung, H. S.; Xu, W.; Li, X. Y.; Ng, D. K. P., Highly Efficient Energy Transfer in Subphthalocyanine-BODIPY Conjugates. *Org Lett* **2008,** *10* (23), 5421-5424.

119. Tatsuta, M.; Iishi, H.; Yamamura, H.; Yamamoto, R.; Okuda, S., Comparison of Photodynamic Inactivation of Experimental Stomach Tumors Sensitized by Acridine-Orange or Hematoporphyrin Derivatives. *Oncology* **1988,** *45* (1), 35-40.

120. Kusuzaki, K.; Minami, G.; Takeshita, H.; Murata, H.; Hashiguchi, S.; Nozaki, T.; Ashihara, T.; Hirasawa, Y., Photodynamic inactivation with acridine orange on a multidrug-resistant mouse osteosarcoma cell line. *Jpn J Cancer Res* **2000,** *91* (4), 439-445.

121. Cevik, I. U.; Dalkara, T., Intravenously administered propidium iodide labels necrotic cells in the intact mouse brain after injury. *Cell Death Differ* **2003,** *10* (8), 928-929.

122. Billamboz, M.; Mangin, F.; Drillaud, N.; Chevrin-Villette, C.; Banaszak-Leonard, E.; Len, C., Micellar Catalysis Using a Photochromic Surfactant: Application to the Pd-Catalyzed Tsuji-Trost Reaction in Water. *J Org Chem* **2014,** *79* (2), 493-500.

123. Bautista-Sanchez, A.; Kasselouri, A.; Desroches, M. C.; Blais, J.; Maillard, P.; de Oliveira, D. M.; Tedesco, A. C.; Prognon, P.; Delaire, J., Photophysical properties of

glucoconjugated chlorins and porphyrins and their associations with cyclodextrins. *J Photoch Photobio B* **2005,** *81* (3), 154-162.

124. Pandey, R. K.; Sumlin, A. B.; Constantine, S.; Aoudia, M.; Potter, W. R.; Bellnier, D. A.; Henderson, B. W.; Rodgers, M. A.; Smith, K. M.; Dougherty, T. J., Alkyl ether analogs of chlorophyll-a derivatives .1. Synthesis, photophysical properties and photodynamic efficacy. *Photochem Photobiol* **1996,** *64* (1), 194-204.

125. Keszthelyi, T.; Weldon, D.; Andersen, T. N.; Poulsen, T. D.; Mikkelsen, K. V.; Ogilby, P. R., Radiative transitions of singlet oxygen: New tools, new techniques and new interpretations. *Photochem Photobiol* **1999,** *70* (4), 531-539.

126. Wilkinson, F.; Helman, W. P.; Ross, A. B., Quantum Yields for the Photosensitized Formation of the Lowest Electronically Excited Singlet-State of Molecular-Oxygen in Solution. *J Phys Chem Ref Data* **1993,** *22* (1), 113-262.